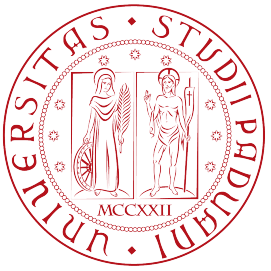

UNIVERSITÀ DEGLI STUDI DI PADOVA

DIPARTIMENTO DI INGEGNERIA CIVILE, EDILE E AMBIENTALE

CORSO DI DOTTORATO IN SCIENZE DELL'INGEGNERIA CIVILE E AMBIENTALE

XXXIV CICLO

Exploring pulsing river networks using empirical and theoretical tools

Thesis written with the financial contribution of
the European Research Council

Coordinator
Ch.mo Prof. Carmelo Maiorana

Supervisor
Ch.mo Prof. Gianluca Botter

Ph.D student
Nicola Durighetto

Academic year 2020-2021

Summary

River networks shape the Earth landscape and promote a multitude of biogeochemical processes, such as erosion and transport of sediments and nutrients. Furthermore, streams and rivers have always played a fundamental role for human activities, often being the primary source for freshwater, promoting the development of advanced societies, and providing food, energy and efficient pathways for transportation. Recently, the temporal dimension of river networks has been recognized as a core issue not only over geological timescales, but also during individual years or seasons, within which river segments may temporarily cease to flow. Empirical evidence has shown that the flowing portion of many river networks does vary in time, owing to seasonal and/or event-based expansion-retraction cycles that mimic the unsteady nature of the underlying climatic forcing. Such rivers, commonly referred to as temporary streams, are believed to represent more than half of the global river network, and are observed in most climatic regions worldwide, from arid, to humid areas. The goal of this thesis is to provide a comprehensive hydrological analysis of temporary streams, by combining empirical data from 18 study catchments spread all over the world with theoretical analyses and stochastic models. A Bayesian framework is developed for the statistical description of the dynamics of the active network, linking the behaviour of the stream network to the underlying local properties of the constituting nodes. The local persistency of the nodes is found to be a key statistical index to quantify the probability of activation of each node, and dictates the interaction between different nodes and defines the spatial pattern of active network at any given time. The activation of the nodes during network expansion is found to follow a fixed order of decreasing persistency, while the deactivation of nodes during network contraction occurs in reverse order. This general behaviour, called hierarchical, is defined in a mathematically rigorous way within the Bayesian framework, and used to derive analytical expressions for the main statistics of the active length as function of the mean network persistency. The latter is then linked to the mean effective precipitation, thus providing a direct connection between climate and network dynamics. The Stream Length Duration Curve links each possible length of the active network to the duration for which that length is exceeded, and allows a quantitative description of the dynamics of a temporary stream. Under the hierarchical hypothesis, this curve is proven to be solely determined by the spatial distribution of the local persistency, providing a crucial link between the spatial and temporal dimensions of the problem. Temporary streams can be also characterized via their length regimes, providing an objective classification system based on the dynamic behaviour of the networks. A stochastic model for streamflow generation

is also exploited in conjunction with the hierarchical activation scheme, to enable the spatio-temporal simulation of a temporary stream under a wide variety of climatic scenarios. This type of simulations require a small number of parameters and a limited computational effort, and allows a deeper understanding of the influence of climate on the origins and implications of channel network dynamics. A set of synthetic temporary streams are used as input for a dynamic metapopulation model simulating the occupancy of a target aquatic species within the network. This application reveals the fundamental role that network dynamics have in degrading the ability of a riverine ecosystem to support a metapopulation, particularly in drier climates, by significantly reducing the average occupancy and increasing the probability of extinction of the target species. Taking into account the dynamic nature of the active network represents a fundamental prerequisite for a correct assessment of many ecological and biochemical functions that are mediated by riverine systems. The work presented in this thesis offers a comprehensive analysis of dynamical river networks, providing a new theoretical framework and novel analytical tools and numerical models for the reconstruction and simulation of the dynamics of the active extent of a stream. Given the rising awareness of the impacts of human activities on the environment, and the sensitivity of temporary streams to a changing climate, the tools provided in this study will hopefully foster the development of better strategies for the management and protection of such systems.

Acknowledgements

My most sincere gratitude goes my PhD supervisor to Gianluca Botter. The passion you put in givin your lectures in my undergraduate days spared my love for hydrology. Then you provided me with the fascinating research topic of this thesis, and with all the support and advices that I needed. I hope that all my effort and the results we obtained demonstrate my admiration for your work and professionalism. I would also like to thank my colleague Francesca Zanetti, and all the students that helped me throughout the years with the field work, because part of this thesis would not have been possible without their contribution. A final thanks goes to my family and friends, who supported me throughout this journey.

Contents

List of Figures

List of Tables

1 Introduction

Water is essential to all forms of life for a number of reasons, including the fact that it acts as a vector for the transport of nutrients and other substances. The hydrosphere is a fundamental component of the Earth because it covers more than 70% of its surface and shapes its form. The hydrosphere is a dynamic system, in which water continuously move generating an endless water cycle that supply water to the environment. Starting from precipitation falling onto the soil, water drains through the hillslopes forming organized structures that are commonly identified as streams and rivers. These drainage networks collect water from the uplands and efficiently transport it downstream to the sea or the ocean. As such, river networks shape the Earth landscape and control fundamental ecological processes, by regulating a multitude of hydro-biogeochemical processes such as erosion and transport of sediments and nutrients (e.g. Battin et al. 2008; Rinaldo et al. 2018). Rivers provide a wide spectrum habitats, supporting diverse aquatic and riparian biota, thus promoting biodiversity, and act as a preferential pathway for the transport of aquatic species, as well as pollutants and waterborne diseases. Furthermore, streams and rivers have always played a fundamental role for human activities, because they represent the primary source for freshwater. Rivers promoted the development of advanced societies, providing food, energy and efficient pathways for transportation.

For decades, the spatial organization of streams has stimulated scientific debate around observed morphological and ecological patterns in river basins. At fine scales, the location of the channel heads has been the focus of pioneering work (Montgomery et al. 1988; Montgomery et al. 1989) that fuelled an array of methodologies for the analysis of Digital Terrain Maps; at larger spatial scales, theoretical investigations examined origins and implications of the branching shape of river networks and their fractal nature (Kirchner 1993; Rinaldo et al. 1993; Rodriguez-Iturbe et al. 1997; Banavar et al. 1999; Sassolas-Serrayet et al. 2018; Yi et al. 2018).

Recently, the temporal dimension of river networks has been recognized as a core issue not only over geological timescales typical of landscape evolution models, but also during individual years or seasons, within which river segments may temporarily cease to flow (e.g. Godsey et al. 2014; Acuña et al. 2014; Zimmer et al. 2020). This empirical evidence has shown that the flowing portion of many river networks does vary in time, owing to seasonal and/or event-based expansion-retraction cycles that mimic the unsteady nature of the underlying climatic forcing. Such rivers, commonly referred to as temporary streams, are believed to represent more than half of the global river network (Datry et al. 2014). Temporary streams are observed in most

climatic regions worldwide, including arid, semi-arid, Mediterranean, temperate and humid areas (Skoulikidis et al. 2017; Durighetto et al. 2020). The dynamic nature of channel networks has important implications beyond catchment hydrology, which include nutrient cycling, green-house gas emissions, stream metabolism, ecological dispersion and water management (Abbott et al. 2016; Berger et al. 2017; Dupas et al. 2019; Von Schiller et al. 2014; Boodoo et al. 2017; Datry et al. 2018; Datry et al. 2014; Vander Vorste et al. 2020a; Nikolaidis et al. 2013; Acuña et al. 2014; Reyjol et al. 2014). Therefore, the study of active stream dynamics is pivotal not only to characterize spatial patterns of hydrologic regimes but also to understand the influence of flow intermittency on e.g. ecological dispersion, in-stream processes, hyporheic exchange and nutrient spiraling (Cardenas 2007; Mari et al. 2014; Tonkin et al. 2017; Burrows et al. 2017; Stubbington et al. 2017; Datry et al. 2017).

The first hydrologic studies about temporary streams date back to half a century ago (Gregory et al. 1968; Morgan 1972; Blyth et al. 1973; Anderson et al. 1978; Day 1978; Roberts 1978; Gregory et al. 1979; Day 1980; Day 1983). Those pioneering works revealed the twofold challenge that underlies the study of temporary streams: while collecting empirical data implies a significant burden, extensive datasets are necessary to disentangle the intertwined spatial and temporal dimensions of the problem, which complicate the identification of the physical processes underpinning the activation/deactivation of different stream portions. Even tough field monitoring remains to date labor intensive, the last decade had seen a significant increase in the number of available datasets. Most of the empirical data about network dynamics is still collected by visual inspection during field surveys (Zimmer et al. 2017; Shaw 2016; Shaw et al. 2017; Jensen et al. 2017; Datry et al. 2016; Durighetto et al. 2020; Senatore et al. 2020; Godsey et al. 2014; Whiting et al. 2016; Lovill et al. 2018; Van Meerveld et al. 2019). However, new technologies have been introduced to reduce monitoring efforts, including electrical resistance sensors (Goulsbra et al. 2014; Peirce et al. 2015; Jaeger et al. 2012; Assendelft et al. 2019; Jensen et al. 2019; Kaplan et al. 2019; Paillex et al. 2020; Perez et al. 2020; Zanetti et al. 2021), aerial photographs (Wiginton et al. 2005; Phillips et al. 2011; González-Ferreras et al. 2017; Malard et al. 2006) and unmanned vehicles (Jensen et al. 2012; Neachell 2014; Debell et al. 2015; Woodget et al. 2015; Spence et al. 2016; Pai et al. 2017; Woodget et al. 2017; Briggs et al. 2019; Borg Galea et al. 2019; Casas-Mulet et al. 2020; Samboko et al. 2020; Kuhn et al. 2021). Nonetheless, a limited number of studies about river network dynamics have been conducted in continental Europe so far, and only few of them provided a full survey of the flowing stream network on a regular basis. In some cases the analysis was restricted to individual stretches (Doering et al. 2007; Medici et al. 2008) or to the channel heads only (Agren et al. 2015), not including the full geometrical complexity of the river network and the presence of disconnected reaches. Other studies, instead, monitored the hydrologic status of a pre-defined set of nodes that do not necessarily correspond to the entire network (Datry et al. 2016), leading to a possible underestimation of the drainage density. In other cases, sporadic surveys were performed (Van Meerveld et al. 2019), preventing a full characterization of the stream network variability over multiple time-scales. As a consequence, comprehensive and organic datasets for the

description of stream dynamics within different sites characterized by heterogeneous climates, physiographies and land covers, are very rare.

In order to explain the main drivers of network dynamics, Godsey et al. 2014 and Prancevic et al. 2019 proposed a conceptual model that links the surface flow at a point to the imbalance between the downvalley seepage rate (seen as the combination of surface and subsurface flows, and proportional to the cumulated area) and subsurface transmissivity (related to hydraulic conductivity, local slope and valley cross-sectional area). However, the application of this conceptual model for the prediction or the simulation of the spatial patterns of the flowing streams is problematic, as it would require the specification of spatial patterns subsurface transmissivity and valley cross-sectional area, which are very difficult to measure or predict.

Few other studies have directly linked network dynamics to climatic variables such as antecedent precipitation and evapotranspiration (Morgan 1972; Blyth et al. 1973; Goulsbra et al. 2014; Jaeger et al. 2019; Jensen et al. 2018; Ward et al. 2018; Jensen et al. 2019), but none of them allows the prediction of the temporal variability of stream network length based on precipitation data alone. Moreover, in all the existing studies the aggregation timescale of the precipitation input (or its range) was pre-defined. Consequently, the full spectrum of impacts of rainfall variability on stream length dynamics - and particularly the combined effects of short-term and long-term rainfall - has not been fully captured yet.

In spite of the enhanced availability of empirical data, to date there is a limited availability of analytical tools with general applicability that are suitable to objectively characterize the magnitude and the extent of river network variability through time. To date, the outcome of experimental surveys is usually represented by a set of active stream network maps characterized by different scales and resolutions (e.g. Shaw et al. 2017; Jensen et al. 2018), complemented by a variety of statistical analyses of relevant stream attributes (e.g. stream length, discharge, number of flow origins and connectivity). Consequently, due to the heterogeneity of the available datasets, comparative analyses and quantitative syntheses of the observed patters of river network dynamics across different geographic areas are lacking. On the other hand, currently available definitions of ephemeral and intermittent water courses are often qualitative (e.g. Wiginton et al. 2005; Datry et al. 2016; Jensen et al. 2017). In many cases, the attribution of a stream class is performed based on specific hydrologic indexes, including the number and duration of dry spells (Osterkamp et al. 1982; Uys et al. 1997; Svec et al. 2005; Wohl 2017; Kaplan et al. 2019), or using ad-hoc ecomorphological indicators (Hansen 2001; Gallart et al. 2012; Leigh et al. 2016; Stromberg et al. 2016; Levick et al. 2018; Stubbington et al. 2019; Gallo et al. 2020). While existing classification approaches were mainly developed based on discharge records and in-situ field inspections, hybrid frameworks that combine experimental observations and modeling tools can also be found in the literature (Williamson et al. 2015). Nonetheless, comparative studies for the development of general criteria for the classification of temporary watercourses and the identification of targeted policy actions are still lacking.

Existing classifications tools for temporary rivers share the adoption of a local per-

spective, according to which a stream type is associated to every single river segment (or reach) in a network, depending on the hydrologic and ecologic regime observed in that particular location. While extremely useful, reach-wise classifications are difficult to extrapolate in space (Levick et al. 2018; Gordon et al. 2003) as the resulting stream types might be highly heterogeneous along the stream network e.g. owing to the internal geological complexity of a catchment. Moreover, local approaches do not take into account the status of the river network upstream of the focus stretch, which instead might be highly influential for a proper definition of the ecological and biogeochemical function of streams. The advantages implied by the adoption of a network-scale perspective in the classification of temporary rivers have been already discussed in the literature (González-Ferreras et al. 2017), even though the practical efforts made by the scientific community in this direction are relatively limited. The total flowing length of a drainage network, L, and its temporal variability represent important spatially integrated characteristics of temporary streams. A proper characterization of the dynamics of L allows direct inference on the catchment-scale effect of the expansion and contraction cycles experienced by the flowing network in response to unsteady hydro-climatic conditions. Besides, the active channel length and its temporal variations exert a fundamental control on a number of factors relevant for the temporal evolution of the stream water quality, including the distribution of catchment-scale travel times (Van Meerveld et al. 2019), the strength of hillslope-channel connectivity (Soulsby et al. 2011) and the magnitude of important biogeochemical processes contributing to the metabolism of rivers (Botter et al. 2010c; Kiel et al. 2014; Bertuzzo et al. 2017). Even though the total active length of a temporary stream has been linked to the corresponding catchment discharge using empirical power-law relationships (Godsey et al. 2014), a joint probabilistic description of the temporal variations in the hydrological response of a catchment and the corresponding changes in the active network length is lacking. Moreover, network-scale classifications of temporary streams based on the total active length that is involved in the hydrologic response of a given catchment have never been developed.

Despite the lack of standard tools, in recent years there have been couple of practical attempts to reproduce the full spatial and temporal dynamics of the actively flowing channels within specific river networks: i) Ward et al. 2018 used a detailed, physically-based, distributed model that simulated surface water-groundwater interactions and active length variations along a 2.9 km channel in the western Cascades, Oregon, USA, and ii) Jensen et al. 2018 created a logistic regression model that combined catchment discharge measurements and spatial patterns of morphometric attributes, which can potentially be used to simulate network dynamics. These modeling attempts were extremely valuable in clarifying the major climatic and geologic determinants of stream network expansion/retraction; however, these models can hardly be generalized and used for predictive purposes outside the specific context in which they were conceived, in particular for applications to study sites where empirical data on network dynamics are lacking. Moreover, the existing literature lacks of stochastic approaches capable of linking the spatial and temporal dynamics of the active portion of the river network to the underlying rainfall and streamflow

regimes. This emphasizes the need for developing general but parsimonious models - potentially applicable even to ungauged locations - for the synthetic generation of long-term scenarios representative of different hydrologic and active length regimes.

In freshwater ecology, landscape connectivity and suitability are two of the main determinants of species dispersal. These attributes are known to influence the persistence of aquatic populations and communities across a variety of hydrologic systems (e.g. Fagan 2002; Campbell Grant et al. 2007; Datry et al. 2016). River networks, owing to its seemingly fractal nature, are able to create key preferential pathways for the propagation of species within 2D domains, leading to important consequences for biodiversity, species persistence and stability (Todd et al. 2010; Mari et al. 2014; Terui et al. 2018; Rinaldo et al. 2018). While the spatial dimension of stream networks has been extensively analyzed in the literature, their temporal dynamics, implied by the ever-changing wetness conditions in the surrounding landscape, historically received much less attention by the ecological community. In particular, temporary streams ensure dynamic conditions to species, potentially generating transient connectivity windows and ephemeral dispersal opportunities available only when the flowing network reaches its maximum extent (Fahrig 1992; Zeigler et al. 2014; Martensen et al. 2017). Streams that periodically experience dry conditions, on the other hand, may temporarily reduce the number, size and connectivity of suitable habitat patches (Boulton et al. 2017; Garbin et al. 2019). The long-term persistence of a metapopulation arguably reflects the interplay between the extent of habitat fluctuations and the dispersal ability of the focus species (Perry et al. 2019; Abbott 2011; Mari et al. 2014; Unmack 2001). Therefore, characterizing the joint dynamics of a temporary stream and its aquatic metapopulation require the development of inter-disciplinary approaches at the interface of ecology and hydrology, able to capture how hydroclimatic fluctuations are perceived by the organisms hosted by river networks. This also represents a prerequisite for the definition of optimal management and conservation strategies in riverine ecosystems. The ecological implications of spatio-temporal variability in habitat suitability and connectivity have been already analyzed in the ecohydrological literature (Fagan et al. 2009; Zeigler et al. 2014; Mari et al. 2014; Stoffels et al. 2016; Zhou et al. 2017; Lowe et al. 2019; Giezendanner et al. 2021; DeAngelis et al. 2010; Bertassello et al. 2019; Bertassello et al. 2020; Bertassello et al. 2021). However, the question of how population occupancy and persistence respond to the dynamic habitat changes and fragmentation observed in temporary streams is still unanswered. Until now, addressing the above key ecological issue was not possible, in the absence of a model for the long-term simulation of hydrologically-driven fluctuations in the extent and configuration of the flowing stream network (see e.g. Giezendanner et al. 2021).

This thesis provides a series of methods and tools for the study of temporary streams, starting from experimental activities. By introducing a general theoretical framework, analytical results and mathematical tools are developed, unveiling the role of climate on stream dynamics. The proposed approach delineates the possible regimes of the flowing portion of a river, enabling quantitative comparisons between different streams, and facilitates the spatio-temporal modeling of temporary streams. The sound theoretical basis provided by this framework may offer useful insights on the

complex inner-workings of dynamic river networks, possibly serving as guidance for the development of new policies for the protection and management of temporary steams.

1.1 Aims and objectives

The overarching goal of this thesis work is to provide a comprehensive analysis of the physical drivers, dynamic characters and ecohydrological relevance of temporary streams. More specifically, the key objective is to provide a new framework that can serve as a basis for the description and modeling of dynamic river networks, regardless of the spatial and temporal scales of interest, which may range from one hectare to tens of square kilometers, and from a single rainfall event to seasonal or inter-annual timescales. The goal is pursued through a combination of theoretical, statistical and stochastic approaches for the development of quantitative tools to characterize the dynamics of a stream network, and to link such dynamics to other hydrologically relevant quantities such as streamflow and antecedent precipitation. The specific research objectives of this thesis can be summarized as follows:

- to assemble and analyze a unified empirical dataset regarding the dynamics of temporary stream networks in a set of representative study sites around the globe, characterized by heterogeneous climates, geologies and land covers, spanning multiple years of observations and employing different techniques;

- the development of a new theoretical framework to identify the mathematical link between the overall dynamics of a stream network and the behaviour of each single stream reach within the network, providing novel insights on the local features of a river basin that prove meaningful at the network-scale;

- to identify the general schemes underlying the activation and deactivation of the different branches of a temporary stream, shedding light on the physical processes regulating the local presence or absence of surface flow;

- to develop suitable tools for the quantitative characterization of the variability of the active length, in order to provide a general criteria for a consistent, network-scale classification of temporary streams based on the underlying dynamics of the river network;

- to identify the main physical drivers of network dynamicity, determining the major meteorological variables and the temporal scales over which the expansion/contraction cycles of the stream network take place;

- to enable easy and efficient spatio-temporal modeling of a temporary stream, for the reconstruction of the continuous dynamics of a river network from a limited number of field surveys or for the simulation of such dynamics under a broad range of climatic settings

1.2 Thesis structure

The presentation of the research in this thesis is structured as follows.

Chapter 2 illustrates the experimental activities that allowed the collection of empirical data on a set of study catchments. In particular, visual field surveys and water presence sensors were employed to characterize the variability of the status of the stream networks over time.

Chapter 3 then describes the location, climate and main hydrogeological characteristics of each study catchment, as long as the specific available data and study period.

Chapter 4 develops a theoretical framework for the description of the main statistical properties of the active length of a dynamic stream network. In particular, the foundations of a general framework are layed out and used to mathematically link the dynamic character of a steam network to the underlying wetting and drying structure of each individual stream reach (Sections 4.1 and 4.1). This framework is then used to identify the hierarchical mechanism of stream activation, a common behaviour of all temporary streams for which the activation and deactivation of stream reaches during the expansion and contraction cycles of the active network happens following a fixed, predetermined order (Section 4.3). The hierarchical activation scheme maximizes the spatial correlation of the status, creating a direct link between the local persistency and the statistics of the active length, and demonstrating that temporary streams are as dynamic as they could possibly be (Section 4.4). Finally, the Stream Length Duration Curve is defined (Section 4.5), and proposed as a tool to quantify the natural temporal variability of the active stream network under a broad range of field settings.

Chapter 5 explores the temporal dynamics of the active length of a temporary stream. A set of empirical models is developed in Section 5.1, with the goals of identifying the main physical drivers and time scales of active length variability. The proposed approach enables the reconstruction of the continuous dynamics of the active length starting from climatic data. Subsequently, the coupled dynamics of streamflow and active length are probabilistically described, identifying a set of possible regimes and providing a consistent network-scale classification of temporary streams (Section 5.2).

Chapter 6 includes the description of two different approaches for modeling the full spatio-temporal dynamics of the active stream network, by combining the findings of the previous chapter with the hierarchical activation scheme. In particular, Section 6.1 presents a data-based method for reconstructing the continuous dynamics on the basis of a limited number of field surveys and climate data. Section 6.2, instead, describes a stochastic model for the simulation of synthetic stream dynamics. An ecological model for metapopulation occupancy is then introduced and applied, with the goal of assessing the fundamental role that stream dynamics play on non-hydrologic processes (Section 6.3).

CHAPTER 7 presents the results of the application of all the tools and models described in the previous chapters on the study catchments. The results are layed out starting from the validation of the hierarchical structuring of temporary streams, with a view to the characterization of the statistics of the active length; then, the temporal dynamics of the active length and their regimes are investigated and, lastly, the full spatio-temporal network dynamics are modeled. In this chapter, a set of synthetic scenarios is also explored and used as a basis for the simulation of metapopulation dynamics on temporary streams under a broad range of climatic settings and length regimes.

CHAPTER 8 concludes the thesis, providing an overview of the major findings reported in this thesis, and discussing possible research topics that could further increase our understanding of temporary streams and their impact on the related landscapes and ecosystems.

2 Experimental activities

This chapter describes the empirical activities used for monitoring the dynamics of the river networks in this thesis. In particular, section 2.1 illustrates the procedure developed for visual field surveys, while the use of custom built water presence sensors is described in section 2.2. Combining direct monitoring activities with existing data about active length dynamics allowed the creation of a unique dataset for temporary streams, that covers a wide variety of settings, encompassing different climates, geologies and land covers.

This dataset offered the opportunity of developing a general theoretical framework for the description of temporary streams, allowing the identification of the main factors and mechanisms driving network dynamics.

2.1 Visual field surveys

The goal of a field campaign is twofold: i) to delineate the geometry of the potential drainage network (i.e. the maximum possible extent of the flowing network), and ii) to map the presence of flowing water during each survey and capture the spatio-temporal variability of the active network. The activities related to the visual field surveys can be subdivided into data collection, network delineation and data analysis, as described in the next paragraphs.

Data collection. The potential drainage network is identified by the presence of either flowing water during at least one survey or permanent channelization signs (e.g. absence of vegetation on a narrow strip of otherwise vegetated terrains, concave areas with clear continuous channel-like erosion pathways). The geometry of the network is specified by nodes (points) connected by stretches (continuous lines). A node is marked at every channel head (i.e. the upstream point of channelized or potentially channelized reaches), at every confluence point and approximately every 20 m in between. The location of each node is dictated by local properties of the network, such as river meandering or the specific position of wet/dry and dry/wet transitions. Additional nodes are included to better describe the location of surface flow initiation/cessation during each survey. For this reason, the spatial resolution of the surveys is higher than the initial nodes spacing (20 m). Each node is coded as active when there is visible water flow with a minimum width of 10 cm, and dry otherwise. The above width threshold is selected because it was noted that below this threshold the local micro-topography might impact the status of each node by

creating very unstable flow conditions in space and time (ponding/dry/wet) as a byproduct of extremely low flows (e.g., 1 l/min). This threshold is also consistent with the resolutions that can be typically achieved using remote imagery, which is becoming a widespread technique for monitoring network dynamics (such as thermal cameras installed on drones, see e.g. Debell et al. 2015; Spence et al. 2016; Briggs et al. 2019). Each survey lasts a single day, so that uniform hydrologic conditions can be assumed for all the nodes observed in a single survey. The survey consisted in walking the entire length of the drainage network, moving upstream along each tributary and collecting the GPS coordinates of network nodes with the aid of a geotracking device. In addition to mapping the network from the outlet upstream, the hillslopes were also scouted to ensure the mapping of channels that are disconnected from the outlet. The scouting was informed by vegetation greenness patterns derived from satellite imagery and by a reference network extracted from the DTM, with a very small threshold on the contributing area (0.5 ha). Nevertheless, all the hillslopes and areas far-away from the connected network in the upper part of the basin were also monitored by hiking the whole catchment area to avoid under-representation of existing channels.

Network delineation. Stream network maps were obtained combining information from field surveys and remotely sensed imagery, including a high resolution DTM and an orthophoto. The DTM is pre-processed using a pit removal algorithm: a threshold of 300 m^2 was chosen on the basis of field observations to discriminate between real pits (not removed by the algorithm) and artifacts of the DTM that should be removed. Flow directions were then calculated using the D8 algorithm (Ocallaghan et al. 1984; Tarboton 1996) and manually corrected in 132 pixels on the basis of field observations to properly represent local anomalies in the observed drainage network, due to human interventions (e.g. presence of roads and hiking trails). Finally, the contributing areas were calculated for each cell based on the corrected flow directions.

The coordinates of the field-collected nodes were adjusted by snapping the nodes over pixels of the DTM where accumulation of the contributing area occurs. Orthophotos were also used to ensure the correct positioning of each node. Maximum horizontal corrections were below 10 m, consistent with the positioning error of the system used for the field surveys. The corrections applied to the flow directions and the adjustments on the coordinates of field-mapped nodes ensured that DTM-derived information and data from the field surveys were consistent with each other.

The drainage network was then delineated by connecting all the nodes with stream stretches, following flow directions along individual streams. Each stretch of the network was considered as active during a given survey only if both the upstream and downstream nodes were simultaneously active.

Preliminary data analysis. To quantify the dynamics of the stream network, a persistency index (P_i) was calculated for each stretch (i) dividing the number of times the stretch i was active by the total number of field surveys. P_i represents the percentage of surveys during which a stretch was active and, under the ergodic assumption, it provides an indication of the probability of that stretch being active

during the campaign. The idea of quantifying the probability of network activity through spatial maps was first introduced by Jensen et al. 2017, even though in that case such probabilities were derived from the flow duration curve, whereas in this work maps of P_i were calculated directly from observational data. While still relying on the assumption that the available surveys properly represent the temporal variability of the status of each node, this method relaxes the additional hypothesis that a unique active network configuration exists for a given discharge at the outlet. Stretches with $P_i = 1$ were classified as persistent, while stretches with $0 < P_i < 1$ were coded as temporary; stretches with $P_i = 0$ were indicated as dry, to underline the fact that they were inactive in all the field surveys. It must be noted that the value of P_i depends on the number/dates of field surveys conducted. Accordingly, a stretch classified as persistent (or dry) in this study may become temporary after the completion of additional field campaigns.

Five key properties of the drainage network were calculated for each field survey:

a) *active length* (L [km]): the total length of the active drainage network on a given date;

b) *active drainage density* [km^{-1}]: L divided by the catchment area;

c) *active disconnected length* (disconnected L, [km]): length of the active drainage network that is not connected at the surface to the outlet;

d) *number of active channel heads*: the number of origins of the active drainage network, hereafter named sources, including all the points in which surface flow resumes downstream of a disconnection along the potential network;

e) *disconnected clusters*: the number of contiguous parts of the active network that are disconnected from the outlet.

The mean and variance of L were also calculated, to be used as indicators of the mean drainage density and the extent of stream network dynamics.

2.2 Water presence sensors

While visual field surveys allow the delineation of the potential drainage network, their main limitation is the required effort, which seldom allows for a continuous monitoring of the dynamics of a temporary stream with high temporal resolutions. An alternative possibility is given by water presence sensors (as seen in Figure 2.1) which continuously monitor the presence of flowing water in a set of prescribed nodes.

Sensor design and deployment. Usually, these sensors are based on Onset HOBO Pendant loggers (HOBO UA-002-64, Onset Computer Corp, Bourne, MA, USA, hereafter HOBO) and suitably modified following the methodology suggested by Chapin et al. 2014. The main changes introduced in this study consisted in removing the light sensor and adding two long electrodes, which recorded a positive electrical signal when connected by the flowing water. The obtained electrical

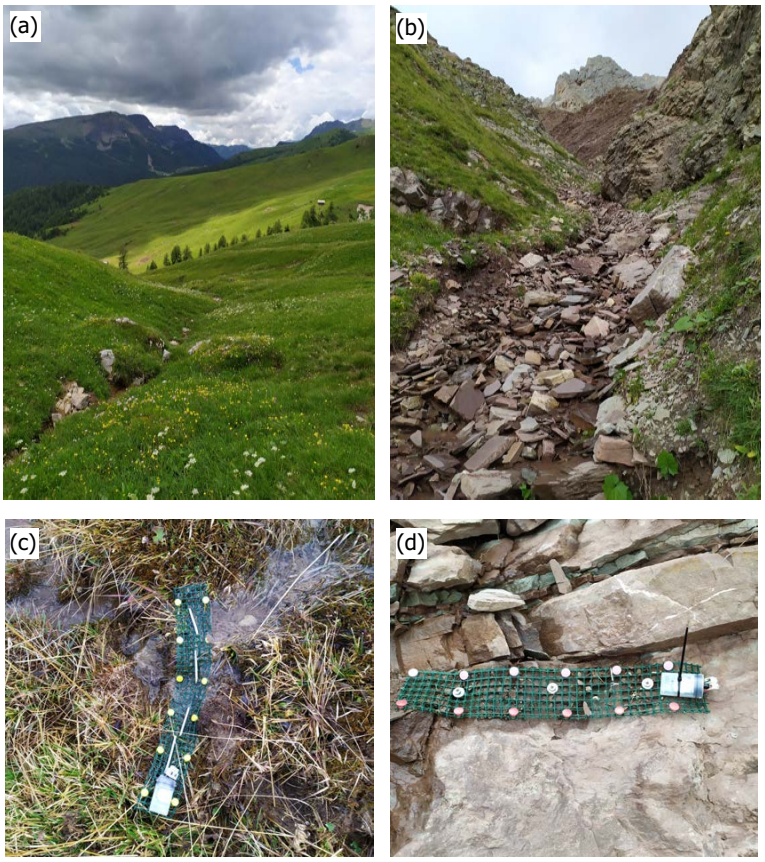

Figure 2.1: Sensors placed along the tributaries of the Rio Valfredda. Left: picture of Zone 1 (a) and a sensor on the grass (c). Right: picture of Zone 2 (b) and a sensor screwed on a rock (d).

resistance (ER) sensors were placed along the river networks to estimate flow intermittency within different network nodes. The electrical conductivity signal recorded by the HOBO ranged from 0 to 330000 lux (corresponding to the maximum value recorded by the sensors when the two electrodes were fully immersed in water) and the temporal sampling resolution was set to 5 minutes.

The river bed of dynamic headwater streams is usually highly heterogeneous, and hydro-morphodynamical variations induced by changes in flow magnitude might cause the flowing water to dodge the sensors, thereby impairing the reliability of the recorded data. To avoid cases in which water flow paths could bypass the sensors, particularly during low-flow conditions, a novel experimental setup is identified. It allows the monitoring of the hydrological state of the whole cross-section where the sensors as placed. The two machine pin electrodes coming out of the sensors' housing cap are connected with two stainless steel wires, from 50 cm to 100 cm long, rolled up to a geotextile net. The length of the geotextile and wires guaranteed that the entire cross-section of the channel are connected to the sensor avoiding interference due to possible variations of the flow field. Rolling the cables on the net prevented them from moving when flooded, possibly creating artificial short circuits or bypasses that might impair the reliability of the electrical signal recorded. The net is then attached to another geotextile using plastic buttons to separate the electrodes from the ground by a few millimeters (and avoid interference with the wet soil).

When placed in field, HOBOs are secured to their networks with suitable plastic strips; silicon is used to protect all the sensors' housing caps and prevent infiltration of water within the loggers. The nets are then screwed on rock emergencies or fixed on the stream bed using pickets, depending on the specific substrate in the location of the deployment (see panels (c) and (d) of Figure 2.1 for two different examples in the Valfredda catchment).

Preliminary data analysis. Two hydrologically-relevant indexes are calculated from the time series collected by the HOBOs: the *average intensity (AI)* and the *exceedance of the threshold (E)*. *Average intensity* is the mean of the electrical signal registered by each HOBO in the period of record. *Exceedance of the threshold* is the probability that the electrical signal registered by a sensor is greater or equal than a chosen threshold value, separating the wet condition from the dry condition, which is chosen based on the intensity measured by the instruments placed in wet nodes during the field surveys. The threshold value is inferred directly from field observations, instead of relying on laboratory experiments (e.g., with a soil column), to get a more reliable representation of the complexity of the natural environments typically found in most headwater catchments of the Alpine region. The above hydrological indexes (AI and E) are calculated for each ER sensor and subsequently correlated with the persistency of the corresponding nodes which was estimated from field surveys.

A visual representation of spatial and temporal dynamics of the river network is obtained based on the intensity signal recorded by the HOBOs. For each time of the surveyed period, the electrical signals recorded by each sensor and its neighbours were interpolated in space, in order to define which part of the stretch connecting the nodes is wet or dry. The exceedance of the threshold by the electrical signal is used to determine the wet or dry status of the stretches. Probes were divided into three categories, depending on the electrical signal recorded:

- *active*, when the value of intensity was greater than the threshold and the cross-section where the HOBO was placed was identified as wet;
- *inactive*, when the signal collected was lower than the threshold and the cross-section was identified as dry;
- *missing data*, when the sensor didn't provide reliable data. These occurrences are mainly related to accumulation of sediments around the geotextile or detachment of the probes from the loggers by grazing animals.

A river stretch is identified as a reach connecting two subsequent HOBOs. When two neighbouring sensors are both active, inactive or missing data, the stretch in between is defined as active, inactive or missing data accordingly. Instead, if two neighbouring HOBOs have data but one of them is active and the other inactive (or when a sensor with missing data has two neighbouring HOBOs providing reliable data), the wet length in the stretch connecting those sensors is calculated using a linear interpolation of the electrical signal measured by the nearest probes. Whenever a stretch has both missing data sensors at its end points and it is located between two concurrently active or concurrently inactive stretches, it is classified as active

or inactive accordingly. Instead, if a stretch with missing data is located between two stretches with a different status (i.e., one active and one inactive), it is kept as a stretch with missing data, as the available data did not allow a proper identification of the status of the sensors and the location of the wet-dry transition. This method can't be applied to stretches classified as missing data if they are located at the sources or in presence of confluences. In these cases, the behaviour of the neighbouring stretches, experimental evidences and the observed spatial patterns of persistency are considered in order to define the status of the stretch (active, inactive or missing data). Finally, a MATLAB code is used to obtain time-lapse visualization of the stream network dynamics with the desired temporal resolution (e.g. 3 hours).

3 Case studies

The empirical activities depicted in the previous sections enabled the compilation of a dataset comprising 18 different study catchments located in Europe and eastern USA, spanning a wide range of latitudes, climates, land covers, geologies and sizes (see Figure 3.1 and Table 3.1).

Section 3.1 provides a detailed description of the Valfredda catchment and all the specific empirical activities carried out in this site from 2018 to 2021 for monitoring the dynamics of the active network and other hydrologically-relevant variables (e.g. precipitation, evapotranspiration and streamflow). Section 3.2, instead, contains a description of all the other study sites included in this thesis, as well as the related available empirical data.

3.1 The Valfredda catchment

The Rio Valfredda is a small alpine creek in northern Italy belonging to the Piave river basin (Figure 3.2, for more details on the basin the reader is referred to Botter

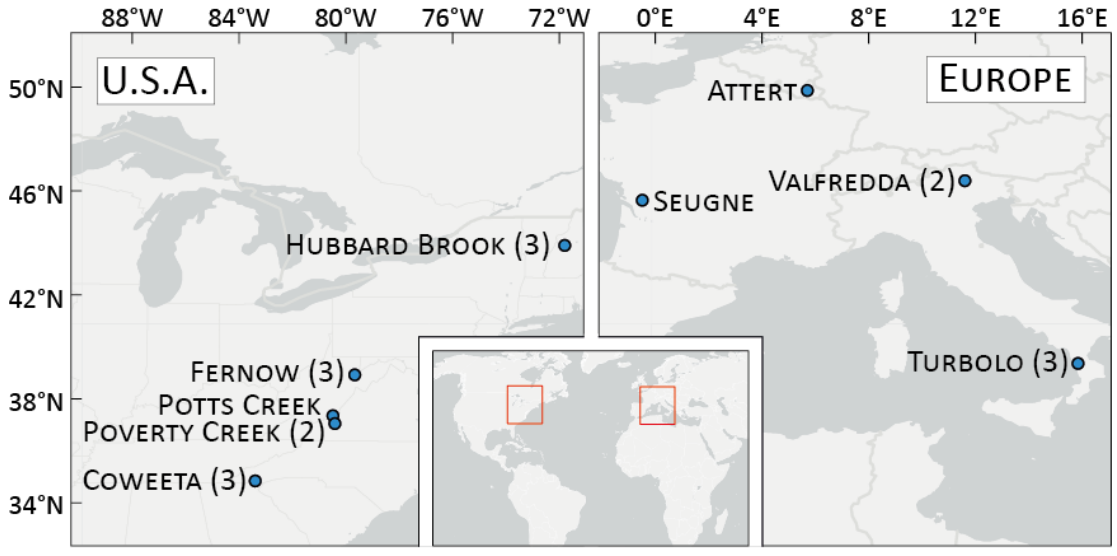

Figure 3.1: Geographical location of the study catchments across Europe and eastern USA. The number of case studies for each location is indicated within round brackets only when this number is larger than one.

et al. 2010a; Lazzaro et al. 2013). The catchment elevation ranges from 1500 to 3000 m a. s. l., with a maximum drainage area of 5.3 km^2. The geomorphic network is 16.8 km long, corresponding to a geomorphic drainage density D_g of 3.16 km^{-1}. Lithology and vegetation cover exhibit significant spatial heterogeneity across elevations, shaping the hydrological dynamics of the basin. On the uplands, deposits of gravel and rocky debris, originated from the erosion of solid rock emergencies near the divides, dominate. These deposits are covered by shallow and patchy pastures generate karst areas that ensure a high soil permeability, thereby promoting the infiltration of most part of the precipitation (as confirmed by the results of the field campaign). Below 2400 m a. s. l., soil covers a sedimentary bedrock with trees growing adjacent to the streams. The lower part of the catchment (below 2000 m a. s. l.) is characterized by an almost impermeable pyroclastic bedrock and a forested cover (as shown in Figure 3.2). There are several springs supplying aqueduct intakes, which collectively withdraw a flow rate that is two orders of magnitude smaller than the stream discharge at the outlet. Accordingly, the effects of these intakes on stream network dynamics were neglected.

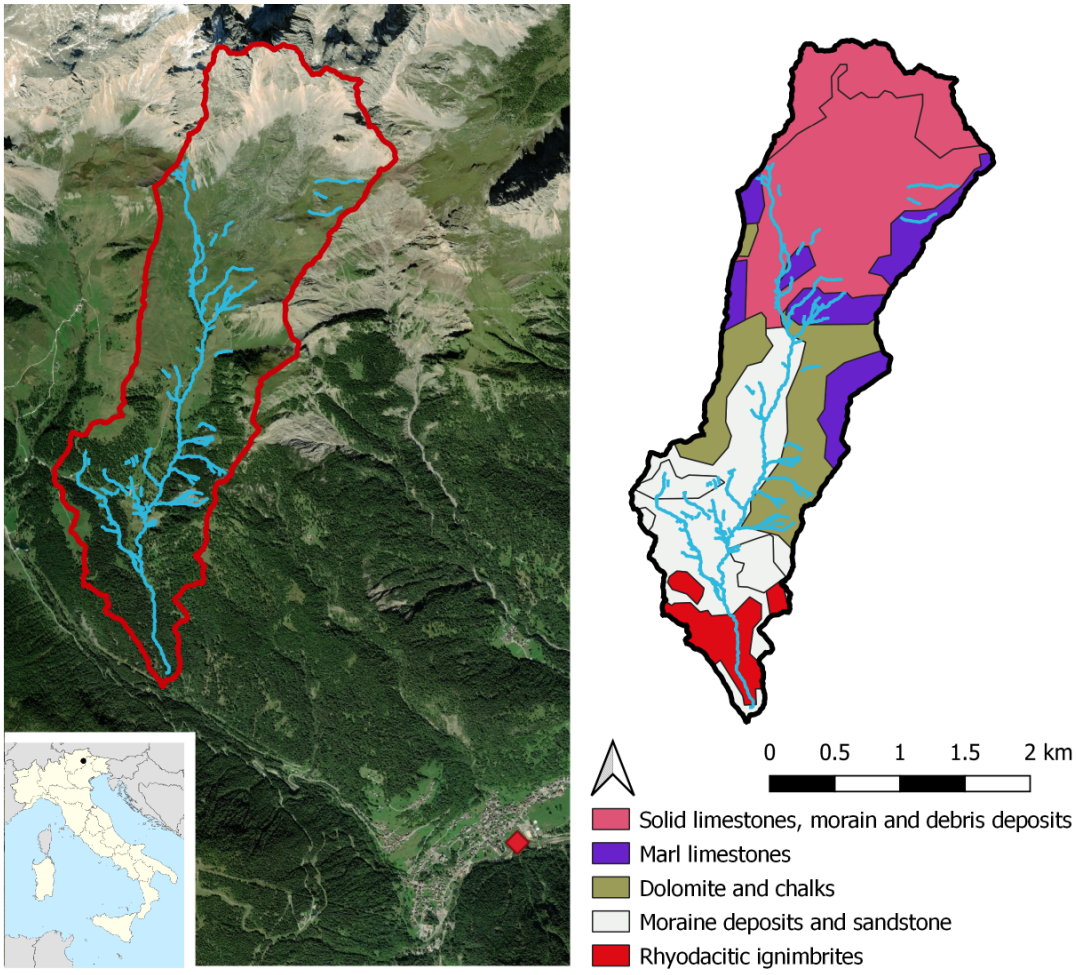

Figure 3.2: Left: ortophoto showing the different land covers of the Valfredda river catchment and its location in Italy. Catchment boundaries are depicted with an orange line; light blue lines represent the potential river network as surveyed; the red marker shows the position of the weather station. Right: geologic map of the area.

The site has an alpine climate, characterized by high precipitation throughout the year (annual rainfall of about 1500 mm), with significant snowfall during winter and melting in spring. The hydrological regime exhibits a strong seasonality, with winter low flows (when the whole catchment is covered by snow) followed by higher discharges during spring and summer. Because of low recession rates in winter and high rain frequency in the other seasons, intra-seasonal flow regimes are mainly persistent (sensu Botter et al. 2013).

Climatic data. Climate data were monitored by a weather station of the Veneto Region Environmental Protection Agency (ARPAV) located in Falcade, 4.5 km far from the catchment centroid (Figure 3.2). These data are characterized by a daily resolution and are available since 2010. Monitored variables include precipitation, temperature, relative humidity, solar radiation, wind speed and direction. These data were analyzed to characterize the climatic regime of the study catchment, especially during the first year of field campaign (summer-fall 2018). Two additional weather stations were installed within the catchment area in 2019, after part of the field campaign described in this paper. Precipitation records gathered by these instruments were compared with the corresponding time series of the ARPAV weather station to ensure that the data used in this study represent sufficiently well the dynamics of the water input in the study catchment (see SI). The morphology of the Valfredda was characterized via a LiDAR survey that was carried out in October 2018 to produce a high resolution (20 cm) Digital Terrain Model (DTM) and a corresponding orthophoto.

Streamflow. Discharge measurements were taken in two cross-sections, one at the outlet of the study catchment and one at about half of the maximum drainage area, where water flows permanently. A pressure transducer allowed the measurement of the water stage with a temporal resolution of 5 minutes. A total of 28 streamflow measurements were performed under different hydrologic conditions using either a three dimensional Acoustic Doppler Velocimeter or the salt dilution method. Streamflow measurements were combined to stage data, to estimate the rating curves at the two measuring stations with discharge ranging between 9 and 620 l/s and a coefficients of determination $R^2 = 0.99$. Discharge time series were then derived for the entire study period with a temporal resolution of 3 hours, so as to reduce the noise in the recorded signal. The same method was applied to measure the constant discharge originated by the localized springs that feed the permanent fraction of the river network.

Visual field surveys. The active portion of the river network has been surveyed 32 times from July 2018 to November 2021, following the procedure described in section 2.1; the specific date of each survey was selected on the basis of the antecedent precipitation in order to maximize the variability of the observed conditions. An additional survey was performed in January 2019, while the catchment was covered by snow. This survey was not used for modeling purposes, but only to obtain an estimate of the extent of the drainage network during the winter time (i.e. from December to May), when the network remains almost steady due to the winter freezing. For more detailed information about the Valfredda catchment the reader is referred to Durighetto et al. 2020.

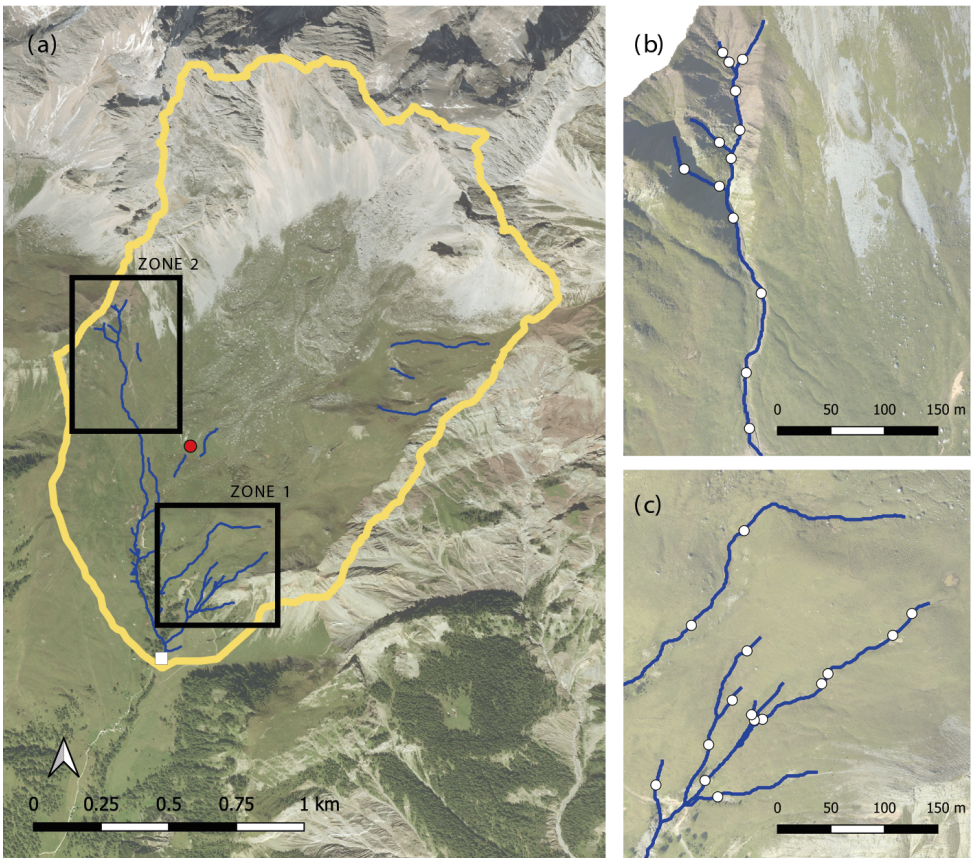

Figure 3.3: (a) Ortophoto of the upper Valfredda catchment, position of the meteorological station (red dot) and of the section where discharge measurement were taken (white square). (b) Location of the deployed sensors within Zone 2. (c) Location of the water presence sensors deployed in Zone 1.

WATER PRESENCE SENSORS. The dynamics of the active stream network during the study period (4th September to the end of October 2019) were observed using 31 water presence sensors, as described in 3.3. The water presence sensors were installed mainly into two different regions of the upper Valfredda catchment, as shown in Figure 3.3. The location of each sensor was chosen based on field surveys carried out prior to the installation of the instruments. Technical difficulties and the time needed to reach each node of the network were carefully considered in the selection process. The specific location of the sensors was also chosen taking into account the heterogeneous substrates of the catchment, so as to enable an accurate analysis of the sensors' behaviour in different settings while granting an even distribution of the nodes' persistency.

Fifteen sensors were deployed along tributaries of the southeastern part of the basin (Zone 1), an area that has glacial morphogenesis and is characterized by moraine deposits shaped on mild slopes covered by pastures (Figure 2.1a); therein, the river width ranges from 20 to 80 cm, and the sensors were fixed to the ground using pickets (Figure 2.1c). This led to a quite uneven spatial distribution of the sensors, with a mean inter-sensors distance of approximately 55 m.

Thirteen sensors were placed in the northwestern part of the network (Zone 2),

where the riverbed is on a steep canyon composed of quartz porphyry rocks (Figure 2.1b). These rocks are small and unstable, and they can move along the channel in response to rainfall events, thereby supporting the intermittent nature of hydrologic flows. In this region, the channel width ranges from 20 cm to about 1 m and the sensors' net were screwed on rock emergencies (Figure 2.1d). In Zone 2, the criteria used in the selection of the HOBOs' positions were the same as for Zone 1. However, in this case, a more even spatial distribution of the ER sensors was obtained, with a smaller mean inter-sensors distance (30 m).

The other 3 sensors were installed along three disconnected branches of the network on the grassland between Zone 1 and 2. Some of the tributaries of the Valfredda Creek were monitored only through visual inspection, as field surveys allowed a simple yet reliable characterization of the hydrological conditions experienced by those reaches during the study period (they were permanently wet even under extreme low flow conditions or they were completely dry even during the most intense precipitation event of the entire period).

3.2 Other study sites

The empirical dataset used in this thesis comprises not only the Valfredda, but also other 16 experimental sites in Europe and USA. A summary description of each study site is reported below, as long as the characterization of the experimental data that is available for each catchment (in particular, active length data). Furthermore, a summary of the long-term climatic, hydrological and geological characteristics of the sites is reported in Table 3.1.

3.2.1 Turbolo

The Turbolo creek is a small river located in southern Italy, where the climate is Mediterranean with hot summers; its drainage area is approximately 7 km^2 at the outlet of Fitterizzi, with elevations ranging between 183 and 1005 $ma.s.l.$. The empirical data used in this study refers to two sub-basins in the northern part of the catchment, with contributing areas of 0.67 and 0.48 km^2 (catchments T_1 and T_3, respectively). A third catchment (T_2), nested into T_1, has also been identified to capture the effects of the internal heterogeneity of geology and land cover in the study area. The T_2 catchment drains an area of 0.23 km^2 only. The Mediterranean climate of the area consists in hot and dry summers with wet, mild winters. The annual precipitation is approximately 1200 mm, but due to high evapotranspiration rates a complete dry-down of the network is observed during the summer. The T catchments are dominated by silty marly clays with low permeability, that generate (jointly with the aridity of climate) streams with very low persistency. The geomorphic drainage densities in this site range between 2.8 and 5.6 km^2. The upper part of T_1 is composed by sandy-conglomerate formations, in which the higher permeability produce a relative increase in the persistency of the stream network. The catchments T_1 and T_2 have been monitored for 35 times from April 2019 to January 2020, while T_3 was monitored for 42 times from May 2019 to January 2020. For more information

on the Turbolo catchment the reader is referred to Senatore et al. 2021.

3.2.2 Hubbard Brook

Three US catchments considered in this study pertain to the Hubbard Brook Experimental Forest of New Hampshire (New England). In the paper, they have been identified as H_1, H_2 and H_3, and their contributing areas are 0.14, 0.25 and 0.42 km^2, respectively. The mean altitude of these catchments ranges between 630 and 740 $ma.s.l.$, with average slopes of 28%. The stream networks of these catchments are the densest of the dataset, with geomorphic drainage densities of 12.5, 14.5 and 8.9 km^{-1}, respectively. The geology of the sites is mainly composed of shists and granulites, covered by a mantle of sandy loams. The humid continental climate of the area provides a mean annual precipitation of 1400 mm, with cold snowy winters and mild summers. For each catchment, 7 visual monitoring of the active network have been carried out in June and July 2015, spanning a wide range of hydroclimatic conditions. More information on this catchments is available in Jensen et al. 2017.

3.2.3 Fernow

The Fernow Experimental Forest is located in the Appalachian Plateau of West Virginia (USA). In this site, three study catchments (F_1, F_2, F_3) have been selected, with drainage areas of 0.14, 0.16 and 0.37 km^2, respectively. These catchments have a mean altitude of approximately 800 $ma.s.l.$, with slopes around 30%. Field observations revealed geomorphic drainage densities of 2.9 km^{-1} with local persistencies varying in the full range between 0 and 1. The bedrock is composed of shales and sandstones, with a soil cover consisting mainly of silt loams. The average annual precipitation is approximately 1450 mm, with rainy summers and mite winters. Snowfalls are common but usually limited and isolated. From May to December 2016 a total of 7 field surveys per catchment were carried out. More information on this study site can be found in Jensen et al. 2017.

3.2.4 Potts and Poverty

Three study catchments are located in the Valley and Ridge physiographic provinces of Virginia (USA). Two of them (P_1 and P_2) are part of the Poverty Creek, while the third (P_3) belongs to the South Fork Potts Creek, 25 km northern of P_1 and P_2. These catchments have a contributing area of 0.25, 0.35 and 0.73 km^2, respectively. P_1 and P_2 have and average elevation of 750 $ma.s.l.$, a mean slope of 33% and a geomorphic drainage density of 7 km^{-1}. The Potts Creek catchment, instead, has a higher elevation (1030 $ma.s.l.$) and gentler slopes (27%). Its geomorphic drainage density is 2.9 km^{-1}. Bedrocks are mainly composed by sandstones in all the catchments, whereas shales and siltstones can be found in the P_1 and P_2 sites. The average annual precipitation in the area is close to 1000 mm, remarkably lower than all the other USA catchments considered in this study (and comparable with the T sites in southern Italy). Unlike the Turbolo Creek, however, the drainage networks do not experience summer dry down due to the lower evapotranspiration rates. The

active network in these catchment has been monitored by visual inspection 7 times between September 2015 and March 2016. More information about these study sites can be found in Jensen et al. 2017. In the $P2$ site, network dynamics were also monitored with a network of 51 water presence sensors between May 2017 and February 2018 (Jensen et al. 2019).

3.2.5 Coweeta

The C_1, C_2 and C_3 catchments are located in the Coweeta Hydrologic Laboratory, North Carolina (USA). They are the highest and steepest USA sites considered in this study, with mean elevations between 800 and 1100 $ma.s.l.$ and slopes of about 50%. These sites have areas of 0.12, 0.33 and 0.40 km^2, respectively, and drainage densities ranging between 3.6 and 6.2 km^{-1}. The catchments lie on the Southern Blue Ridge Mountains, which mainly consist of exposed metamorphic rock (biotite gneiss and amphibolite). The climate is generally warm and humid, with temperatures above $0°C$ all year round. The precipitation is greatest in winter and early spring, with an average annual precipitation of about 1800 mm. The field campaign for detecting the active stream network in these sites were carried out from November 2015 to December 2016, and consisted in 7 field surveys for each catchment. More information about these study sites can be found in Jensen et al. 2017.

3.2.6 Attert

The Attert catchment (catchment code A) covers an area of 247 km^2 between Luxemburg and Belgium. The altitude ranges between 245 and 550 $ma.s.l.$ and the geology is dominated by slate, marls and sandstone, while lithology is driven by land use (mainly forest and agriculture). The climate is characterized by wet winters and mild summers, with an average annual precipitation of 900 mm uniformly distributed throughout the year (Pfister et al. 2017). Different types of sensors were employed in this catchment (time-lapse photography, conductivity sensors and water level gauging stations) to monitor flow presence in a set of 182 nodes along the network. These sensors recorded water presence at a 30-minute time interval from 2013 to 2017. The sparse arrangement of the sensors along the network didn't allow a proper calculation of the active length. Therefore this data was only used to validate the hypothesis of hierarchical activation of the stretches. Detailed information about this catchment can be found in Kaplan et al. 2019.

3.2.7 Seugne

The Seugne river is located in the Charente-Maritime département in west France. The catchment (hereafter coded as S) has a contributing area of 920 km^2, with elevations that span between 8 and 160 $ma.s.l.$. The geology is composed of limestones, carbonates, sedimentary rocks and sand. The climate is Marine West Coast. The active network was monitored in the catchment as part of the Onde campaign. Visual inspection observations were employed determine water presence in a set of

40 predetermined nodes, at a monthly interval from 2012 to 2020. As for the Attert catchment, this data was only used for validating the hierarchical hypothesis because the sparse monitoring points did not allow the calculation of the active length. More information about the field campaign can be found in *Observatoire national des étiages (ONDE) dataset* n.d.

Table 3.1: Summary of the main climatic, hydrological and geologic characteristics of the study catchments (NA = data not available). Note that the mean climatic attributes reported here are long term averages and do not refer to the study period only.

Catchment code	**Area** $[ha]$	**Mean elevation** $[m\,a.s.l.]$	**Mean temperature** $[°C]$	**Mean precipitation** $[mm/month]$	**Mean evapotrans.** $[mm/month]$	**Mean streamflow** $[mm/month]$	**Runoff coefficient**	**Aridity index**	**Geology**
A	24700	350	9.6	74.6	51.3	36.3	0.47	1.45	Marl, slate and sandstone
C_1	12	823	13.7	226.0	68.2	172.5	0.76	3.31	Gneiss
C_2	33	1019	13.8	229.7	77.8	160.5	0.70	2.95	Gneiss
C_3	40	1052	11.9	285.3	56.1	214.4	0.75	5.08	Gneiss
F_1	14	773	15.6	144.1	83.0	58.1	0.40	1.74	Shale rocks
F_2	16	767	15.6	144.9	86.4	40.4	0.28	1.68	Shale rocks
F_3	37	822	15.6	146.5	86.4	39.5	0.27	1.69	Shale rocks
H_1	14	690	16.2	163.7	104.2	87.2	0.53	1.57	Mudstone and shists
H_2	20	740	17.1	209.8	119.0	117.1	0.56	1.76	Mudstone and granite
H_3	43	632	16.2	162.8	103.4	85.2	0.52	1.57	Shists and mudstone
P_1	25	750	10.1	73.2	55.8	69.4	0.95	1.31	Shale rocks
P_2	35	729	14.2	77.4	69.0	32.1	0.41	1.12	Shale rocks
P_3	73	1029	NA	NA	36.4	57.6	NA	NA	Sandstones
S	91950	100	17.3	62.7	NA	NA	NA	NA	Limestones
T_1	63	263	17.2	87.8	109.5	47.6	0.54	0.80	Clays
T_2	23	250	17.2	87.8	109.5	47.6	0.54	0.80	Clays
T_3	46	358	17.6	88.3	112.9	48.9	0.55	0.78	Clays
V	527	2250	7.6	152.7	47.8	86.4	0.57	3.19	Limestone and sandstone

4 Theoretical framework

The available data about the active portion of the stream network lied at the basis of the development of a general theoretical framework for the mathematical description of network dynamics. In particular, the aim of this chapter is to provide an analytical characterization of the statistics of the active length (i.e. mean, variance and probability density function), on the basis of the statistical properties of the nodes that belong to the network. The general framework introduced in this chapter is further expanded in chapter 5, which describes the temporal dynamics and regimes of the active length, and in chapter 6 where the full spatio-temporal dynamics of the active network are modeled.

This chapter is structured as follows: the general theoretical framework is introduced in section 4.1, while a simplified, Bayesian version of such model is derived in section 4.2. The introduction of the hierarchical behaviour (section 4.3) allows the specification of a general mechanism according to which networks expand and contract. The hierarchical structuring of network dynamics enables a significant simplification of the analytical expressions derived in this thesis. Then, the statistics of the active length are linked to the local persistency of the nodes of the network (section 4.4). Last but not least, the Stream Length Duration Curve (SLDC) is defined in section 4.5. The SLDC is proposed as a general tool to quantify the temporal variability of the active length in a broad range of settings, allowing objective comparisons between different catchments.

4.1 General framework

Let me define a dynamical stream network through a set of N nodes with arbitrary spatial coordinates within a 3D space, representative of the terrain of a given landscape. In this framework, the dynamical nature of the stream network can be probabilistically represented by a random shifting between two possible states associated to each node: “active" or “dry". From a mathematical viewpoint, the river network thus corresponds to a vector of N binary random variables $\boldsymbol{X} = (X_1, X_2, ..., X_N)$, whose components are associated to the N nodes of the network. Specifically, X_k ($k \in (1, N)$) characterizes the local status of the k^{th} node according to the following coding scheme:

$$X_k = \begin{cases} 0 & if\ the\ node\ is\ dry \\ 1 & if\ the\ node\ is\ active \end{cases} \tag{4.1}$$

X_k follows a Bernoulli probability distribution with parameter p_k:

$$X_k \sim p_k^{x_k} \left(1 - p_k\right)^{1-x_k} , \tag{4.2}$$

where x_k denotes a realization of the stochastic variable X_k, and the symbol $\sim$ means “is distributed as". The mean and the variance of the dichotomic process at the node k, X_k, can be expressed as:

$$E[X_k] = p_k$$

$$E[(X_k - E[X_k])^2] = p_k(1 - p_k)$$

where $E[...]$ denotes expectation. Therefore, the parameter p_k in equation (4.2) represents the mean local persistency of the node k (i.e. the average percentage of time during which the node k is active). The mean local persistency (hereafter local persistency) can be estimated from independent field surveys as the sample mean of X_k, i.e. $p_k = \frac{Na_k}{N_k} \in [0; 1]$, where Na_k is the number of surveys in which the node k is active and N_k the number of times the node k was surveyed (see e.g. Durighetto et al. 2020). It is worth noting that the quantity p_k is a local property in space, though temporally integrated.

The length of the active stream network at a given time is crucially dependent on two independent factors, namely i) the fraction of stream length associated to each node and ii) the sequence of nodes active at a given time. In particular, the stream network length L can be expressed as:

$$L = \boldsymbol{X} \cdot \boldsymbol{\Delta l} , \tag{4.3}$$

where $\cdot$ indicates the scalar product and $\boldsymbol{\Delta l} = (\Delta l_1, \Delta l_2, ..., \Delta l_N)$ is a vector of lengths whose components represent the increase of overall stream length produced by the activation of each node of the network. Δl_k can be calculated (for every node) based on the network topology as the sum of the semi-distances between the node at hand and the connected neighboring nodes (upstream and downstream), suitably evaluated along the flow directions. Equation (4.3) shows that, due to the randomness of $\boldsymbol{X}$, the active stream network length is a random variable as well.

The sequence of nodes that are active at a given time can be characterized in a probabilistic way through the definition of the joint pdf of the vector of N random variables X_k , $k \in [1, N]$. The joint pdf of the random vector $\boldsymbol{X}$ is a multivariate Bernoulli distribution, with possibly correlated components. The analytical expression of this multivariate distribution reads (e.g. Dai et al. 2013):

$$p(\boldsymbol{x}) = p_{00...0}^{[\prod_{j=1}^{N}(1-x_j)]} \; p_{10...0}^{[x_1 \prod_{j=2}^{N}(1-x_j)]} \; p_{01...0}^{[(1-x_1)x_2 \prod_{j=3}^{N}(1-x_j)]} \; \dots \; p_{11...1}^{[\prod_{j=1}^{N} x_j]} \tag{4.4}$$

where $p_{abc..z}$ is the joint probability of $X_1 = a, X_2 = b, X_3 = c, ..., X_N = z$ and $\boldsymbol{x} = (x_1, x_2, ..., x_N)$ represents a realization of $\boldsymbol{X}$. In order to fully specify the joint pdf in equation (4.4), the identification of a large number of parameters (2^N) is required. Therefore, the problem can be largely undetermined (i.e. overparametrized) unless further simplifying assumptions are introduced.

The mean network length can be calculated based on the local persistency, taking the expectation of both sides of equation (4.3):

$$\langle L \rangle = \sum_{i=1}^{N} p_i \, \Delta l_i \tag{4.5}$$

Equation (4.5) shows that the mean length can be expressed as a weighted sum of the local persistency along the network. Nevertheless, changes in the state (active vs dry) of the nodes of the network, as induced by the interaction of unsteady climatic forcing (e.g. a random sequence of rainfall events) and local geologic or morphological properties, make the overall length of the flowing streams time-variable. The variability in time of the stream network length can be summarized through the variance of L, that can be estimated from equation (4.3) as the variance of a linear combination of random variables:

$$var(L) = \sum_{i=1}^{N} \sum_{j=1}^{N} \Delta l_i \Delta l_j Cov(X_i, X_j) = \sum_{i=1}^{N} \sum_{j=1}^{N} \rho_{i,j} \Delta l_i \Delta l_j \sqrt{p_i(1-p_i)p_j(1-p_j)} \,, \tag{4.6}$$

where $Cov(X_i, X_j)$ is the covariance between X_i and X_j and $\rho_{i,j}$ is the corresponding cross correlation (i.e. the covariance scaled to the product of the standard deviations of X_i and X_j). Equation (4.6) shows that, differently from the mean network extension, the variability of the stream length through time is crucially impacted by the spatial correlation structure of the sequence of random states X_k along the network.

The temporal variability of the length of the flowing streams can be characterized in a more detailed manner through the probability density function (pdf) of L - or, alternatively, through the corresponding cumulative distribution functions of L (exceedance or non-exceedance probabilities). A general closed-form expression for the exceedance probability of the length of the flowing network, $P_L(L)$, can be written as:

$$P_L(L) = Prob\,[l \geq L] = Prob\,[\boldsymbol{X} \cdot \boldsymbol{\Delta l} \geq L] \tag{4.7}$$

The left hand side of equation (4.7) represents the probability to observe a length of flowing streams larger than (or equal to) L, while the right hand side of the same equation represents the Cumulative Distribution Function CDF of a linear combination of possibly correlated Bernoulli-distributed binary random variables. Were these

binary variables uncorrelated, the pdf of the stream length would be expressed as a convolution of N scaled Bernoulli pdfs, thereby originating a Binomial-Bernoulli distribution when $\Delta l_k = const(k)$. Instead, the presence of mutual correlations among the components of $\boldsymbol{X}$, which is a reflection of the physical mechanisms that underlie river network expansion and contractions, prevents a full analytical treatment of the problem in the general case, unless further simplifying assumptions are introduced (see section 4.3).

4.2 A Bayesian model for dynamic networks

Given the complexity of the physical processes under investigation, a simplified probabilistic description of the nodes state in the network can be helpful to quantify the effect of the expansion/contraction cycles experienced by rivers on the temporal variability of the active stream length. Here, stream network dynamics are described through a spatially-correlated dichotomic stochastic process, in which the state of one node is seen as a binary random variable (active/dry, see equation (4.1)) that is probabilistically linked to the state of another (suitably identified) node in the network. In other words, pairwise joint pdfs representing the status of two connected nodes are identified (Figure 4.1). Considering now a generic couple of directly connected nodes (say, the nodes j and i), the joint probabilities of the state of these nodes are identified by the following elements (Figure 4.1):

- p_{11}^{ji} (probability that the node j is active and the node i is active);
- p_{10}^{ji} (probability that the node j is active and the node i is dry);
- p_{01}^{ji} (probability that the node j is dry and the node i is active);
- p_{00}^{ji} (probability that the node j is dry and the node i is dry); (4.8)

These joint pdfs are spatially variable (i.e., they do depend on the couple of nodes at hand, as reflected by the notation) and must obey to the following additional constraints: $p_{11}^{ji} + p_{10}^{ji} = p_j$, $p_{01}^{ji} + p_{11}^{ji} = p_i$ and $p_{11}^{ji} + p_{10}^{ji} + p_{01}^{ji} + p_{00}^{ji} = 1$ (joint and marginal pdfs must be consistent, and the total probability has to be conserved). A few important remarks are, in order: i) this is a probabilistic model, and mechanistic cause-effect relationships affecting the sequential activation of different nodes are not necessarily represented in an explicit manner; ii) the pairs of connected nodes are not necessarily close-by in the physical space (the probabilistic space and the geometric space are different); iii) assuming a direction in the connections between any pair of nodes is necessary for the calculation of pairwise conditional pdfs and, thus, for the calculation of the joint pdf of the node states according to the Bayesian paradigm. The directionality of the links allows the identification of a parent and a child node for each pair of connected nodes, such as the connection is directed from the parent to the child. However, these directions might be arbitrary (i.e. they can be reversed provided that only pairwise conditional pdfs are generated) and don't necessarily reflect causality (see point i) above). Under the above assumptions, the correlation between two directly connected nodes X_i and X_j, ρ_{ij} reads:

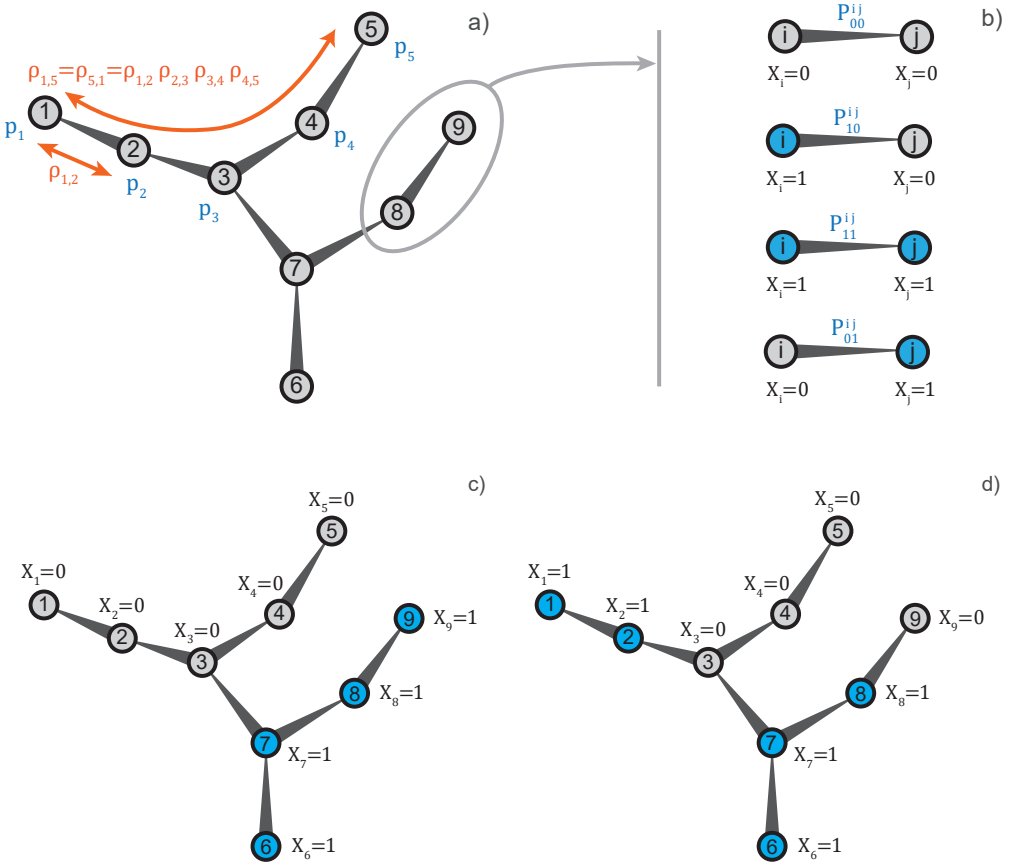

Figure 4.1: a) Schematic of a Bayesian binary network with two possible states (active or dry). Each node, represented by a circle, is identified by a number. Nodes are linked together by directed edges to represent the dependence structure of the network. Blue labels represent marginal probabilities of node activation, orange labels indicate the correlation between two nodes. b) Schematic of the joint probability of activation of two connected nodes i and j, as indicated by the blue labels. Active nodes ($X = 1$) are color-coded as blue, while dry nodes ($X = 0$) are represented in grey. c) and d) Two example configurations of possible states of the nodes. The active nodes may or may not be continuous along the network.

$$\rho_{i,j} = \frac{p_{11}^{ji} - p_i\, p_j}{\sqrt{p_i\, p_j (1-p_i)(1-p_j)}} \tag{4.9}$$

The correlation ρ given above quantifies the probability that two neighbouring nodes are simultaneously active or simultaneously dry. Nevertheless, the correlation can be calculated for both neighbouring and non-neighbouring nodes. The correlation between two nodes k and m that are not directly connected can also be expressed as:

$$\rho_{k,m} = \prod_{i:k->m} \rho_{i,i+1}\,. \tag{4.10}$$

where the product involves all the couples of directly connected nodes $(i, i+1)$ that generate a path connecting the nodes k and m (see Figure 4.1). Therefore, the full correlation structure of the network is identified by the pairwise correlations of the states of neighbouring nodes (hereafter, local correlations). Overall, a dichotomic Bayesian network is thus defined through the specification of five attributes: i) the number of nodes N, ii) the stream length associated to each node (i.e. the vector $\boldsymbol{\Delta l}$), iii) the network structure, i.e. how each node is connected with the other nodes, iv) the N local persistencies p_i and v) the $N-1$ local spatial correlations between neighbouring nodes, $\rho_{i,j}$. The mean degree of correlation of the network, $\langle \rho_{ntwk} \rangle$, can be then calculated as:

$$\langle \rho_{ntwk} \rangle = \frac{1}{N^2} \sum_{k=1}^{N} \sum_{m=1}^{N} \rho_{k,m} \tag{4.11}$$

Equation (4.11) expresses the overall correlation of the system as the average correlation existing among all the possible couples of (directly or indirectly) connected nodes of the network. $\langle \rho_{ntwk} \rangle$ is a lumped measure of the degree of spatial correlation of the random states $\boldsymbol{X}$ within a temporary stream.

A key element of the formulation is that the correlation between two nodes is constrained by the local persistency of the two nodes. In fact, for a given couple of nodes i, j with local persistencies p_i and $p_j \leq p_i$, the maximum possible correlation between the nodes, ρ_{ij}^{max}, is:

$$\rho_{i,j}^{max} = \sqrt{\frac{p_j(1-p_i)}{p_i(1-p_j)}} \leq 1 \tag{4.12}$$

while the corresponding minimum possible correlation, ρ_{ij}^{min}, reads:

$$\rho_{i,j}^{min} = -\left(\frac{p_i p_j}{(1-p_i)(1-p_j)} \right)^{\beta} \geq -1 \tag{4.13}$$

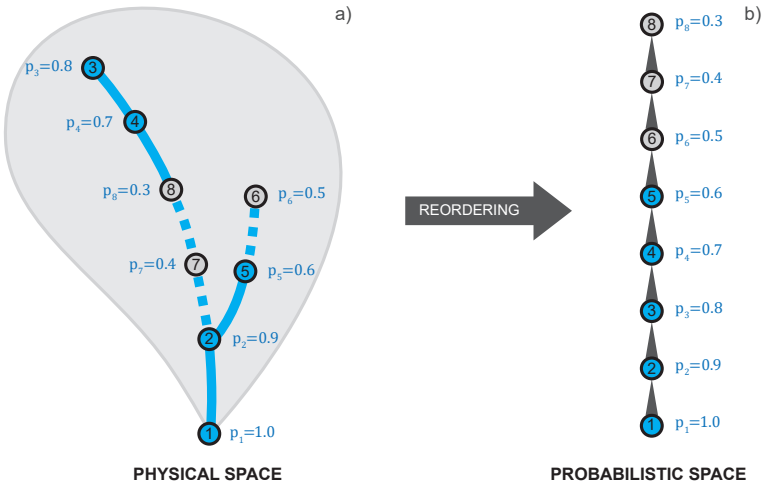

Figure 4.2: Schematic of the hierarchical model applied to an example river network with 8 nodes. a) A representative stream network drawn as a blue line that can be either active (continuous) or dry (dotted line). The nodes are active (blue) or dry (grey) accordingly. b) Schematic of the corresponding chain obtained by applying the hierarchical model. The nodes are first reordered from the most to the least persistent, and then direct connections between nodes are set. If the condition $p_{01}^{(i-1)\,i} = 0$ is set for all the neighbouring nodes, then node activation follows the chain order (i.e. the node 1 is the first to be activated, while the node 8 is active only when all the other nodes are already switched on). Note that the reordering of the nodes allows the hierarchical model to describe also active stream networks that are discontinuous in the physical space.

where $\beta = 1/2$ if $p_i + p_j \leq 1$ and $\beta = -1/2$ otherwise. Therefore, the full set of possible correlations (i.e., the range $(-1, 1)$) is available only when $p_i = p_j = 0.5$. Otherwise, the maximum local correlation is upwardly bounded or the minimum correlation is downwardly bounded. For example, two nodes with persistency 0.5 can display a correlation between -1 and 1, two nodes with persistency 0.9 have a correlation between -0.11 and 1, whereas for two nodes with persistencies $(0.1, 0.9)$ the correlation ranges between -1 and 0.11. It is worth mentioning that a unit linear Pearson correlation is possible only in the case of $p_i = p_j$, for which two connected nodes can be systematically active at the very same time. As one of the two local persistencies of the connected nodes (or both) tends to 0 or 1, the upper limit of the local correlation approaches 0.

4.3 A persistency-driven hierarchical model of network dynamics

This section introduces a simplified case of the model presented in section 4.2, in which the switching on of the various network's nodes during the expansion of the flowing streams takes place in a hierarchical way - from the most persistent to the least persistent nodes. Mathematically, this implies that the nodes are first re-ordered in a chain based on their local persistency, from the most to the least persistent (Figure 4.2). Then pairwise connections are set between consecutive nodes (i.e. between the nodes $i-1$ and i) imposing the constraint $p_{01}^{(i-1)\,i} = 0$ (in which

the first subscript refers to the status of the most persistent node of the pair, and the second subscript refers to the state of the least persistent) for all the possible pairs of directly connected nodes. This does not imply that the underlying active stream network is spatially continuous, as the re-ordering does not reflect the actual position of the nodes (two connected nodes can be far apart in the physical space, as in the example of Figure 4.2). Under these assumptions, the three non-null joint pdfs defined in equation (4.8) can be written as:

$$\begin{aligned} p_{11}^{(i-1)\,i} &= p_i - p_{01}^{(i-1)\,i} = p_i \\ p_{10}^{(i-1)\,i} &= p_{i-1} - p_{11}^{(i-1)\,i} = p_{i-1} - p_i \\ p_{00}^{(i-1)\,i} &= (1 - p_{i-1}) - p_{01}^{(i-1)\,i} = 1 - p_{i-1}\ , \end{aligned} \tag{4.14}$$

where the nodes i and $i-1$ are two consecutive nodes in the chain, re-ordered by descending persistency (i.e., $p_i < p_{i-1}$).

This process represents a single chain, in which all the nodes with the same local persistency (i.e. same p_i) behave systematically in the same manner (they are all simultaneously switched-on or switched off). Moreover, a node with a given p_i can be switched on only if all the network's nodes with a larger local persistency are already switched on. In this case, a mechanistic relationship between pairs of nodes is introduced as the switching on of the $i-1$ node is a necessary (but not sufficient) condition for the activation of the node i. The physical interpretation of this model is based on the idea that, during the network expansion, a hydrological signal is propagated along the network when a given landscape portion becomes saturated and, consequently, overland flow is generated.

Provided that the nodes are re-ordered according to a decreasing value of local persistency, each of the possible sequences of ordered nodes corresponds to a sequence of K ($K \in [0, 1, 2, ..., N]$) active nodes ($X_1 = 1, X_2 = 1, ..., X_k = 1$), followed by a sequence of $N - K$ dry nodes ($X_{K+1} = 0, X_{K+2} = 0, ..., X_N = 0$). Accordingly, in equation (4.4), the only non-zero terms of the joint pdf of $\boldsymbol{X}$ are those of the type $p_{1000...00}$, $p_{1100...00}$, $p_{1110...00}$, ..., $p_{1111...10}$, $p_{1111...11}$ and a single transition from 1 to 0 is allowed in the chain. As the position of each node in the physical space is not explicitly specified in the stochastic model, a sequence of wet and dry nodes of this type is consistent with a stream network in which the active reaches, during wetting, expand either upstream or downstream (Durighetto et al. 2020). Furthermore, the hierarchical scheme is also suited to describe active networks that are not continuous in the physical space because of non-monotonic changes of the local persistency along the network (see Figure 4.2. Under the above assumptions, equation (4.4) can be simplified as follows:

$$p(\boldsymbol{x}) = p_{000...0}^{[\prod_{j=1}^{N}(1-x_j)]}\, p_{100...0}^{[x_1 \prod_{j=2}^{N}(1-x_j)]}\, p_{110...0}^{[x_1 x_2 \prod_{j=3}^{N}(1-x_j)]} \ldots p_{111...1}^{[\prod_{j=1}^{N} x_j]} \tag{4.15}$$

The transition between 1 and 0 in the chain is observed between the nodes $i-1$, i with a probability equal to $p_{10} = p_{i-1} - p_i$. Accordingly, the probability of a sequence

of N consecutive active nodes is the probability that the least persistent node of the network is active, p_N. Likewise, the probability of a sequence of N consecutive dry nodes is the probability that the first node of the chain is dry, $1 - p_1$. Therefore, the joint pdfs of all the possible combinations of states appearing in equation (4.15) can be expressed as:

$$\begin{aligned} p_{000...00} &= 1 - p_1 \\ p_{100...00} &= p_1 - p_2 \\ p_{110...00} &= p_2 - p_3 \\ &\dots \\ p_{111...10} &= p_{N-1} - p_N \\ p_{111...11} &= p_N \end{aligned} \tag{4.16}$$

Provided that the geometry of the stream network is described by the active lengths associated to each node, the active stream length in this case only depends on the number of nodes active at a given time. Let us define L_i as the partial sum of the first i components of the vector $\boldsymbol{\Delta l}$, i.e.

$$L_i = \sum_{k=1}^{i} \Delta l_k \,, (i \geq 1) \tag{4.17}$$

whereas $L_0 = 0$ by convention. L_i $(i = [0, 1, 2, ..., N])$ identifies the length of the stream network when i nodes are active - only the nodes with persistency larger than (or equal to) p_i. This instance is observed with probability $p_{i-1} - p_i$ for $0 < i < N$ (see equation (4.16)) . Therefore, a general expression for the probability density function (pdf) of the stream length can be written as:

$$p_L(L) = \sum_{i=0}^{N} (p_i - p_{i+1}) \delta(L - L_i) \,, \tag{4.18}$$

where $\delta(\cdot)$ is the Dirac-delta generalized function (ref), $p_0 = 1$ and $p_{N+1} = 0$ to simplify the notation. The cumulative density function (cdf) of the stream length can then be calculated by means of equation (4.7), or simply integrating the stream length pdf shown in equation (4.18) as:

$$P_L(L) = \int_0^L \sum_{i=0}^{i=N} (p_i - p_{i+1}) \delta(x - L_i) dx = \sum_{i=0}^{i=N} (p_i - p_{i+1}) H[L - L_i] \tag{4.19}$$

where $H(\cdot)$ is the unit Heavyside step-function. Equation (4.19) is a linear stepwise function of L and it can be rewritten as:

$$P_L(L_i) = 1 - p_i \,. \tag{4.20}$$

The r.h.s. of equation (4.20) expresses the cumulative probability of the local persistency along the network.

4.3.1 Accuracy of the hierarchical model

The hierarchical model assumes that the activation of the nodes follows a descending persistency order. Such hypothesis was validated using empirical data with the procedure reported in this section. The hierarchical activation scheme implies that, at any given time, there exists a persistency threshold P^* that allows a separation between the dry nodes ($P < P^*$) and the wet nodes ($P \geq P^*$). Accordingly, hierarchical active networks were constructed assuming that, at any given time t, each node was active if and only if its local persistency was bigger than a suitable, time-dependent threshold $P^*(t)$. For each field survey, P^* was calculated as the exceedance probability of the corresponding observed number of active nodes. To compare observed and hierarchical active networks at a given time, a confusion matrix was computed for each node of each study catchment. The modeled and observed states of each node within all the field surveys were then compared. The spatially and temporally averaged accuracy of the hierarchical model was then calculated as

$$Accuracy = \frac{TP + TN}{TP + TN + FP + FN} \tag{4.21}$$

where TP, TN, FP and FN indicate, respectively, the true positives (i.e. the number of nodes and times for which the status of a node is correctly modeled as active), the true negatives, the false positives and the false negatives. An accuracy of 100% means that the hierarchical model was able to correctly model the status of all the nodes in the network during all the field surveys. The local accuracy is defined analogously, the only difference being that it refers to a single node, instead of the whole network. The accuracy can be thus integrated in time, i.e. across all the surveys.

4.4 Linking active length statistics to local persistency

The hypothesized hierarchical behaviour of river networks enables the derivation of novel theoretical results that advance our ability to predict the dynamics of flowing channels in temporary streams. In hierarchical networks, in fact, active channel length statistics can be expressed analytically in terms of the mean network persistency, unveiling the complex linkage between climate and stream dynamics, as reported in this section. In particular, a set of equations linking the mean and variance of the active length to the mean network persistency and its internal heterogeneity is derived in section 4.4.1. Then, in section 4.4.2 the results are reported in terms of active drainage density (defined as the active length normalized with the

corresponding catchment area), to allow the comparison of catchments with different sizes, and a further simplification is introduced showing how the mean network persistency is the only factor affecting the statistics of the active length.

Finally, an empirical linear regression between mean network persistency and mean monthly excessive precipitation (i.e. total precipitation minus potential evapotranspiration) is used to show that water availability, which is a byproduct of climate, regulates the extent of the variability of a dynamic river network.

4.4.1 Mean and variance of the active length

If, without loss of generality, $\Delta l_i = \Delta\, l$ is assumed to be a constant (i.e., equally spaced nodes), the mean active length can be calculated as:

$$\langle L \rangle = E[L] = N\ \Delta l\ E[X] = L_{max}\ \bar{P}\,, \tag{4.22}$$

where $E[-]$ denotes expectation, $\bar{P}$ is the mean network persistency (i.e. the average node persistency throughout the entire network; $\bar{P} = \sum_{i=1}^{N} P_i/N$ in case of equally spaced nodes) and $L_{max} = N\Delta l$ is the geomorphic length (i.e. the maximum length of the network).

The variance of the active length, $Var(L)$, is linked to the covariances $Cov(X_i, X_j)$ between the status of all the pairs of nodes that make up the network. In the general case, the covariance of the states of two nodes can be written as:

$$\begin{aligned} Cov(X_i, X_j) = {} & (1-P_i)(1-P_j)P_{11}^{ij} + (1-P_i)(0-P_j)P_{10}^{ij} + \\ & (0-P_i)(1-P_j)P_{01}^{ij} + (0-P_i)(0-P_j)P_{00}^{ij} \\ = {} & P_{11}^{ij} - P_i P_j \end{aligned} \tag{4.23}$$

Due to the symmetry of the covariance ($Cov(X_i, X_j) = Cov(X_j, X_i)$), there is no loss of generality in assuming $P_i \geq P_j$. Introducing the hypothesis of hierarchical activation of the nodes is equivalent to imposing $P_{01}^{ij} = 0$ (i.e. the less persistent node j cannot be active if the more persistent node i is dry), or $P_{11}^{ij} = P_j$. As a consequence, the covariance between the states of two nodes reads:

$$Cov(X_i, X_j) = P_j(1-P_i)\,. \tag{4.24}$$

This expression is only dependent on the persistencies of the two nodes. Let us now consider a stream network with N nodes numbered in a decreasing order of persistency (i.e. $P_i \geq P_j$ for $i < j$). Note that node numbering does not necessarily reflect the actual position of the nodes in the physical space. The states of the nodes can be represented in a vector of random variables $\boldsymbol{X} = (X_1, X_2, ..., X_N)$. The covariance between each possible couple of nodes can then be summarized in the covariance matrix, the elements of which can be expressed as:

$$Cov(\boldsymbol{X}) = \begin{cases} P_i(1-P_i) & \text{for } j = i \\ P_i(1-P_j) & \text{for } j < i \\ P_j(1-P_i) & \text{for } i > j \end{cases} \tag{4.25}$$

where i and j represent the row and column indexes, respectively. At any given time, the active stream length L is a linear combination of the states of all the nodes, as per equation (4.3). The stream length variance is therefore expressed as the sum of all the elements of the covariance matrix, properly weighted by the Δl_i associated to each node, as expressed by equation (4.6). Without loss of generality, to simplify the notation a constant unit length $\Delta l_i = \Delta l = 1$ is assumed for each node. All the relevant equations, however, can be easily generalized to the case $\Delta l_i \neq const$ by properly weighting each term associated to the node i (i.e. the status X_i or the local persistency P_i) with the corresponding Δl_i. First, let us express each local persistency as the sum of the mean network persitency, $\bar{P}$, and a local deviation from the mean, ΔP_i (i.e. $P_i = \bar{P} + \Delta P_i$). Note that $\sum_{i=1}^{N} \Delta P_i = 0$ by definition. Combining equations (4.25) and (4.6), and using the above definitions, the stream length variance can then be written as:

$$\begin{aligned} Var(L) &= \left[\sum_{i=1}^{N} P_i(1-P_i)\right] + \left[2\sum_{i=2}^{N}\sum_{j=1}^{i-1} P_i(1-P_j)\right] \\ &= N^2\bar{P}(1-\bar{P}) - \sum_{i=1}^{N}\Delta P_i^2 - 2\sum_{i=2}^{N}\sum_{j=1}^{i-1}\Delta P_i \Delta P_j + 2\sum_{i=1}^{N} i\Delta P_i \\ &\approx N^2\bar{P}(1-\bar{P}) + N^2\widetilde{\Delta P} \end{aligned} \tag{4.26}$$

where the term $\widetilde{\Delta P} = 2/N^2 \cdot \sum_{i=1}^{N} i\Delta P_i$ represents a weighted spatial average of the persistency deviations around the mean. The weights associated to each ΔP_i increase as i increases (i.e., as P_i decreases). Therefore, a bigger weight is attributed to the negative values of ΔP_i, and $\widetilde{\Delta P} \leq 0$. It is important to note that the last row of equation (4.26) represents an approximation of the actual value of $Var(L)$, which is obtained from the full expression of $Var(L)$ by neglecting the following two terms: i) the term $\sum_{i=1}^{N} \Delta P_i^2$, that proves to be negligible when N is large (because it is of order N, while the other terms are of order N^2); ii) the term $2\sum_{i=2}^{N}\sum_{j=1}^{i-1}\Delta P_i \Delta P_j$, that is negligible because of the compensating effects originated by the interplay between the factors ΔP_i and ΔP_j when the summation indices vary. A detailed set of numerical simulations based on synthetic networks and available empirical data confirmed that the neglected terms are at least four orders of magnitude smaller than all the other terms of the equation.

4.4.2 Statistics of the active drainage density

In this framework, the average drainage density ($\bar{D}$, defined as the average active stream length normalized with the corresponding catchment area, Horton 1945) can

be directly derived from equation (4.22), and expressed as:

$$\bar{D} = \bar{P} D_g \,, \tag{4.27}$$

where D_g is the potential geomorphic drainage density, that corresponds to the simultaneous activation of all the N nodes in the channelized network, including streams that are typically dry but excluding what is out of the geomorphically obvious channel features and the hillslopes (where surface flow could be temporarily observed). Being D and L proportional, its statistics can be easily derived from the corresponding statistics of L.

When the activation of the nodes is hierarchical, the temporal coefficient of variation of the active drainage density, CV_D (that also corresponds to the temporal coefficient of variation of the active network length, CV_L) can be written combining equations (4.26) and (4.22) as:

$$CV_D = CV_L = \sqrt{\frac{\bar{P}(1-\bar{P}) + \widetilde{\Delta P}}{\bar{P}^2}} \,, \tag{4.28}$$

where the term $\widetilde{\Delta P} = 2/N^2 \cdot \sum_{i=1}^{N} i(P_i - \bar{P}) \leq 0$ represents a weighted spatial average of the persistency deviations around the mean. Thus, $\widetilde{\Delta P}$ reflects spatial variation of persistency likely induced by patterns of geologic and morphometric attributes in the channel network or landscape.

Equation (4.28) allows for the identification of two distinct contributions to the temporal changes of the drainage density: a positive contribution proportional to $\bar{P}(1-\bar{P})$, determined by the mean persistency of the whole stream network, and a negative contribution proportional to $\widetilde{\Delta P}$, that depends on the internal spatial variability of P_i. Thus, an upper limit for the coefficient of variation of the active drainage density can be identified by setting $\widetilde{\Delta P} = 0$ in equation (4.28):

$$CV_D^{max} = CV_L^{max} = \sqrt{\frac{1-\bar{P}}{\bar{P}}} \,. \tag{4.29}$$

Equation (4.29) corresponds to the theoretical coefficient of variation of a homogeneous network made up of synchronous nodes sharing the same persistency ($\bar{P}$). In realistic cases, instead, the actual value of CV_D is influenced by the spatial variations of the local persistency. Enhanced internal geological, landscape and hydrological heterogeneities entail the spatial changes of flow persistence and increase $|\widetilde{\Delta P}|$, thereby reducing the variability of the active length. To describe the influence of the spatial variability of the local persistency on CV_D, a one-parameter beta probability density function is used to represent the heterogeneity of the persistency among the different nodes in the network. In fact, empirical data suggest that the local persistency along a network can be in most cases represented by a beta distribution with the first shape parameter equal to 1:

$$pdf(P_i) = \frac{(1-P_i)^{\beta-1}}{B(1,\beta)}\,, \tag{4.30}$$

where P is the local persistency, β is the second shape parameter of the distribution and $B(1,\beta) = \frac{1}{\beta}$. Under this assumption, the term $\widetilde{\Delta P}$ in equations (4.26) and (4.28) reads:

$$\widetilde{\Delta P} = -\frac{\bar{P}(1-\bar{P})}{2-\bar{P}} \tag{4.31}$$

leading to the following equation for CV_D:

$$CV_D = CV_L = \sqrt{\frac{(1-\bar{P})^2}{\bar{P}(2-\bar{P})}}\,. \tag{4.32}$$

Differently from equation (4.29), equation (4.32) accounts for the statistical distribution of flow intermittency within the river network. The resulting expression for CV_D, however, only depends on the mean network persistency because the term $\widetilde{\Delta P}$ of equation (4.28) was in turn expressed as a function of $\bar{P}$. The existence of a general link between $\widetilde{\Delta P}$ and $\bar{P}$ should not be surprising, since in perennial (or persistently dry) rivers all the nodes necessarily exhibit very similar persistencies - thereby implying that $\widetilde{\Delta P} \simeq 0$ for very high or very low values of $\bar{P}$.

4.5 The Stream Length Duration Curve

In the previous section, the mean and variance of the active length were explored and linked to the corresponding statistics of the local persistency. Here, the cumulative density function of the active length is used to define the Stream Length Duration Curve (SLDC), to better quantify the temporal variability of the active length. It is then shown how, thanks to the hierarchical activation, the SLDC can also be estimated from the cumulative spatial distribution of local persistency.

Being a monotonic function of L, the exceedance probability of the active stream length, $P_L(L)$, can be inverted and re-interpreted as the active Stream Length Duration Curve (SLDC), in analogy with the definition of flow duration curve that is widely employed in the hydrological literature and in practical engineering to characterize the temporal variability of the flowrate at-a-station (e.g. Vogel et al. 1994; Castellarin et al. 2004; Doulatyari et al. 2015). Flow duration curves provide a useful basis to address important water resources problems such as water abstractions, environmental flows, hydro-power, irrigation (Searcy 1959; Vogel et al. 1994; Ridolfi et al. 2020). Analogously, the SLDC enables the description of active stream dynamics providing a tool to compare stream extension and variability across different climatic areas.

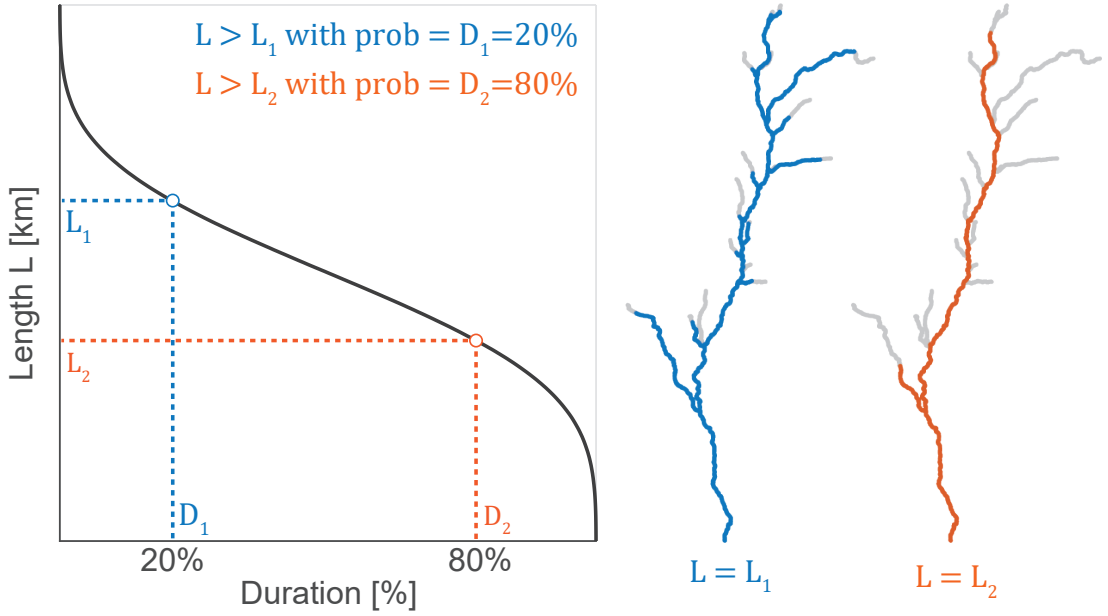

Figure 4.3: Schematic of a Stream Length Duration Curve.

This can be done graphically by putting all the possible active flow lengths (L) on the y-axis of a plot, and then representing on the x-axis the corresponding duration, $D(L)$ (Figure 4.3). The duration of a given length expresses the time for which that flowing length is equalled or exceeded, and it is calculated as the complementary of the cumulative distribution function of L as follows:

$$D\left(L\right) = 1 - P_L\left(L\right), \tag{4.33}$$

where $P_L(L)$ is the cumulative distribution function (i.e. the non exceedance probability) of the active length. This produces a function $L(D)$ that is the inverse of the exceedance probability of the active stream length given by equation (4.7). By construction, the area underlying the SLDC represents the mean length of the active streams, as given by equation (4.22), while the slope of the Stream Length Duration Curve is proportional to the variance of L expressed by equation (4.6).

Under the assumption of hierarchical activation of the nodes, the Stream Length Duration Curve can be seen as the spatial integral of the local persistency. This means that the duration of a given length (say, L^*) is the exceedance probability of the local persistency (interpreted as a spatial random variable) up to a suitable persistency threshold $p^*(L^*)$. This threshold is set in a way for which L^* is the overall network length when only the nodes with persistency larger than (or equal to) p^* are simultaneously switched on. Equation (4.20) suggests that the temporal distribution of the active stream length is linked to the spatial distribution of the local persistency. This space-for-time substitution for the estimation of the Stream Length Duration Curve is allowed only when each node of the network constraints the status of the node(s) with a smaller persistency according to the hierarchical model.

The SLDC is proposed as a general tool to quantify the natural temporal variability of the active stream network under a broad range of field settings, possibly enabling the definition of an objective classification of temporary streams, based on the underlying dynamics of the river network. In fact, the active length regime of a river can be defined based on the shape of the $D(L)$ curve, as discussed in section 5.2.4.

5 Temporal dynamics and statistics of the active length

The theoretical framework proposed in chapter 4.1 enables the description of dynamic river networks using spatially and temporally integrated statistics (e.g. average, variance and pdf of the active length). In this chapter, instead, the temporal dynamics of the active length are explored. In particular, two different but complementary approaches are employed.

In section 5.1, climatic data is used to develop a set of simple empirical models for the estimation of the active length. Even tough these models are catchment-specific and cannot be used to get a general characterization of the global patterns of temporary streams, the application of such models may provide useful insights on dynamic river networks. Specifically, the main goals of these models are a) to identify the physical drivers of active length variability, possibly enabling the identification of the hydrological processes involved in the activation/deactivation of different portions of a stream network, and b) to reconstruct the continuous dynamics of the active length starting from a limited number of field observations and widely available climatic data, such as daily precipitation and evapotranspiration.

Section 5.2, instead, takes advantage of a well-established empirical relationship linking active length to the corresponding streamflow at the outlet (Godsey et al. 2014; Jensen et al. 2017; Lapides et al. 2021; Senatore et al. 2021). The coupled dynamics of streamflow and active length are probabilistically described starting from the physically based stochastic model introduced by Botter et al. 2007. This allows the definition of the Stream Length Duration Curve as a derived distribution of the streamflow distribution. This approach can be used to provide a consistent network-scale classification of temporary streams by identifying a set of possible regimes of streamflow and active length, as discussed in section 5.2.4.

5.1 A statistical model for active length

Three different empirical models for the description of the active stream network length L were developed and their performance was formally compared to elucidate the major climatic controls on active network dynamics and the temporal scales over which the expansion/contraction cycles take place.

Rainfall depth h [mm] and potential evapotranspiration ET_0 [mm] at daily scale

are the two model inputs. The latter was evaluated from climatic data through the Penman-Monteith equation (Allen et al. 1998).

5.1.1 Model 1

The first model uses the cumulative precipitation h_T [mm] as the unique explanatory variable for L. h_T was calculated as the sum of antecedent precipitation over a time period of T days:

$$h_T(t) = \int_{t-T}^{t} h(\tau) d\tau. \tag{5.1}$$

where t is the time to which h_T is referred and τ is the integration variable. The active length was then modeled with the formula:

$$L(t) = k_0 + k_h \cdot h_T(t) \tag{5.2}$$

where the parameters k_0 [km] and k_1 [km/mm] are the intercept and slope of the recession line, respectively, which represent the length of the permanent drainage network and the length increase per unit of h_T.

Three model parameters (T, k_0, k_1) need to be calibrated in this model. For any given period T, a linear regression of the observed L against the corresponding h_T was used to calibrate the parameters k_0 and k_1 of equation (5.2), and the goodness of fit was assessed through the coefficient of determination R^2, calculated based on all the available observations. Subsequently, the optimal value of T was selected by maximizing the function $R^2(T)$. The robustness of the parameter estimation was checked via leave-one-out cross validation. This technique consists in repeating the calibration procedure for different training subsets of the available data, each of which is obtained by removing a single data point from the complete data set. The final calibrated parameters are then the average of the parameters obtained from each training subset. To characterize model performance, the standard deviations of the calibrated parameters and the mean absolute model error were calculated.

5.1.2 Model 2

The second model was obtained by replacing in equation (5.1) the cumulative rainfall depth, h_T, with the cumulative of excess rainfall, EP_T [mm], i.e. the cumulative difference between daily precipitation and evapotranspiration over a period of T days.

The reference crop evapotranspiration ET_0 was estimated with the Penman-Monteith equation (Allen et al. 1996; Settin et al. 2007). Then, a dimensionless crop coefficient k_c was used to estimate the actual evapotranspiration ET as:

$$ET(t) = k_c \cdot ET_0(t). \tag{5.3}$$

In general, k_c depends on crop type and development stage, and therefore it should be variable both in space (as a function of land cover) and in time (as a function of the vegetative state). The two main land covers of the Valfredda catchment are grazing pastures and conifer trees, for which the suggested values for k_c are between 0.85 and 1 throughout the study period (Allen et al. 1998). Therefore, in this work a uniform and constant k_c was calibrated in order to link spatially- and temporally-averaged vegetation conditions to the event-based dynamics of the overall stream length. Also, in this region, soil water content is typically higher than the incipient stress point. Accordingly, equation (5.3) does not include the effect of water stress on ET. Nevertheless, the calibrated value of k_c should implicitly include the possible effect of reduced soil-water availability on catchment-scale evapotranspiration.

The daily excess precipitation was thus expressed as $EP(t) = h(t) - ET(t)$. The cumulative excess precipitation, EP_T [mm], was then calculated by integrating EP over the period T as:

$$EP_T(t) = \int_{t-T}^{t} EP(\tau)d\tau. \tag{5.4}$$

Note that EP and EP_T can take negative values when evapotranspiration is bigger than precipitation.

The basic equation of this model is analogous to equation (5.2):

$$L(t) = k_0 + k_1 \cdot EP_T(t). \tag{5.5}$$

This model involves four parameters: the crop coefficient k_c (equation 5.3), the reference aggregation time T (equation 5.4), the length of the permanent drainage network k_0, and the L increase per unit of EP_T, k_1 (equation 5.5).

The calibration was performed following the same procedure used for model 1: for any given combination (T, k_c), the parameters k_0 and k_1 were estimated via linear regression of the observed Ls against the corresponding values of EP_T; the goodness of fit was evaluated through the determination coefficient R^2. The estimation of the optimal values of T and k_c was then performed maximizing the function $R^2(T, k_c)$. The calibration over the full set of available data was then cross validated with a leave-one-out technique.

Including ET in the calculation of the predictor for L should improve the representation of the shrinking of the Active Drainage Network during recessions. This model, in fact, is expected to originate a decrease of L over time right after each rainfall event because of the negative values of EP during non-raining days. During wet periods, instead, ET is typically smaller than the rainfall amounts, also because of lower temperatures and reduced solar radiation associated to rainy days, thereby leading to an arguably smaller impact of ET on network dynamics. Note that for $k_c = 0$ model 2 corresponds to model 1.

5.1.3 Model 3

The third model was used to assess the possible influence of different flow generation processes (surface and subsurface flow/groundwater) on the length of the drainage network. Accordingly, two cumulative rainfall depths (with two different time periods T_1 and T_2) were used to predict the active drainage network length as

$$L(t) = k_0 + k_1 \cdot h_{T_1}(t) + k_2 \cdot h_{T_2}(t). \tag{5.6}$$

The rationale of this model is the existence of multiple nested expansion/contraction cycles of the active drainage network driven by the cumulative rainfall at different time scales. These time scales possibly correspond to the time scales of the different stream flow generation processes active in the study basin.

The parameters of this model can be divided in two groups: the aggregation time scales T_1 and T_2 used to calculate the cumulative precipitations, and the three coefficients (k_0, k_1 and k_2) of equation (5.6).

The calibration procedure was analogous to the previous cases: for any given combination (T_1, T_2), the parameters of equation (5.6) were estimated via linear regression and the corresponding R^2 was evaluated; the optimal value of the couple (T_1, T_2) was then selected by maximizing the function $R^2(T_1, T_2)$, and the calibration was cross-validated with a leave-one-out technique.

The two predictors h_{T_1} and h_{T_2} used in equation (5.6) are different aggregations of the same data, and thus they could display collinearity effects. When collinearity exists, the estimate of the regression coefficients would become very sensitive to small changes in the available data, thereby reducing the statistical significance of the model. For this reason, the Belsley test (Belsley 1991) was carried out on the predictor variables to check the possible presence of collinearity between h_{T_1} and h_{T_2} for the calibrated values of T_1 and T_2.

5.1.4 Model selection

Model selection was carried out based on Akaike Weights. This method combines model performance (by minimizing the log of the residual square sum, RSS, between model estimates and experimental data) and model complexity (accounting for the number of calibrated parameters of the model). First, the Akaike Information Criterion, corrected for small sample sizes, was calculated as (Akaike 1974):

$$AIC_c = 2 \cdot \frac{g+1}{n} + log(\frac{RSS}{n}) + 2 \cdot g \cdot \frac{g+1}{n-g-1} \tag{5.7}$$

where n is the sample size and g is the number of calibrated parameters.

Akaike Weights, AW_m, were then calculated for each model m as

$$AW_m = \frac{exp(-\Delta AIC_{c,m}/2)}{\sum_m exp(-\Delta AIC_{c,m}/2)} \tag{5.8}$$

where $\Delta AIC_{c,m}$ is the difference between AIC_c for model m and the minimum value of AIC_c among all the models. The optimal model is the one characterized by the lowest value of AIC_c, that coincides to the highest value of AW. Akaike Weights are used for a formal assessment of the best model, as they formally represent the relative likelihood of each model.

5.2 Exploiting active length vs streamflow relationships

The empirical models presented in the previous section are useful for the identification of the temporal scales and major climatic controls related to active network dynamics, but are not suitable for the definition of an objective system for the classification of temporary streams based on the underlying dynamics of the network. The latter is in fact achieved in this section, in a series of steps. First, the streamflow statistics are quantified (section 5.2.1); then, a well-established empirical relation between streamflow and active length is introduced (section 5.2.2) and used to link the SLDC to the characteristics of streamflow (section 5.2.3). Finally, a joint characterization of streamflow and active length regimes is provided in section 5.2.4.

5.2.1 Modeling streamflow dynamics

River flow regimes are here quantified through the probability distribution function (pdf) of daily streamflows, using an analytical model which is based on a stochastic description of streamflow dynamics (Botter et al. 2007). These dynamics are assumed to result from the superposition of a sequence of flow pulses generated by precipitation. The model is well established in the literature and it has often been applied to estimate the pdf of daily flows based on limited information on climate and landscape (Botter et al. 2010c; Botter et al. 2013; Doulatyari et al. 2015; Basso et al. 2015).

In this model, the rainfall hydrological forcing is described by a marked Poisson process with frequency λ_p [T^{-1}] and exponentially distributed depths with average α [L]. Precipitation events are infiltrated in the root zone where they replenish the moisture deficit created by evapotranspiration in between rain events. The drainage towards the stream is assumed to take place only when soil moisture, in response to some rain events, exceeds a given wetness threshold. These fill-and-spill dynamics create a second stochastic process corresponding to the sequence of effective rainfall pulses, resulting from the filtering operated by soil moisture dynamics on the total precipitation. Consequently, the sequence of events producing streamflow (i.e. effective rainfall) can also be approximated by a Poisson process, characterized by a frequency λ [T^{-1}] ($< \lambda_p$).

If the drainable catchment storage is assumed to behave as a linear reservoir with time constant k [T^{-1}], the excess water deriving from the infiltrated rainfall, which represents the effective rainfall, is eliminated through the catchment hydrological response determining a sudden increase of the streamflow in correspondence of each event, followed by exponential recessions. Under the assumptions made, the magnitude of the jumps experienced by q are random and exponentially distributed with mean αk.

Provided that the system is linear, the overall streamflow is given by the sum of the contribution of the different effective pulses forcing the contributing catchment and the presence of overlapping pulses does not change the recession time constant, k. Hence, the stochastic dynamical equation for the specific discharge at a daily time scale reads (Botter et al. 2007):

$$\frac{dq}{dt} = -kq\,(t) + \xi_t, \tag{5.9}$$

where the temporal variations of specific discharge (per unit catchment area) $q\,(t)$ are expressed as the sum of two terms: one expresses the exponential decay of the flow in between two events; the other, ξ_t [L/T^2], describes the effect of a sequence of random streamflow increments due to effective rainfall events. Under these assumptions, the master equation associated with the stochastic process given in eq. (5.9) can be solved in steady-state conditions. The corresponding analytical expression for the pdf of q is a Gamma-distribution with shape parameter λ/k and rate parameter αk (Botter et al. 2007):

$$p_q\,(q) = \frac{(\alpha k)^{-\frac{\lambda}{k}}}{\Gamma\left(\frac{\lambda}{k}\right)}\; q^{\frac{\lambda}{k}-1} \exp\left(-\frac{q}{\alpha k}\right), \tag{5.10}$$

where $\Gamma\,(\omega)$ is the complete Gamma-function of argument ω, defined as (Abramowitz et al. 1994):

$$\Gamma(\omega) = \int_0^\infty t^{\omega-1} e^t dt. \tag{5.11}$$

The cumulative distribution function (cdf) of daily discharges can be calculated integrating the pdf of q given by eq. (5.10), as follows:

$$P_q\,(q) = \frac{\gamma\left(\frac{\lambda}{k}, \frac{q}{\alpha k}\right)}{\Gamma\left(\frac{\lambda}{k}\right)}, \tag{5.12}$$

where $\gamma(\omega, x)$ is the lower incomplete Gamma-function of argument ω with integration extreme equal to x, defined as (Abramowitz et al. 1994):

$$\gamma\,(\omega, x) = \int_0^x t^{\omega-1} e^t dt. \tag{5.13}$$

Eq. (5.12) represents the non-exceedance probability of daily discharges during a reference period, expressed as a function of α, λ and k. According to the above formulation, the mean discharge can be obtained through the following equation (Botter et al. 2007):

$$\langle q \rangle = \alpha\lambda. \tag{5.14}$$

Likewise, the coefficient of variation of daily discharges, CV_q, can be analytically expressed as (Botter et al. 2007):

$$CV_q = \sqrt{\frac{k}{\lambda}}. \tag{5.15}$$

This coefficient, which represents the ratio of the standard deviation to the mean, is a measure of dispersion of a probability distribution around the mean, and represents a quantitative metric to classify flow regimes as proposed by Botter et al. 2013. Eq. (5.10) and (5.12) are best applied to individual seasons, as they rely on the assumption of stationarity.

5.2.2 Active length vs streamflow relationship

Streamflows and active network lengths of a river co-evolve in response to the temporal variability of the the climate forcings suitably modulated by landscape features. To evaluate the dynamicity of the river network, and quantify its tendency to extend or contract in response to rainfall events accounting for geologic and topographic characteristics of the site, a well-established empirical relationship between the total active drainage length (L) and the corresponding specific discharge (q) was used. According to this formulation, the active stream length increases as a power-law function of the catchment discharge as (Godsey et al. 2014; Jensen et al. 2017; Lapides et al. 2021; Senatore et al. 2021):

$$L = \ a \ q^b. \tag{5.16}$$

In eq. (5.16) a [$d^b/cm^{b\text{-}1}$] is a constant and b is the network scaling exponent, which typically ranges between 0.02 and 1. This analytical model for the description of the joint variations in active length and discharge has been already investigated and tested in several headwater networks in humid and semiarid climates (Gregory et al. 1968; Blyth et al. 1973; Day 1978; Godsey et al. 2014; Prancevic et al. 2019). Combining theoretical analysis and empirical data, the scaling exponent b was linked to physical properties of the catchment. In particular, b was found to be influenced by the exponents of other three geomorphological scaling relationships (local slope, valley transmissivity, and drainage area). These exponents depend on key characteristics of the study site such as the drainage density, the channel slope and the topographic curvature. Higher b values identify more dynamic stream networks.

In some cases, streamflow timeseries at the outlet of the catchment within which active lengths are evaluated might not be available, but discharge measurements could be available in a different control section of the same river. In such circumstances, a permanent streamflow could be observed even in cases where the river network within the focus catchment is completely dry. If the active network length is null when the discharge is strictly positive, eq. (5.16) needs to be replaced by the following formula (Senatore et al. 2021):

$$L = \ a \ (q - q_0)^b \quad (q > q_0), \tag{5.17}$$

in which q_0 represents a threshold specific discharge, for which $L = 0$.

5.2.3 The SLDC as a derived distribution

The active length regime of a river can be defined based on the shape of the Stream Length Duration Curve (SLDC), as discussed in the following sections. To determine the SLDCs, the probability distribution function of the active lengths, $p_L(L)$, or the related cumulative distribution function, $P_L(L)$, must be estimated. To this aim, a derived distribution approach that exploits the analytical relationship between L and q was used. Inverting eq. (5.16), it is possible to express q as a function of L as follows:

$$q = \left(\frac{L}{a}\right)^{\frac{1}{b}}. \tag{5.18}$$

Then, provided that $P_L(L) = P_q(q(L))$, the cumulative distribution of the active lengths can be obtained from eq. (5.12), as:

$$P_L(L) = P_q(q(L)) = \frac{\gamma\left(\frac{\lambda}{k}\ ,\ \left(\frac{L}{a}\right)^{\frac{1}{b}}\frac{1}{\alpha k}\right)}{\Gamma\left(\frac{\lambda}{k}\right)}. \tag{5.19}$$

Eq. (5.19) can be then differentiated in order to get the analytical expression for the pdf of L, which is a generalized Gamma-distribution:

$$p_L(L) = \frac{(\alpha k)^{-\frac{\lambda}{k}}}{ab\Gamma\left(\frac{\lambda}{k}\right)}\left(\frac{L}{a}\right)^{\frac{\lambda}{kb}-1}\exp\left(-\left(\frac{L}{a}\right)^{\frac{1}{b}}\frac{1}{\alpha k}\right). \tag{5.20}$$

The mean value for the active length is represented by the following formula:

$$\langle L\rangle = \frac{a(\alpha k)^b\Gamma(\frac{\lambda}{k}+b)}{\Gamma\left(\frac{\lambda}{k}\right)}, \tag{5.21}$$

and the modal value of the distribution reads:

$$L_0 = a\,(\alpha k)^b \left(\frac{\lambda}{k} - b\right)^b. \tag{5.22}$$

Hence, the ratio between the mode of the pdf of L (eq. (5.22)) and the mean active length (eq. (5.21)) is expressed as:

$$\frac{L_0}{\langle L \rangle} = \frac{\Gamma\left(\frac{\lambda}{k}\right)\left(\frac{\lambda}{k} - b\right)^b}{\Gamma\left(\frac{\lambda}{k} + b\right)}. \tag{5.23}$$

Similarly, the coefficient of variation of the active length can be analytically derived from the Moment Generating Function of the underlying stochastic process $L(t)$ as:

$$CV_L = \sqrt{\frac{\Gamma\left(\frac{\lambda}{k}\right)\Gamma\left(\frac{\lambda}{k} + 2b\right)}{\Gamma\left(\frac{\lambda}{k} + b\right)^2} - 1}. \tag{5.24}$$

This coefficient quantifies the extent of active length variations. When $\lambda/(kb) \ll 1$, pronounced network dynamics are observed ($CV_L > 1$). When $\lambda/(kb) \gg 1$, network dynamics are smoothed ($CV_L < 1$). The dependence of CV_L on λ/k and b will be further discussed in the following section.

When the active network length is equal to 0 even if the corresponding observed discharge is null (see eq. (5.17)), eq. (5.17) reads:

$$q = \left(\frac{L}{a}\right)^{\frac{1}{b}} + q_0. \tag{5.25}$$

Therefore, the cumulative distribution function of L for this specific case can be written as:

$$P_L\,(L) = \frac{\gamma\left(\frac{\lambda}{k},\ \left(\left(\frac{L}{a}\right)^{\frac{1}{b}} + q_0\right)\frac{1}{\alpha k}\right)}{\Gamma\left(\frac{\lambda}{k}\right)}. \tag{5.26}$$

In line with the previous derivations, the probability distribution function of L when $q_0 \neq 0$ is obtained by differentiating eq. (5.26) as:

$${p_L}^C\,(L) = \frac{(\alpha k)^{-\frac{\lambda}{k}}}{ab\Gamma\left(\frac{\lambda}{k}\right)} \left(\frac{L}{a}\right)^{\frac{1-b}{b}} \left(\left(\frac{L}{a}\right)^{\frac{1}{b}} + q_0\right)^{\frac{\lambda}{k}-1} \exp\left[-\left(\left(\frac{L}{a}\right)^{\frac{1}{b}} + q_0\right)\cdot\frac{1}{\alpha k}\right]. \tag{5.27}$$

Eq. (5.27) is valid only for $L > 0$ and represents the continuous part of the pdf, p_L^C. However, in this case a finite probability is associated to $L = 0$. This corresponding

"atom" of probability in $L = 0$ must be added to the pdf so as to account for the fact that the network is completely dry when $q \leq q_0$. The atom of probability can be written as:

$$p_L{}^A(L) = P_q(q_0)\,\delta(L)\,, \tag{5.28}$$

where $P_q(q_0) = \text{Prob}[q \leq q_0]$ as given by eq. (5.12) and δ is the Dirac delta function. The overall probability distribution function of the active length, in this case, can be expressed as a sum between the continuous part of the pdf and the atom:

$$p_L(L) = p_L{}^C(L) + p_L{}^A(L)\,. \tag{5.29}$$

The Stream Length Duration Curve can be obtained by inverting the function $P_L(L)$ as given by eq. (5.19) and (5.26).

5.2.4 Streamflow and active length regimes

To identify the major drivers of discharge and active network length regimes, the analytical distributions of the catchment streamflow and active length have been normalized with the mean values of q and L. The pdf of the normalized discharge $q^* = q/\langle q \rangle$ can be written as:

$$p^*{}_q(q^*) = \frac{1}{\Gamma\left(\frac{\lambda}{k}\right)} q^{*\,\frac{\lambda}{k}-1} \exp\left(-\frac{q^*\lambda}{k}\right). \tag{5.30}$$

which is only a function of λ/k. Likewise, the pdf of the normalized active length L^* reads:

$$p^*{}_L(L^*) = \frac{1}{b}\frac{\Gamma\left(\frac{\lambda}{k}+b\right)^{\frac{\lambda}{kb}}}{\Gamma\left(\frac{\lambda}{k}\right)^{\frac{\lambda}{kb}+1}} L^{*\,\frac{\lambda}{kb}-1} \exp\left(-\left(L^*\frac{\Gamma\left(\frac{\lambda}{k}+b\right)}{\Gamma\left(\frac{\lambda}{k}\right)}\right)^{\frac{1}{b}}\right), \tag{5.31}$$

where L^* is the ratio between active length values L and the mean active length $\langle L \rangle$, obtained through eq. (5.21).

Similarly, the cdfs of normalized q and L have can be represented by the following equations:

$$P^*{}_q(q^*) = \frac{\gamma\left(\frac{\lambda}{k}, \frac{q^*\lambda}{k}\right)}{\Gamma\left(\frac{\lambda}{k}\right)}\,, \tag{5.32}$$

and:

$$P^*{}_L\left(L^*\right) = \frac{\gamma\left(\frac{\lambda}{k},\ \left(L^*\frac{\Gamma\left(\frac{\lambda}{k}+b\right)}{\Gamma\left(\frac{\lambda}{k}\right)}\right)^{\frac{1}{b}}\right)}{\Gamma\left(\frac{\lambda}{k}\right)}\,. \tag{5.33}$$

Eqs. (5.30) to (5.33) clarify that the shape of the streamflow distribution depends on the ratio λ/k while the shape of active length distribution is controlled by two dimensionless parameters: λ/k and b.

A graphical representation of the Flow Duration Curve can be helpful in order to identify the different types of river flow regimes associated to different values of the dimensionless parameter λ/k. A convex duration curve that sharply decreases towards the x-axis is obtained for $\lambda/k < 1$. This represents an erratic regime in which very low flows are frequent, but sporadic high flows are also possible (Fig. 5.1a). The erratic regime is observed when the frequency of events producing streamflow (λ) is smaller than the recession time of the catchment (k). Under these circumstances the river is able to dry considerably before the arrival of new pulses. Thus, streamflows are unpredictable (i.e. they strongly fluctuate in time) and the preferential state of

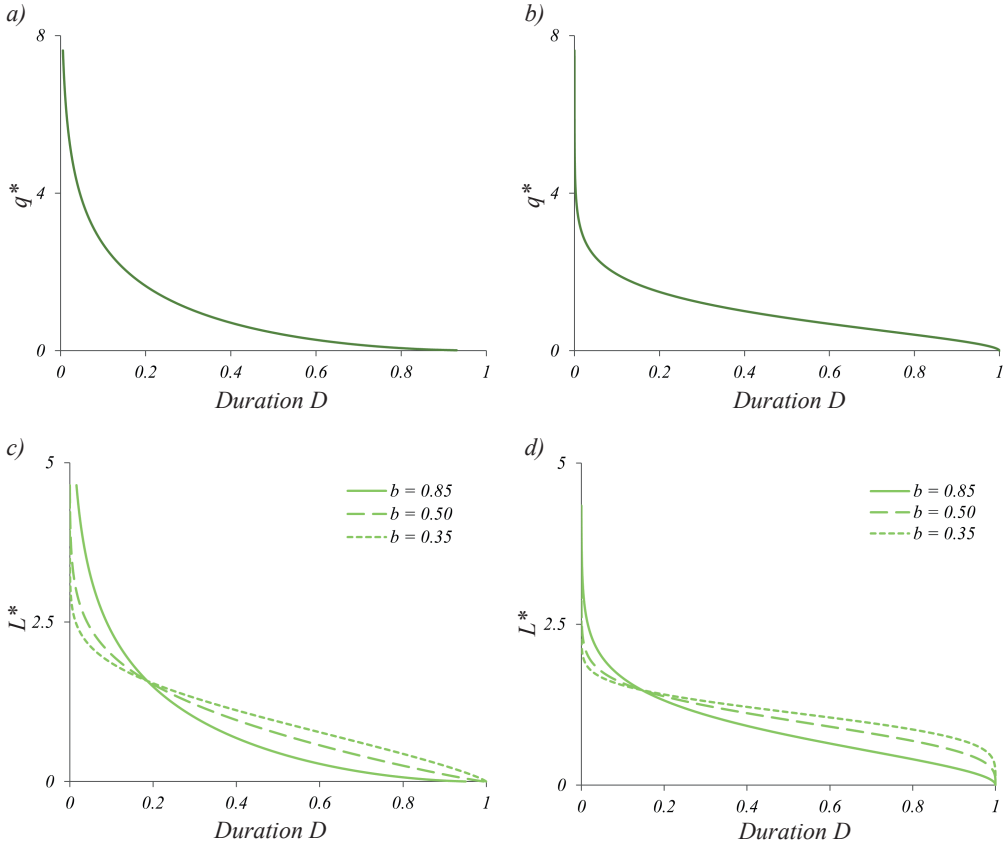

Figure 5.1: Theoretical examples of FDCs with normalized streamflow data ($q^* = q/\langle q\rangle$) and LDCs with normalized active length data ($L^* = L/\langle L\rangle$) for erratic regime (panels a and c respectively, $\lambda/k = 0.5$) and for persistent regime (panel b and d respectively, $\lambda/k = 2$). In panel c) the values of $\lambda/(kb)$ ranges from 0.59 (solid line) to 1.43 (dotted line), while in panel d) they range from 2.35 (solid line) to 5.7 (dotted line).

the system is lower than the mean. As per equation (5.15), in the erratic flow regime the coefficient of variation of daily flows is larger than one ($CV_q > 1$).

Conversely, an S-shaped FDC with an inflection point is obtained when $\lambda/k > 1$. This corresponds to a persistent regime with a limited streamflow variability and a continuous water supply to the stream from the contributing catchment (Fig. 5.1b). This corresponds to cases in which the frequency of flow-producing rainfall events (λ) is larger than the catchment recession rate (k) . Under these conditions, the hydrograph is weakly variable around the mean discharge and more predictable. Therefore, as per equation (5.15), the coefficient of variation of daily flows is smaller than one ($CV_q < 1$) and the slopes of the FDC are gentler. Flow duration curves typical of the intermediate regimes ($\lambda/b \simeq 1$) exhibit a behaviour which lies in between the two end members described above.

Differently from the flow regime, the shape of $P_L(L)$ and the corresponding active length regimes are driven by the interplay between λ/k and b. When $\lambda/(kb) < 1$, an ephemeral regime is obtained, and the river network is dry or almost dry at some point during the reference period (e.g. one season, one year) but expands significantly in correspondence of a few rain events. The corresponding SLDC is a convex function of D which decreases sharply (Figure 5.1c) and is characterized by relatively high slopes (i.e. significant temporal variations of L). Note that if $\lambda/k < 1$, the SLDC can be concave, as the pdf of q, or it could exhibit an inflection point depending on the value of the parameter b (Figure 5.1c). For $\lambda/k < 1$ and $b > 1$, both the duration curves of q and L are convex functions of D. However, for a fixed value of λ/k, if the value of the scaling exponent b decreases the SLDC becomes flatter. Thus, if $\lambda/k < 1$ and $b < 1$, the SLDC and the FDC might be characterized by different shapes. When $\lambda/(kb) > 1$, in fact, the stream length duration curve has an inflection point (Fig. 5.1d), representing a perennial regime in which the shortest values of L are characterized by a duration of 1 (i.e. at least a portion of the stream network never dries out) and the temporal variations of L are relatively limited. However, in cases where the highest value of the probability density is observed for $L \to 0$ (e.g. when $L_0/\langle L \rangle < 0.1$), the active length regime can be defined as "ephemeral de facto" provided that most of the time the network is almost dry. Under these circumstances, the SLDC closely resembles a convex function of D, in which $D \simeq 1$ only for very low values of L. Hence, when $\lambda/k > b$, the actual behaviour of the SLDC is determined by the ratio between the modal and the mean values of L, expressed by eq. (5.23). If this ratio is lower than, say, 0.1 the regime, though being perennial from a purely mathematical viewpoint, is ephemeral on practical grounds, provided that the preferential network configuration is much shorter than the mean network length. Numerical and analytical arguments suggest that, when b is lower than 1.0, the chance to observed an "ephemeral de facto" regime is quite limited. Thus, for $b < 1$ one can retain the distinction between ephemeral and perennial regimes previously introduced (if $\lambda/k > b$ perennial; if $\lambda/k > b$ ephemeral). For higher values of b, instead, the "ephemeral de facto" regime can be observed quite frequently, and needs to be explicitly considered. For practical reasons, eq. (5.23) can be approximated by a polynomial function. Thus, the criterion for identifying when the regime is ephemeral de facto can be written as:

$$\frac{\lambda}{k} < 0.4114\, b^2 + 0.7168\, b. \tag{5.34}$$

According to equation (5.24), in the perennial regime $CV_L < 1$, whereas in both the ephemeral and ephemeral de facto regimes, $CV_L > 1$. Therefore, if $\lambda/k < b$ an ephemeral regime for the active stream length is observed with $CV_L > 1$, while in cases where $\lambda/k > b$ and eq. (5.34) is satisfied, the river shows an "ephemeral de facto" active length regime with $CV_L > 1$. Otherwise, if $\lambda/k > b$ and the condition expressed by eq. (5.34) is not fulfilled, the river displays a perennial active length regime with $CV_L < 1$.

The analytical expressions derived above clarify how two dimensionless parameters, λ/k and b, determines different combinations of active length and discharge regimes in temporary rivers. The dependence of these regimes on the driving parameters, can be graphically represented in a b vs λ/k plot (Fig. 5.2).

As per the streamflow regimes, the plane can be subdivided into two regions: i) when $\lambda/k > 1$, a persistent flow regime with an S-shaped FDC is observed; ii) when $\lambda/k < 1$, instead, the flow regime is erratic, with a convex FDC. As per the active length regime, instead, three different domains can be identified in the λ/k vs. b plane. When $\lambda/k < b$ the SLDC is steep and approaches the x-axis for durations lower than 1, representing an ephemeral active length regime with relatively high probabilities associated with a river network that completely dries out. Conversely, if $\lambda/k > 0.4114\, b^2 + 0.7168\, b$, the SLDC results in a flat curve that covers the full range of durations. The S-shaped SLDC indicates a perennial active length regime with a river network that never dries out. If $b \leq \lambda/k \leq 0.4114\, b^2 + 0.7168\, b$, the catchment experiences an ephemeral de facto active length regime, with a SLDC that intersects the x axis for $D \simeq 1$. In addition, if the value of b is lower (larger) than 1, the SLDC intersects the corresponding FDC due to its flatter (steeper) shape. Instead, if b is close to 1 the SLDC results similar to the corresponding FDC. Combining these conditions, 7 macro-regions or "classes" can be identified, which are characterized by different combinations of streamflow and active length regimes, as shown in Figure 5.2 and detailed in the following.

- Class A ($\lambda/k < b$ and $b < 1$): in this class the flow regime is erratic and $CV_q > 1$. The active stream length regime is ephemeral, with $CV_Q > CV_L > 1$. This corresponds to cases in which the high variability of discharges is smoothed by the L time-series. Nevertheless, the variability in the active length is pronounced and the river network tends to dry out for a non-negligible portion of time, in correspondence of the lowest values of q.

- Class B ($\lambda/k < 1$ and $b > 1$): in this class the flow regime is erratic and $CV_q > 1$. The active stream length regime is ephemeral, with $CV_L > CV_Q > 1$. This corresponds to cases in which the high variability of discharges is further enhanced by the active length dynamics. Thus, the variability in the active length is pronounced and the river network tends to dry out for a significant amount of time during the frequent droughts.

- Class C ($\lambda/k < b$ and $b > 1$): in this class the flow regime is persistent and $CV_q < 1$. The active stream length regime is ephemeral, with $CV_L > 1$. This corresponds to cases in which the variability of discharges is limited but significant temporal changes in the the active length are observed. The pronounced variability in the active length through time is also reflected by the complete dry-down of the river network. In fact, $L = 0$ for a non-negligible portion of time, in correspondence of the lowest values of q.
- Class D ($b < \lambda/k < 0.4114\,b^2 + 0.7168\,b$ and $b > 1$): in this class the flow regime is persistent and $CV_q < 1$. The active stream length regime, instead, is ephemeral de facto, with $CV_L > 1$. This corresponds to cases in which the variability of discharges is limited but the corresponding temporal changes of the active length are comparatively more pronounced. The variability in the active length is moderate and the river network tends to dry out in correspondence of the lowest values of q. Mathematically, the most likely network configuration corresponds to a short network with a small but positive length. On practical grounds this regime is very similar to that identified as "class C".
- Class E ($\lambda/k > 0.4114\,b^2 + 0.7168\,b$ and $b > 1$): in this class the flow regime is persistent and $CV_q < 1$. The active stream length regime is perennial, with $CV_q < CV_L < 1$. Although active length variations are more pronounced than the corresponding temporal changes of q, the active length variability is not huge. In fact, the river network includes some perennial reaches that never dry out.
- Class F ($\lambda/k > 1$ and $b < 1$): in this class the flow regime is persistent and $CV_q < 1$. The active stream length regime is perennial, with $CV_L < CV_q < 1$. This corresponds to cases in which the variability of discharges is limited and so are the temporal changes in the active length. The temporal variability in the active length is very small and the river network includes a significant perennial portion that never dries out.
- Class G ($\lambda/k > b$ and $b < 1$): in this class the flow regime is erratic and $CV_q > 1$. The active stream length regime is perennial, with $CV_L < 1$. This corresponds to cases in which the pronounced variability of the discharge is not mirrored by the timeseries of L. This implies that the variability in the active length is limited. In this case the river network has a perennial portion that never dries out.

5.2.5 Model application and evaluation

The model application to a given case study requires three sequential steps: i) parameter estimation; ii) calculation of streamflow and active length statistics; iii) model evaluation.

As per the estimation of the streamflow model, the reference parameters α, λ and k were estimated on a seasonal basis starting from the available data of daily rainfall [cm] and daily specific discharge [cm/d]. k was estimated using recession data, as detailed in Basso et al. 2015. For the identification of λ, two methods were used:

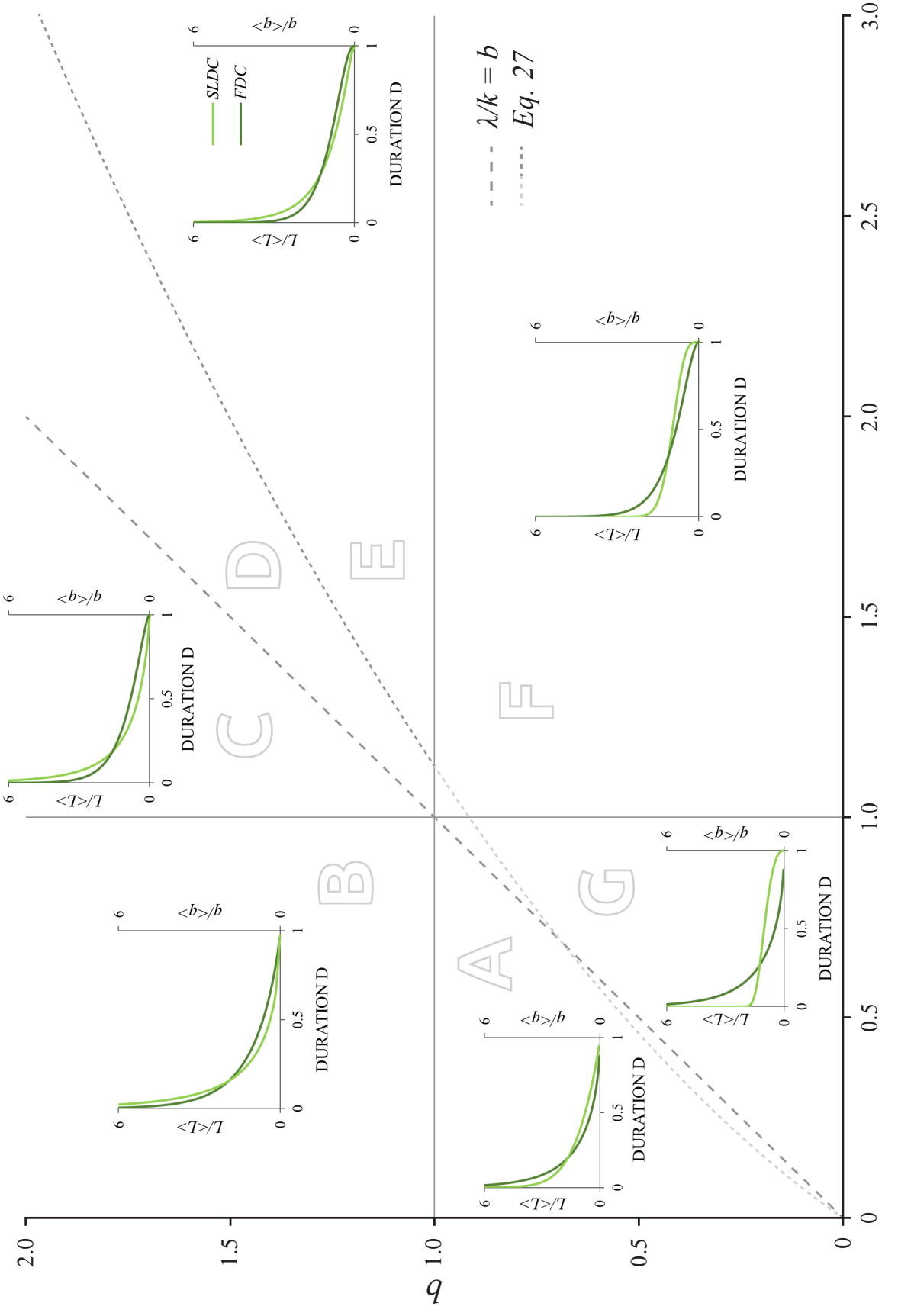

Figure 5.2: Theoretical classification of streamflow and active length regimes. The classification is based on the shape of FDCs and LDCs, which is in turn controlled by the dimensionless parameters b and λ/k. The insets refer to the dimensionless discharge ($q^* = q/\langle q \rangle$) and active length ($L^* = L/\langle L \rangle$).

a) a mass balance between rainfall and streamflow: $\lambda = \langle q \rangle / \alpha$ (eq. (5.14)); b) a computation of the frequency of positive jumps observed in the streamflow series (Ceola et al. 2010; Betterle et al. 2017). The method b) was used only in cases where several outliers in the observed streamflow data were detected (e.g. Poverty Creek during winter and spring season), which might impair the discharge sample mean.

The parameter α was calculated in two different ways: from rainfall data (method c) or using a statistical calibration (method d). Generally, the parameter α was calculated as the average of the daily precipitation depths observed during rainy days. In some cases, however, unrealistically high values of λ were obtained with this method (c) - an instance which indicates some inconsistency between rainfall and discharge data. In these cases, adjusting the streamflow data was unfeasible because of the difficulties in characterizing systematic errors in discharge measurements. Consequently, the inconsistency was resolved by calibrating α and minimizing the model errors in reproducing the relevant quantiles of the distribution (method d).

The parameters a and b of eq. (5.16) instead were obtained by a linear regression in the $\log(L)$-$\log(q)$ plane starting from available L and q data (see SI). The constant a was determined as the antilog of the intercept value, while the exponent b was calculated as the slope of the regression line. When eq. (5.17) was used, the same procedure described above was applied replacing q with (q-q_0), where q_0 corresponds to the maximum specific discharge for which $L = 0$. In all cases, the goodness of fit between the available data has been estimated in the linear regression through the R^2 coefficient.

The calculation of the underlying statistics of L and q was performed using the analytical equations detailed in the previous sections, exploiting an ad-hoc Matlab code. The pdfs and cdfs of q and L are first evaluated at the seasonal level, and then - when needed - they were aggregated at the annual timescale through a weighted average of the corresponding seasonal distributions (SI). The seasons have been defined on a calendr basis, taking into account the duration of the available timeseries.

The robustness of the analytical model for the probabilistic description of q and L developed in this paper was assessed by comparing the analytical pdfs (and cdfs) of q and L with the corresponding empirical distributions of observed discharges and active lengths. The empirical pdfs of q and L were created subdividing the range between zero and the maximum observed value of q and L into a number of equally-spaced intervals, and then computing the frequency distribution of the observations across these intervals. The empirical cdfs, instead, have been calculated using a standard Weibull plotting position, after suitable ranking of the data based on their magnitude. Finally, the performance of the models was evaluated for each case study and each subperiod of analysis using the Mean Absolute Error (MAE) among the 0.2, 0.4, 0.6 and 0.8 quantiles of the cdfs. The mean difference among the analytical and the observed cdfs of q and L in correspondence of the above quantiles were calculated using the analytical expressions for $P_q(q)$ (eq. (5.12)) and $P_L(L)$ (eq. (5.19) or (5.26)). The MAE was scaled to the mean value of the corresponding distribution (i.e. Scaled Mean Absolute Error, $SMAE$).

6 Spatio-temporal dynamics of the active network

In this chapter, the temporal dynamics of the active length described in chapter 5 are combined with the hierarchical activation scheme of section 4.3 in order to model the full spatio-temporal dynamics of the active stream network.

In particular, section 6.1 describes a simple yet effective way to reconstruct the complete dynamics of a temporary stream on the basis of a limited number of field observations, by taking advantage of the empirical models for active length dynamics introduced in section 5.1 and the concept of hierarchical structuring of channel networks.

Section 6.2, instead, describes the modeling of stream network dynamics based on the stochastic generation of timeseries of streamflow at the outlet. The model is used to explore spatiotemporal dynamics of the active network in streams subjected to contrasting flow regimes and various spatial patterns of flow persistency (section 6.2.3). The generated active network time-series are then used as a basis for a dynamic stochastic patch occupancy model (section 6.3), in which the structure of the ecological network changes through time in response to unsteady climatic conditions, to provide key information on the ecological significance of stream expansion and retraction, unveiling how river network dynamics are mirrored by key topological metrics and metapopulation occupancy under different settings.

6.1 An empirical model for reconstructing spatio-temporal dynamics of surface flow emergence

The model presented in this section combines the statistical approach proposed in section 5.1 to predict the temporal dynamics of the flowing length and the hierarchical model developed in section 4.3 to explain the spatial patterns of flow persistency. The empirical nature of this approach and the reduced number of parameters make it particularly suited to handle highly heterogeneous networks where spatially discontinuous flow patterns are observed.

The hierarchical activation scheme can be represented as a Markov chain in which the node i can be active only if all the previous nodes in the chain (i.e. nodes with

larger local persistency) are active too (see section 4.3). As a consequence, each possible network configuration corresponds to a sequence of K active nodes ($K \in [1, N]$) followed by a sequence of $N - K$ dry nodes, and a biunivocal relation between the active length and its spatial configuration along the network is generated. With this mechanism in place, spatial maps of active network can be computed at any given time following three sequential steps: i) the spatial pattern of local persistency P_i is estimated from field observations as the fraction of times surface flow was observed at each location; ii) the active network length L is computed from antecedent precipitation using a suitably calibrated empirical model (e.g. the one reported in section 5.1) iii) at each time step of the simulation the nodes are activated following the hierarchical scheme until the desired active length is reached.

Note that steps i) and iii), which recreates the spatial pattern of the active network, rely on empirical data alone, without any additional parameter calibration. Given the usually limited number of field surveys, P_i can only take a set of discrete values; thus, the network geometry is composed by discrete stretches with uniform persistency. In order to provide a prediction of a network that is continuous both in time and space, P_i is linearly interpolated in space along the network prior to the application of the step iii) of the above procedure.

This procedure represents a simple way to reconstruct the complete spatio-temporal dynamics of a dynamic river network from precipitation data and a limited number of field surveys, allowing an optimized used of empirical data about stream dynamics. This approach is also useful to enhance the resolution of empirical data within a mathematically robust framework, in which the temporal and spatial dimensions of the problem are suitably connected through the persistency of the network nodes. An example application of the approach is shown in Chapter 7.10.

6.2 A spatially explicit Bayesian hierarchical model of channel network dynamics

This section describes the modeling of stream network dynamics based on the stochastic generation of streamflow timeseries. Although the proposed model requires a small number of parameters and a limited computational effort, it allows the synthetic simulation of the spatio-temporal dynamics of the active stream network under a broad range of climatic and morphological conditions. The model is used to explore spatiotemporal dynamics of the active network in streams subjected to contrasting flow regimes and various spatial patterns of flow persistency (section 6.2.3).

The mechanism of hierarchical activation is tantamount to assuming that at any time there exist a time-dependent persistency threshold $P^*(t)$ that separates dry nodes (the nodes in the map with persistency lower than $P^*(t)$) from wet nodes (the ones with persistency higher than $P^*(t)$). The advantage offered by this approach is the disentanglement of the temporal component of network dynamics, dictated by $P^*(t)$, from the spatial pattern shown by active network through time, which is

prescribed by the arrangement of the local persistency along the network.

Operationally, modeling the spatio-temporal dynamics of the active network with this procedure requires two main steps: the potential network is first defined via a set of connected nodes with prescribed local persistency (section 6.2.1) and then a time-variable persistency threshold $P^*(t)$ is used to discern dry nodes from wet nodes at each time step of the simulation (section 6.2.2.

6.2.1 Simulating spatial patterns of local persistency

The spatial patterns of network dynamics are governed by the spatial distribution of local persistency along the network. These data can be directly estimated from field surveys (see section 2.1); however, if empirical data about stream persistency is lacking, a first-order approximation can be made by exploiting climatic and morphological data. This procedure is divided in three consecutive steps: 1) estimation of the mean network persistency, 2) definition of the cumulative density function of local persistency, and 3) assignment of local persistency to each node.

The first step consists in defining the average local persistency along the network, $\bar{P}$, by taking advantage of its linear correlation with the catchment-scale excess precipitation. An empirical law obtained from the available data (see section 7.5) can be used to estimate $\bar{P}$ as

$$\bar{P} = 0.0527 + 0.1951(P_t - E_p) \tag{6.1}$$

where P_t and E_p are, respectively, total precipitation and potential evapotranspiration in $mm/year$.

The second step defines CDF_P, the cumulative density function of local persistency. Experimental data gathered in a set of catchments located in different geomorphoclimatic regions suggests that the statistical distribution of the local persistency P_i along the river network follows a one-parameter beta probability density function (see equation (4.30) in section 4.4.2). This is a special form of the beta distribution in which one of the two parameters is set equal to one. The corresponding cumulative density function of P_i can be written as

$$CDF_P(P_i) = 1 - (1 - P_i)^{\beta} \tag{6.2}$$

where the parameter $\beta = 1/\bar{P} - 1$ is inversely related to the average network persistency. Thus, once the mean persistency of a given network is known, or it has been estimated via equation (6.1), the parameter β in eq (6.2) can be determined.

In the third step, each node of the network is then assigned a local persistency P_i extracted from the known distribution CDF_P, given by equation (6.2). Observed spatial correlations of the local persistency in dynamical river networks are typically quite variable across different study sites. While spatial patterns of P_i were found to be positively correlated with some relevant geomorphic properties (Jensen et al.

2018), in some cases local heterogeneity in geological features dominates, making the observed heterogeneity of P_i enhanced and rather unpredictable (e.g. Senatore et al. 2020; Durighetto et al. 2020). To cope with this issue, three different scenarios are identified here. In the first, the local persistency of each node is assigned in a completely random manner, resulting in non-correlated values of P_i along the network; in the second scenario, instead, P_i is deterministically linked to the topographic wetness index (TWI), which was proposed to be a good measure of the likelihood of surface flow (Beven et al. 1979). Specifically, the scheme assumes that, for any pair of nodes i and j, if $P_j < P_i$ then $TWI_j < TWI_i$; finally, in the third scenario P_i is deterministically linked to the upslope accumulated area, which is usually considered to be proportional the amount of water supplied from upstream.

6.2.2 Stochastic generation of spatio-temporal dynamics of the active channel network

The hierarchical framework proposed in this thesis, the temporal dynamics of expansion and contraction of temporary streams are uniquely determined by the temporal variability of a persistency threshold separating wet from dry nodes, $P^*(t)$. The temporal variations of the persistency threshold $P^*(t)$ are driven by the changes in the corresponding catchment streamflow $q(t)$: when q increases (decreases), the network expands (contracts), and P^* decreases (increases). When available, timeseries of observed or modeled $q(t)$ can be directly employed for the reconstruction of the past dynamics of the active network. Alternatively, the physically-based stochastic model presented in section 5.2.1 can be employed to generate synthetic timeseries of $q(t)$ that mirror the natural intermittency of precipitation. The main advantage of using the model presented in section 5.2.1, as compared to more sophisticated hydrological models, is that it requires only 4 parameters with a clear physical meaning, and thus it enables a parsimonious and simple generation of long-term scenarios in which the stochastic nature of rainfall is explicitly accounted for.

The stochastically-generated streamflow follows the Gamma distribution reported in equation (5.12). This function can be inverted and interpreted as the Flow Duration Curve (FDC), which links each flow value q to the corresponding relative duration D, i.e. the fraction of time for which that specific q value is equalled or exceeded. In particular, the flow duration curve can be written as:

$$D(q) = FDC(q) = 1 - P_q(q) \ . \tag{6.3}$$

As one can imagine, the dynamics of the active network mimic the sequence of streamflow pulses and recessions. Due to the hierarchical scheme, network expansion always follows the same sequence of network configurations in which new nodes are activated at each expansion step and no active nodes are deactivated. The reverse sequence corresponds to network contraction. Therefore, the synchronism between increases (decreases) of q and network expansion (contraction) suggests the existence of a biunivocal correspondence between q and the configuration of the active network. This correspondence is in line with the literature about temporary

streams, which show the existence of a bijective relation between q and L (Day 1978; Godsey et al. 2014; Prancevic et al. 2019; Jensen et al. 2019; Zanetti et al. 2021). As a consequence, whenever a streamflow q with duration D is observed at the outlet, the corresponding network configuration is composed of nodes that are active for a percentage of time of at least D, because they are also active in all the more expanded configurations relative to higher flows. To state it differently, whenever a given network configuration is observed, all the active nodes have a local persistency P_i which is at least D:

$$P^*(t) = D(q(t)) = 1 - P_q\,(q)\ , \tag{6.4}$$

where $P^*(t)$ is the instantaneous value of the threshold of local persistency that allows a distinction between active and dry nodes. Therefore, for each time step the status of each node of the network is assigned as:

$$X_i(t) = \begin{cases} 1 & \text{if } P_i \geq P^*(t) \\ 0 & \text{otherwise} \end{cases} \tag{6.5}$$

The length of the active network, $L(t)$, can then be calculated as the sum of the lengths Δl_i associated to each active node:

$$L(t) = \sum_{i=0}^{N} \Delta l_i \cdot X_i(t)\ . \tag{6.6}$$

Once $L(t)$ is known, the Stream Length Duration Curve can be easily obtained with the Weibull plotting position method. However, thanks to the hierarchical activation scheme, the SLDC can also be directly achieved from the spatial distribution of the local persistency. In particular, $1 - CDF_P(P_i)$ can be interpreted as the fraction of nodes with local persistency greater than P_i, which corresponds to the fraction of length that is active for a relative duration of $D = P_i$. Therefore, the Stream Length Duration Curve can be written as

$$\frac{L}{L_g} = 1 - CDF_P(D) \tag{6.7}$$

where L_g is the geomorphic length, i.e. the total length of the stream network.

This setup allows the generation of a stochastic timeseries of streamflow following equation (5.9), and which is transformed into a timeseries of persistency thresholds with eq. (6.4). Finally, starting from the potential network generated in 6.2.1, equation (6.5) dictates which nodes are active at each time step. Therefore, the full spatial and temporal dynamics of a temporary stream are obtained.

6.2.3 Numerical setup

A number of simulations was carried out to explore different scenarios achievable by the presented model. Multiple sets of climatic parameters were tested, as reported in Table 6.1. In particular, three different triplets of rainfall parameters (λ_P, α, E_p) were used to simulate three contrasting climatic types (namely Dry D, Intermediate I and Wet W). The recession coefficient k was assumed to be representative of the alpine climatic region. The actual evapotranspiration E_a is calculated with the Budyko curve (Budyko 19774; Mianabadi et al. 2019) as

$$\frac{E_a}{P_t} = \left[\frac{E_p}{P_t} tanh\left(\frac{P_t}{E_p}\right)\left(1 - exp\left(-\frac{E_p}{P_t}\right)\right)\right]^{1/2} \tag{6.8}$$

where $P_t = \alpha\lambda_P$ is the mean total precipitation. The mean effective rainfall frequency λ is estimated with a catchment water balance, where the mean effective precipitation can be written as the difference between P_t and the actual evapotranspiration E_a

$$\lambda = \lambda_P - \frac{E_a}{\alpha} \, . \tag{6.9}$$

The mean network persistency is then estimated by means of equation (6.1). Local persistency values for each node of the network are randomly extracted from the pdf shown in eq. (6.2). In particular, three different criteria for assigning local persistencies are compared: *1*) completely random, resulting in non-correlated persistency along the network, *2*) by topographic wetness index (i.e. nodes with higher TWI are given higher persistency) and *3* by contributing area. Each of the 9 scenarios explored in this paper is determined by the combination of a criterion for persistency assignment (*1-3*) with a climatic type (D, I or W) and, accordingly, identified by the corresponding label (e.g. the scenario with wet climate and local persistencies by contributing area is labeled *W3*).

For each scenario, a timeseries of streamflow at the outlet $q(t)$ is stochastically generated, from which the flow duration curve is derived and used to generate the corresponding timeseries of persistency threshold $P^*(t)$, as explained in 6.2.2. The status of each node is assigned for each time step by means of eq. (6.5), and the active length calculated with eq. (6.6). Finally, the Weibull plotting position method is used to construct the Stream Length Duration Curve (SLDC) from $L(t)$, and compare it with equation (6.7).

Finally, the sensitivity of the active stream network on the local persistency threshold was assessed. To this aim, the length of the Minimum Spanning Tree, MST, is calculated on the active nodes of the stream network for each of the 9 scenarios. Therefore, the advantage of the MST lies in the possibility of conceiving it as the SLDC of the connected portion of the network.

Table 6.1: Summary of the parameters used in the erratic and persistent flow regime scenarios. Only λ_P, α, E_p and k are independent parameters.

Climatic scenario	**Dry (D)**	**Intermediate (I)**	**Wet (W)**	
λ_P	0.25	0.40	0.55	d^{-1}
α	15.0	12.00	10.0	mm/d
E_p	3.0	2.50	2.0	mm/d
k	0.15	0.15	0.15	d^{-1}
P_t	3.75	4.80	5.50	mm/d
E_a	2.29	2.16	1.82	mm/d
λ	0.10	0.22	0.37	d^{-1}
λ/k	0.65	1.47	2.45	d^{-1}
$\bar{P}$	0.20	0.50	0.74	-

6.3 Beyond hydrology: dynamic metapopulation model

The generated active network time-series can be used as a basis for the dynamic stochastic patch occupancy model proposed in this section, in which the structure of the ecological network changes through time in response to unsteady climatic conditions. This approach enables an assessment of the full impact of the hydrological dynamics to which river networks are exposed on species persistence. The results of the metapopulation model and the comparison between dynamic and static network scenarios may in fact provide key information on the ecological significance of stream expansion and retraction, unveiling how river network dynamics are mirrored by key topological metrics and metapopulation occupancy under different settings.

In particular, to show the potential of the analytical and numerical tools developed in this thesis, a dynamic stochastic patch occupancy model (D-SPOM) is used to simulate the presence-absence of a focal species over the aforementioned dynamic stream network. The model is a dynamic version of the widely adopted stochastic patch occupancy model, SPOM (Hanski 1994; Moilanen 1999; Rybicki et al. 2013; Giezendanner et al. 2019). The SPOM is a homogeneous first-order Markov chain in which the state of the metapopulation at time t+1 depends only on the state (occupancy pattern) of the metapopulation at time t. In particular, a binary state variable, $y_i(t)$, is set to 1 if site i is occupied at time t, and 0 otherwise. Then, for each node in the network and each time step, the probabilities of colonization and extinction events depend on colonization and extinction rates with exponential survival probability:

$$P_{C,i}(t) = 1 - exp(-C_i(t))\Delta t \tag{6.10}$$

$$P_{E,i}(t) = 1 - exp(-E_i(t))\Delta t \tag{6.11}$$

where Δt is the simulation time step and $C_i(t)$ and $E_i(t)$ are the colonization and extinction rates for the i-node at time t. The key novelty introduced in the D-SPOM is to consider $C_i(t)$ and $E_i(t)$ as dependent on the current hydrological status of the river network according to the following equations:

$$C_i(t) = c \sum_{i \neq j} exp(-d_{ij}(t)/D) P_j(t) y_j(t) \tag{6.12}$$

$$E_i(t) = e/P_i(t) \tag{6.13}$$

where P_i is the persistency of the i-node, and $d_{ij}(t)$ is the pairwise distance between the reach i and j calculated along the river network. The presence of rescue effects (Brown et al. 1977; Moilanen 2004) in the extinction rate (equation (6.11)) is neglected, because the primary objective is about how environmental stochasticity, rather than demographic stochasticity, affects species dispersal and persistence. Temporal fluctuations of colonization rate, $C_i(t)$, and extinction rate, $E_i(t)$, include three specific traits of the given focal species: colonization, c, extinction, e, and mean dispersal distance. The specific values of these parameters were chosen from literature to be $c = 0.1\ d^{-1}$, $e = 0.05\ d^{-1}$, and $D = 200$ m. It is important to note that the goal of this application is to highlight the importance of the dynamics of a river network on ecological processes rather than provide an exact description of e specific study site. For this reason, no calibration or sensitivity analysis is performed on the parameters.

In classical metapopulation theory (Hanski et al. 1991; Hanski et al. 2000), the metapopulation capacity, λ_{max}, is derived for a static landscape (i.e. $P_i(t) = S_i$) and captures the impact of landscape structure (the amount of habitat and its spatial configuration) on metapopulation persistence. Species can persist if the equilibrium state p_0 corresponding to global extinction (i.e. characterized by pi = 0 for any i) is unstable. This condition is met when the leading eigenvalue of the Jacobian matrix J of the system linearized around p_0 is positive. By defining a landscape matrix $\mathbf{M}$ consisting of elements $m_{ij} = exp(-d_{ij}/D)S_iS_j$ for $i \neq j$ and $m_{ii} = 0$, the Jacobian reads $\mathbf{J}$ = c$\mathbf{M}$- e$\mathbf{I}$, where $\mathbf{I}$ is the identity matrix. The leading eigenvalue of $\mathbf{J}$ can be expressed as $c\lambda_{max} - e$, where λ_{max} is the leading eigenvalue of matrix $\mathbf{M}$ that contains information about the landscape and the quality of the river reach. The theoretical prediction of the classical metapopulation theory is that a species can persist whenever $\lambda_{max} > e/c$ (Hanski et al. 1991; Hanski et al. 2000). However, when simulating the stochastic discrete process using D-SPOM, even a species with e/c above the λ_{max} threshold could go extinct due to demographic stochasticity (Bertassello et al. 2021).

The advantage of the proposed D-SPOM approach is to explicitly account for the spatiotemporal dynamics influencing habitat availability and accessibility for a focal species. The model requires two fundamental variables of metapopulation dynamics: habitat suitability, which is considered here as function of the local persistency (P_i), and connectivity, which is estimated based on dispersal across the inter-patch distance (d_{ij}). In this analysis both landscape attributes are temporally variable, being

driven by daily, seasonal, and annual-scale hydroclimatic forcing (see section 6.2.2). Metapopulation dynamics are estimated in terms of length occupancy, $\Omega(t)$, which identifies the temporal dynamics of the fraction of river network that is occupied by a focal species. $\Omega(t) = 1$ means that every node of the river network is occupied by the species, while $\Omega(t) = 0$ indicates that the species is extincted in the given habitat.

7 Results

7.1 Visual field surveys in the Valfredda catchment

The active length observed in the Valfredda catchment during the 32 field surveys performed from 2018 to 2021 ranges from 5.5 to 12.2 km (33 to 77 % of the maximum potential length as defined in section 2.1), depending on the underlying hydrological conditions, with an average of 9.1 km (Table 7.1). The corresponding Active Drainage Density ranges between 1.06 and 2.35 km^{-1}. The connectivity of the observed drainage network is reported in Table 7.1 in terms of disconnected length and disconnected clusters (i.e. number of contiguous parts of the active network that are disconnected from the outlet). The minimum length (Figure 7.1a) was surveyed on the 26^{th} of October, 2018, after a dry period of about 50 days (total precipitation 38 mm). The maximum extension of the active drainage network was recorded 8 days later, on the 3^{rd} of November, after a precipitation event of about 320 mm (Figure 7.1b).

The spatial distribution of the persistency index, P_i, is represented in Figure 7.1c. The lower order branches of the network generally have a lower persistency, with the exception of the tributaries that are supplied by permanent springs, marked on the Figure with pale red circles.

The permanent fraction of the drainage network covers only 28 % of the total length (Figure 7.1d), suggesting a high temporal variability of the drainage network notwithstanding the humid climate and the presence of many permanent springs in the catchment. Despite showing evident channelization signs, 21 % of the potential length was inactive during all the field surveys.

Figure 7.2 shows how the number of disconnected clusters, the number of sources, the disconnected length and the persistency index P_i vary as a function of L. As L increases, two contrasting processes can affect the number of disconnected branches of the network. On one hand, in the presence of active streams that are only temporarily disconnected from the outlet due to a dry channel downstream, an increase in L should remove the disconnections, thus reducing both the number of disconnected clusters and the disconnected L. On the other hand, in case of temporary stretches that remain always disconnected from the main river network, an increase in L during wetting produces the activation of new disconnected reaches, thereby increasing both the number of disconnected clusters and the disconnected L. The

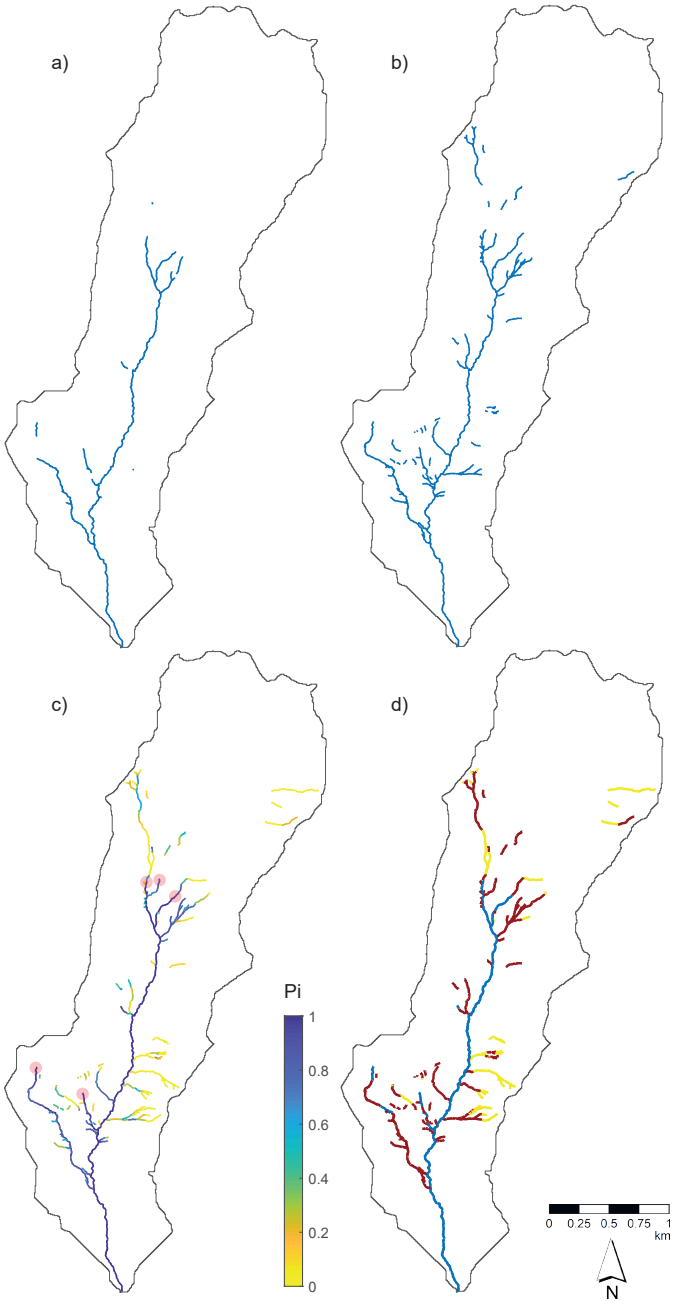

Figure 7.1: Maps of the Valfredda drainage network: (a) active drainage network at its minimum on 26/10/2018, (b) active drainage network at its maximum on 03/11/2018, (c) persistency index, from 0 (yellow) to 1 (blue) and (d) classification of network stretches as persistent (blue), temporary (red) and dry (orange). Red circles in panel (c) denote permanent springs. Panels (c) and (d) show the potential network; disconnections are present when channels stop and the water flow is dispersed on the hillslope and infiltrated.

Table 7.1: Summary of the field surveys, with the active length (L, in km and as a percentage of the 16.2 km of mapped potential drainage network), the active drainage density, the disconnected length (in km and %), and the number of disconnected clusters (i.e. the number of active stretches that are not connected at the surface to the outlet).

Date	**Active length L**		**Active drainage density**	**Disconnected length**		**Disconnected clusters**
	[km]	%	[km^{-1}]	[km]	%	[-]
12 Jul 2018	9.16	56	1.72	1.70	10.5	31
26 Jul 2018	9.25	57	1.71	1.76	10.9	33
07 Aug 2018	10.36	64	1.95	2.29	14.1	36
23 Aug 2018	10.14	62	1.91	1.83	11.3	30
04 Sep 2018	11.28	69	2.13	3.30	20.4	41
13 Sep 2018	9.36	58	1.77	1.75	10.8	33
01 Oct 2018	7.97	49	1.50	1.17	7.2	18
26 Oct 2018	6.41	39	1.21	0.63	3.9	13
03 Nov 2018	12.48	77	2.35	3.45	21.3	49
18 Jan 2019	5.46	33	1.06	0.78	4.8	14
07 Aug 2019	10.44	64	1.96	2.88	17.8	36
12 May 2020	8.72	53	1.64	1.24	7.7	25
03 Jul 2020	10.71	65	2.01	2.11	13.0	40
28 Jul 2020	9.92	61	1.86	1.41	8.7	27
05 Aug 2020	13.48	82	2.53	3.24	20.0	56
17 Sep 2020	9.89	60	1.86	1.43	8.9	29
23 Sep 2020	9.72	59	1.83	1.43	8.8	31
30 Sep 2020	9.67	59	1.82	1.41	8.7	29
08 Oct 2020	13.26	81	2.49	3.46	21.4	44
30 Oct 2020	9.97	61	1.87	1.40	8.7	29
06 Nov 2020	9.77	60	1.83	1.44	8.9	31
18 Nov 2020	9.68	59	1.82	1.42	8.8	27
25 Nov 2020	9.21	56	1.73	1.34	8.3	25
14 Jul 2021	9.20	56	1.73	1.14	7.1	27
12 Aug 2021	9.45	58	1.77	1.83	11.3	29
02 Sep 2021	8.80	54	1.65	1.21	7.5	27
10 Sep 2021	8.92	55	1.67	1.24	7.6	29
30 Sep 2021	9.20	56	1.73	1.37	8.5	25
20 Oct 2021	9.74	60	1.83	1.51	9.3	31
28 Oct 2021	8.80	54	1.65	1.24	7.6	29

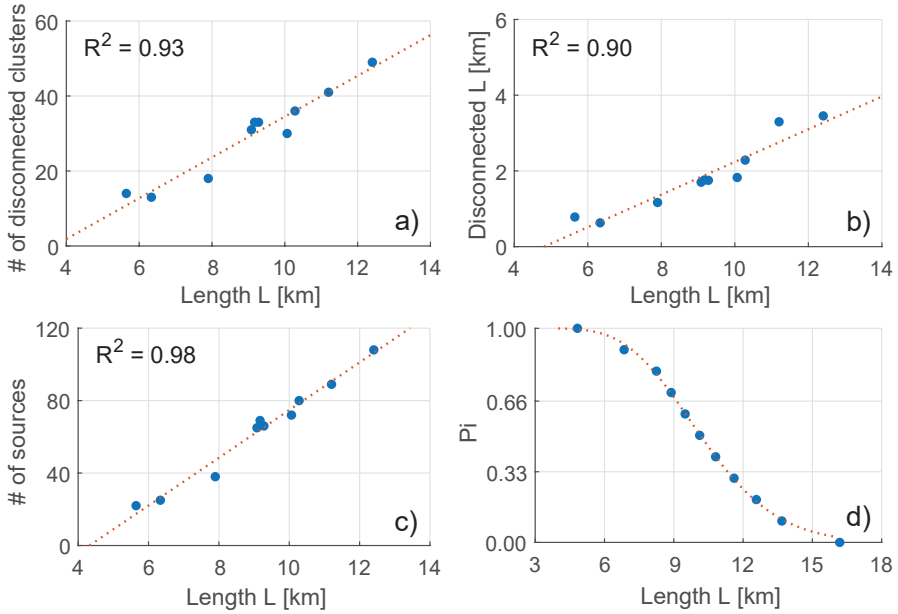

Figure 7.2: Correlation between key properties of the drainage network. Number of disconnected clusters (a), disconnected active drainage length (b) and number of sources (c) are linearly correlated with L. Persistency P_i follows a gamma distribution with $k = 15.8$ and $\theta = 0.67$ km (d). The red dotted lines represent the regression line (panels a, b, c) and the theoretical gamma distribution (panel d). The P-value of each regression is smaller than 10^{-3}.

increasing trend of disconnected clusters and disconnected length as function of L shown in Figure 7.2 therefore indicates that in the Valfredda catchment the activation of additional disconnected reaches during river network expansion dominates. Accordingly, also the number of sources increases with L because the less persistent stretches (which become active only for high values of L) mostly correspond to the lower order upstream channels, where the network is more branched (see Figure 7.1c).

Figure 7.2d shows the relationship between L and the persistency index P_i. The plot shows the length of the active drainage network obtained when only the stretches with persistency greater than (or equal to) different values of P_i are active. The observed points closely follow a gamma distribution with shape parameter $k = 15.8$ and scale parameter $\theta = 0.67km$.

Based on the geological features of the bedrock, 5 different geologic units were detected in the Valfredda catchment: U1) solid and debris limestones, moraine and debris deposits; U2) marl limestones; U3) dolomite and chalks; U4) moraine deposits and sandstone; and U5) rhyodacitic ignimbrites. The heterogeneity in the geology is also reflected in the soil cover and vegetation, (see below).

A significant spatial variability in the drainage density and network dynamics was observed across the five geologic units (Figure 7.3). In the northern part of the catchment (U1), where debris deposits and terrain depressions dominate, the drainage density is low (namely 1.9 km^{-1}, of which 1.3 km^{-1} has a persistency smaller than 0.5). This is also reflected by the presence of several pits in the DTM, some of them

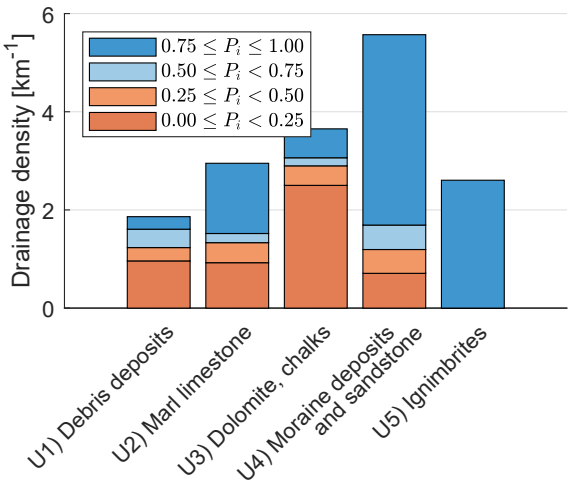

Figure 7.3: Drainage density in the five main geologic units of the catchment, classed based on the underlying persistency.

characterized by relatively high contributing areas, where water can accumulate during rainfall events to be later infiltrated and transferred to the groundwater.

In the portion of the catchment between 1800 and 2150 m a. s. l. (U2) there are five perennial sources fed by groundwater (pale-red dots in Figure 7.1), possibly originating from the northern part of the basin. These permanent streams represent the non-dynamical fraction of the network. However, they can be enriched by a multitude of temporary tributaries during wet conditions (Figure 7.1a-c). In this geologic unit, the drainage density (3 km^{-1}) is almost evenly contributed by persistent and temporary streams (Figure 7.3). These dynamic tributaries can either expand upstream from the most permanent reaches of the network or expand downstream from disconnected reaches that temporarily reconnect to the main Valfredda creek during wet conditions.

The most dynamical reaches of the network were observed in the central-eastern region of the watershed (U3), where rocky outcrops dominate. Interestingly, the tributaries that are located on the western side of the catchment (U4) were much less dynamical. This asymmetry in the temporariness of the tributaries that originates from the two hillslopes of the main valley in the central part of the catchment is explained by the heterogeneity of geology and physiography. The western side of the valley is characterized by moraine deposits overlaid by a relatively thick organic soil layer covered by grassland and conifers (Figure 3.2). This part of the catchment shows a high drainage density ($\approx$ 5.5 km^{-1}), of which only 1.2 km^{-1} has a persistence smaller than 0.5 (Figure 7.3). Instead, on the eastern side the dolomite bedrock is close to the surface and generates an almost-impermeable surface with steep slopes. The resulting network has a much lower persistency, and drainage density is much smaller than in U3 (3.6 km^{-1}). Finally, the lower part of the main valley (U5) is covered by thick forest. Here, the drainage density is reduced to 2.6 km^{-1}, and all channels are persistent.

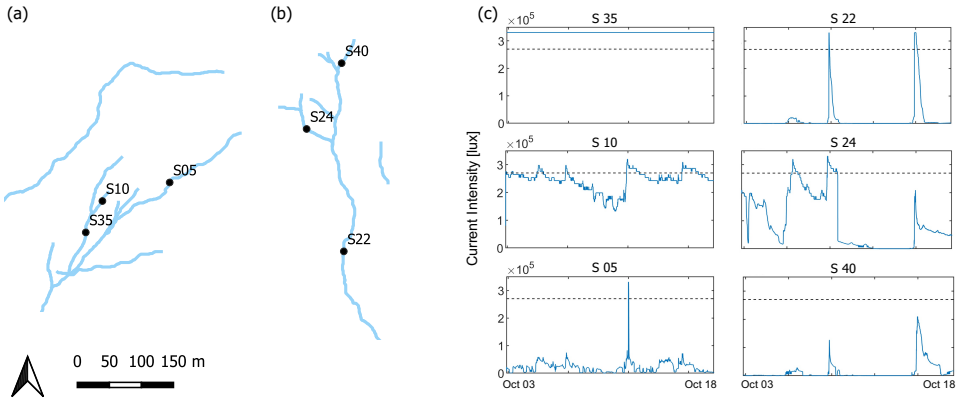

Figure 7.4: Examples of time series recorded by some of the sensors for two weeks between October 03 and October 18. The dashed line represent the threshold of 270000 *lux* (c) and location of these sensors along the tributaries of Zone 1 (a) and 2 (b).

7.2 Water presence sensors in the Valfredda catchment

The analysis of the time series of the electrical signals, $I(t)$, recorded by the water presence sensors deployed in two study zones of the Valfredda (see section 2.2) elucidates the different hydrological behaviour of the two study zones, and also emphasizes the heterogeneity of the signal recorded by different sensors within each zone. In most cases, $I(t)$ shows a pronounced temporal variability within the whole period of record.

The HOBOs belonging to Zone 1, which were all placed on a grassy substrate, exhibited quite heterogeneous behaviours. Some sensors, such as S_{35} (Figure 7.4), systematically recorded intensity values close to the maximum intensity, as they were located along streams where water flowed permanently during the entire study period. Other sensors, instead, were placed in more dynamical streams and displayed an electrical signal that fluctuated between the maximum intensity (during rainfall events) and 100000 – 150000 lux (during the driest periods: S_{10}). Other sensors, mainly located in the higher part of Zone 1, recorded no intensity at all during most of the time, with intensity peaks that were observed only during rainfall events, when discontinuous ephemeral ponds were generated in correspondence of the stream network (S_{05}).

Unlike the HOBOs of Zone 1, none of those placed in Zone 2 (Figure 7.4) was consistently wet during the whole study period. The probes activated during rainfall events and dried out afterwards with heterogeneous velocities, depending on their position: sensors located in the central part of the creek persisted being wet for longer (see e.g. S_{24}), while those placed close to the channel heads turned off very quickly after each rain event (S_{22}). Other sensors, while they recorded an increase in the electrical signal during precipitation events, remained consistently below the 270000 lux threshold for the entire study period (S_{40}).

A statistical analysis was carried out to assess the consistency between the hydro-

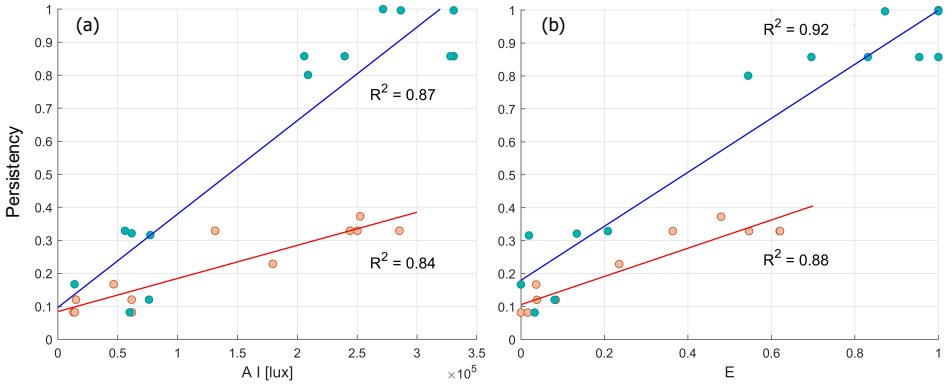

Figure 7.5: Scatter plots of persistency vs average intensity (a) and persistency vs exceedance of the threshold (b) of the sensors of Zone 1 (green points) and Zone 2 (orange points).

logically relevant indexes (namely, the *average intensity* and the *exceedance of the threshold*) calculated for each sensor and the persistency of the corresponding nodes, as derived from field surveys. Figure 7.5 shows the scatter plots of persistency vs. AI and persistency vs. E for 28 sensors of Zone 1 and 2. All the available data were represented in the same two plots in order to emphasize differences and similarities among the HOBOs located in different zones.

The working hypothesis is that an higher persistency of the nodes is reflected by an higher average intensity of the current recorded by the sensors and an enhanced probability that the electrical signal exceeds the selected saturation threshold. This hypothesis seems to be supported by the high coefficients of determination which were calculated from the data (R^2 always above 0.84). However, Figure 7.5 also shows that the morphological characteristics of the studied zones (altitude and heterogeneous land cover) can influence the electrical signal registered by the instruments. Data collected from sensors of Zone 1 are not homogeneous despite they are located close-by in the field. The HOBOs of Zone 1 are clustered in two separate groups (Figure 7.5): one cluster includes the sensors located downstream that are mostly wet ($E > 0.7$ and $AI > 2\ 10^5$ lux) and the other includes only the HOBOs located upstream that turn on only during rainfall events ($E \leq 0.2$ and $AI < 0.8\ 10^5$ lux). Instead, the tributary along which sensors of Zone 2 are located completely dries down, as indicated by the low values of the maximum persistencies observed in this area. The data points in these cases are evenly distributed along the regression line, indicating a more homogeneous internal distribution of the node persistencies. It is also interesting to note that the two zones display very heterogeneous regression slopes between mean intensity and persistency. Instead, the slopes of the regression lines between exceedance of the threshold and persistency are comparatively more similar in the two zones. This suggests that E might be a more robust indicator of the underlying hydrological dynamics experienced by the nodes in the network, regardless of the specific position of the sensors in the catchment.

Data collected by the sensors deployed along the watercourse provide information about the high frequency spatial and temporal dynamics of the stream network.

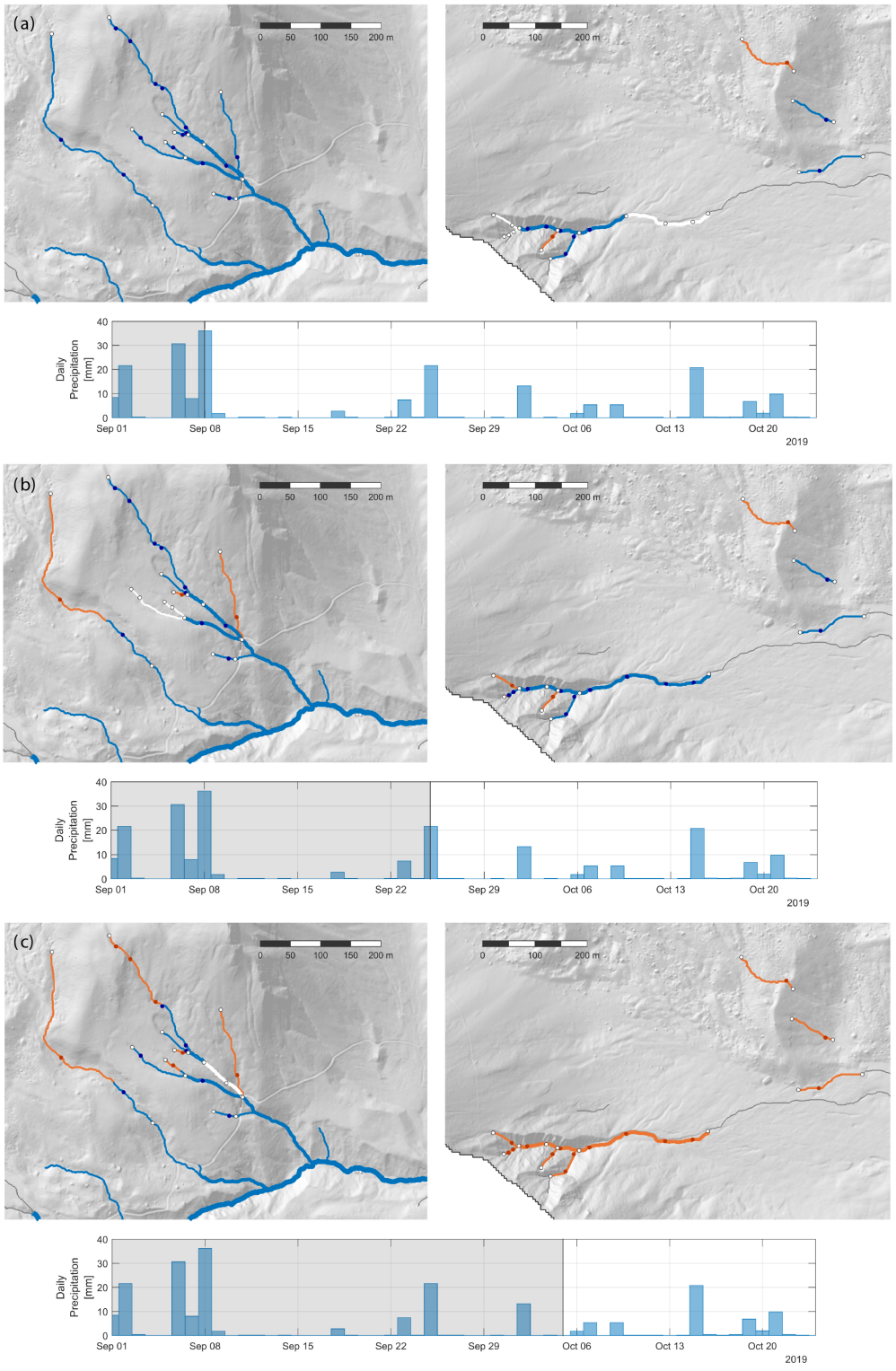

Figure 7.6: Map of the active stream network of Zone 1 (left) and Zone 2 (right) on the 8th of September (a), on the 25th of September (b) and on the 5th of October 2019 (c). Active stretches and sensors are blue, inactive are orange and no-data elements are white.

The full video of the observed river network dynamics is shown in Zanetti et al. 2021, while Figure 7.6 presents a sequence of snapshots taken from the video that represent the temporal evolution of the spatial configuration of active channels in the study catchment. Figure 7.6a represents the channel network during the most intense rainfall event of the period studied, on the 8^{th} of September, when all of the sensors of Zone 1 (left) were wet (blue dots). Not all the sensors of Zone 2 (right) had already been installed at that time. This circumstance explains the reason why some stretches are represented as no data (white dots) in that region. Also in Zone 2, on September 8, most of the network streams were wet, with the exception of two river segments (shown in orange) that remained dry during the entire study period.

After the rainfall event that was observed on September 8, 2019, the network kept drying out for several weeks, and then wetted up again, owing to a rain event that was observed on the 25^{th} of September (shown in Figure 7.6b). This precipitation event was less intense than the previous one and it was characterized by a lower antecedent precipitation. Consequently, some headwater branches did not get wet in both zones.

The snapshot in Figure 7.6c shows the network on October 5, three days after an isolated precipitation event that took place in between a relatively dry period. On that date, all the HOBOs of Zone 2 were dry, while only the downstream sensors of Zone 1 (those closer to the permanent part of the network) became wet. Figure 7.6c emphasizes, once again, the dynamical nature of the channel network in the study catchment, and the different hydrological behaviour of the two focus regions identified in this study.

The data suggest that the two regions of the study catchments are strongly heterogeneous, not only in terms of land cover but also in many features of the underlying network dynamics. The lower part of Zone 1 was permanently wet, with high values of E and persistencies close to 1 for most of the sensors. In the upper part of the same zone, instead, the network branches were more dynamical and they usually got wet in response to precipitation events. Along the main channel of Zone 2, instead, water was able to infiltrate and exfiltrate rapidly, creating frequent stream disconnections, promoted by the unstable morphology of the river bed. In this case, mean current intensities and node persistencies were consistently smaller than those observed in Zone 1.

In both regions, a good correlation between the persistency of the nodes and two statistical features of the electrical signal recorded by the ER sensors (namely, the mean intensity and the exceedance of a suitably selected saturation threshold) was found. This suggests that the statistics of the ER signals recorded in the field could be robust indicators of the hydrological status of different network nodes. In particular, ER time series could be used to extrapolate information on the spatial patterns of node persistency, which could be, in turn, used to define the hierarchy according to which the nodes in the network are activated in response to rain events and then deactivated during the subsequent drying (Botter et al. 2020).

7.3 A novel global dataset

The empirical activities described in section 2 allowed the monitoring of the dynamics of the active network in the Valfredda catchments. The results of these activities (sections 7.1 and 7.2), in combination with the available data pertaining to the other study catchments of this thesis, constitute a global dataset comprising 18 different study catchments located in Europe and eastern USA. The objective of this dataset is to provide a strong empirical basis for the validation and application of the theoretical and modeling tools presented in this thesis. As such, the catchments were selected to be very heterogeneous, spanning a wide range of latitudes, climates, land covers, geologies and sizes. Figure 7.7 summarizes the main climatic and hydrological characteristics of the study catchments. The figure indicates that the study catchments cover a wide range of climatic conditions in terms of mean precipitation, evapotranspiration, aridity and temperature. Furthermore, the catchments are characterized by heterogeneous elevations and catchment areas. Therefore, the dataset can be considered as representative of a broad range of climatic and morphological settings.

Table 7.2 which reports the study period, number and type of field observations for each study catchment. In all cases, the available data refers to prolonged field campaigns with regular observations lasting at least one year, in order to properly capture the intra-annual variability of the extent of the active network that results from multiple precipitation events.

The observed stream network dynamics are summarized by the maps of local persistency in Figure 7.8. All the network of catchments T_1, T_2 and T_3 have a low local persistency ($P_i < 0.4$), suggesting that these catchments tend to be very dry, with only sporadic activations of the network dictated by rainfall events. On the opposite, other catchments such as C_1, C_2, C_3 and F_1 show very high persistency, with a limited number of stretches having $P_i < 0.60$. This suggests that in these sites most of the stream network tends to remain active all year round and the dynamics are very limited. Nonetheless, most of the sites show local persistency ranging between 0 and 1, and a enhanced dynamicity of the stream network.

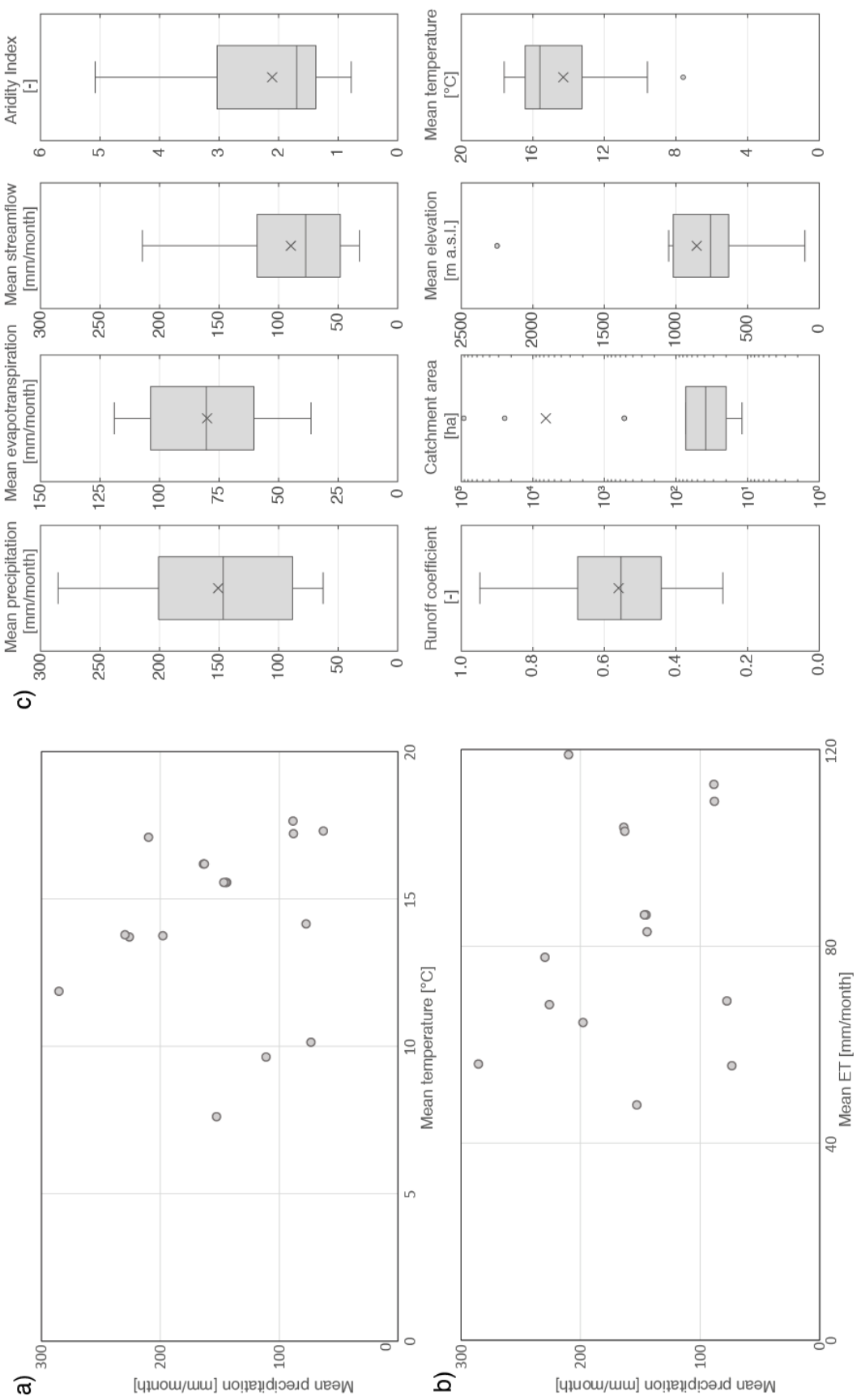

Figure 7.7: Representation of the study catchments in the Whittaker plot (mean annual temperature vs mean annual precipitation, panel a). Also shown is the scatter plot of the mean evapotranspiration and the mean annual precipitation across all the study sites (panel b). Panel c) shows box plots of the main climatic and morphological characteristics of the study catchments.

Table 7.2: Characteristics of the field campaigns carried out for the monitoring of the active stream network and accuracy of the hierarchical model.

Catchment code	Area $[km^2]$	**Survey type**	**# of surveys**	**Survey period**		**# of nodes**	**Accuracy**	Reference (watershed number[a])
A	247	ER sensors	33770	Aug-2015	Jul-2017	182	94%	Kaplan et al. 2019
C_1	0.12	Visual	7	Nov-2015	Dec-2016	323	100%	Jensen et al. 2017 (WS 18)
C_2	0.33	Visual	7	Nov-2015	Dec-2015	365	100%	Jensen et al. 2017 (WS 34)
C_3	0.4	Visual	7	Dec-2015	Dec-2016	707	100%	Jensen et al. 2017 (WS 32)
F_1	0.14	Visual	7	Jun-2016	Dec-2016	175	100%	Jensen et al. 2017 (WS 13)
F_2	0.16	Visual	7	May-2016	Dec-2016	243	100%	Jensen et al. 2017 (WS 10)
F_3	0.37	Visual	7	May-2016	Dec-2016	489	100%	Jensen et al. 2017 (WS 4)
H_1	0.14	Visual	7	Jun-2015	Jul-2015	861	100%	Jensen et al. 2017 (WS 6)
H_2	0.2	Visual	7	Jun-2015	Jul-2015	1429	100%	Jensen et al. 2017
H_3	0.43	Visual	7	Jun-2015	Jul-2015	2218	100%	Jensen et al. 2017 (WS 3)
P_1	0.25	Visual	7	Sep-2015	Jan-2016	1045	100%	Jensen et al. 2017
P_2	0.35	Visual	7	Sep-2015	Dec-2015	1225	100%	Jensen et al. 2017
P_3	0.73	Visual	7	Aug-2015	Mar-2016	906	100%	Jensen et al. 2017
S	920	Visual	78	Apr-2012	Oct-2019	40	96%	ONDE Dataset
T_1	0.63	Visual	35	Apr-2019	Jan-2020	368	99%	Botter et al. 2021
T_2	0.23	Visual	35	Apr-2019	Jan-2020	173	99%	Botter et al. 2021
T_3	0.46	Visual	42	May-2019	Jan-2020	205	99%	Botter et al. 2021
V_1	5.27	Visual	32	Jul-2018	Oct-2021	504	97%	This study
V_2	5.27	Visual	9	Jul-2018	Nov-2018	504	96%	This study

[a] If applicable, for gauged catchments at the experimental forests with a designated watershed number

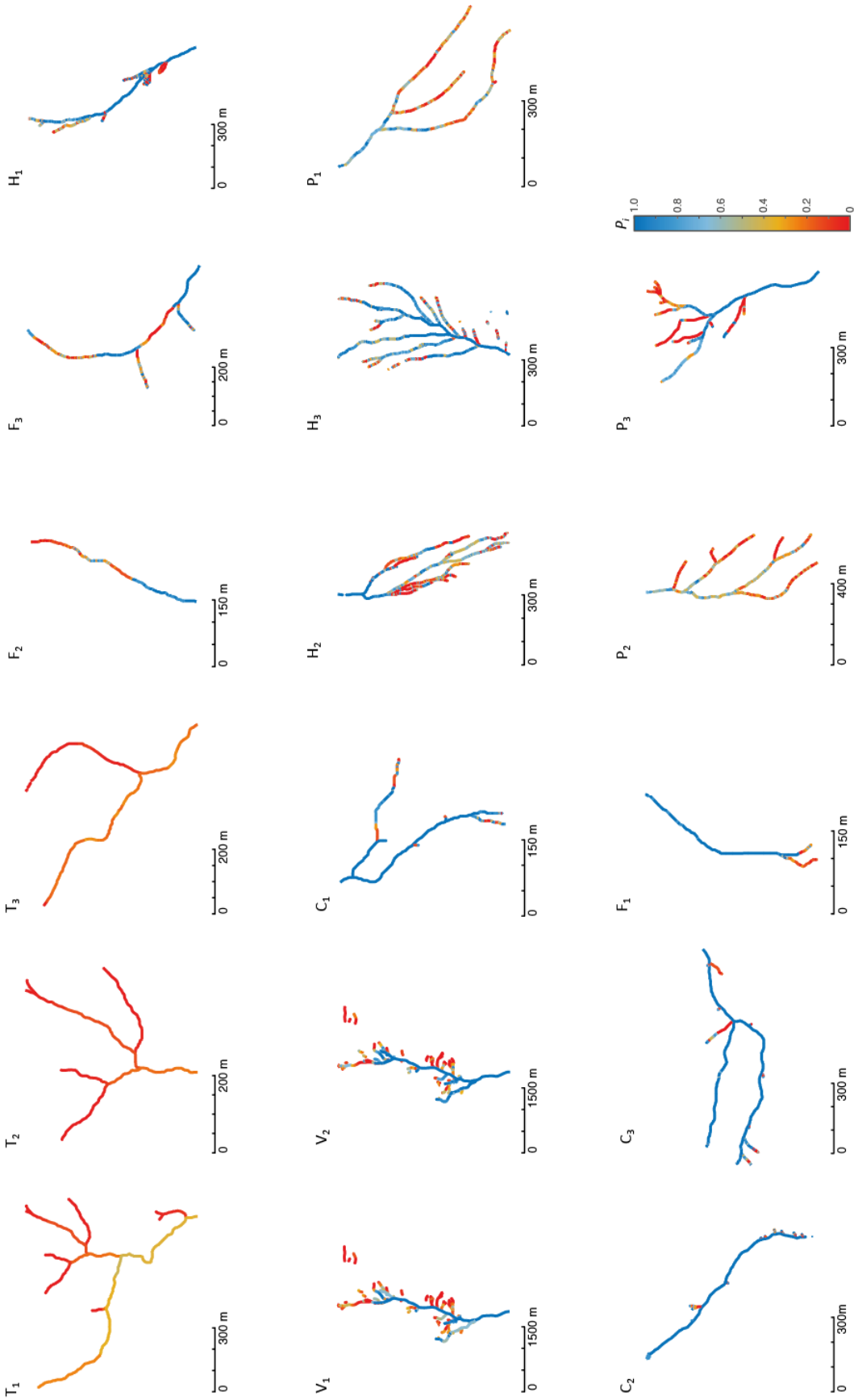

Figure 7.8: Maps of local persistency of the study catchments.

7.4 Validation of the hierarchical activation hypothesis

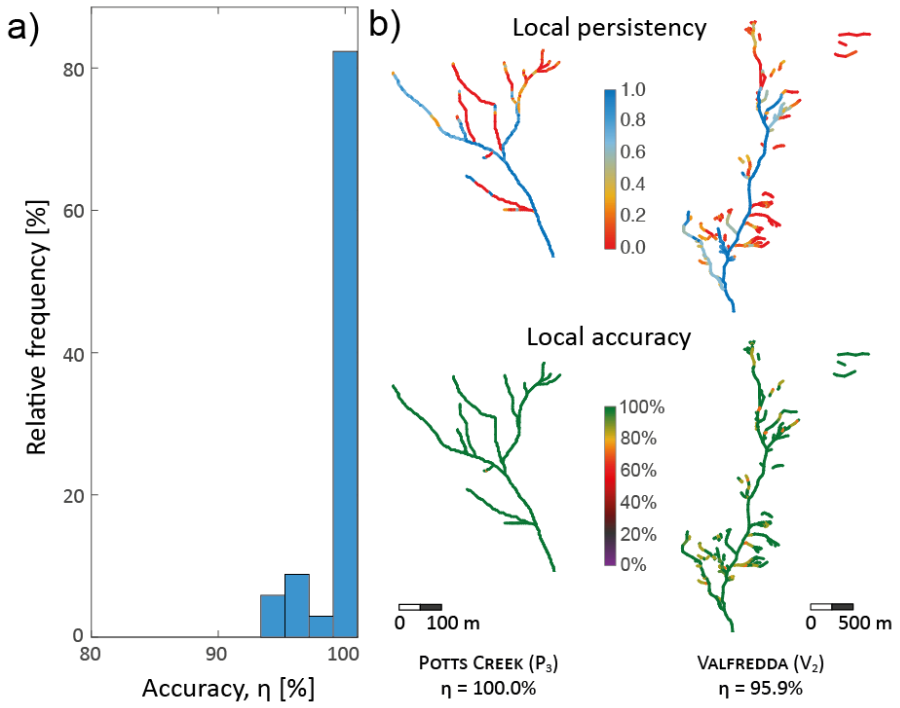

Figure 7.9: a) Relative frequency of the accuracy of the hierarchical model (relative number of nodes properly classified as wet or dry by the hierarchical model) for all the study catchments. The maps in b) show spatial patterns of local persistency and local accuracy of the hierarchical model in the best and the worst cases (respectively South Fork of Potts Creek, USA and Valfredda Creek, Italy). Analogous maps for all the study sites are reported in Appendix A.

The global dataset was used to validate the robustness of the hierarchical scheme of Section 4.3. For each study site, flow presence maps representing the observed active network on different dates were produced using multi-month field mapping campaigns (with a mean frequency of two weeks) or water presence sensors (with a sub-hourly resolution). These maps were converted into sets of geo-referenced nodes with binary states (wet/dry), and the local persistency of each node (P_i) was calculated as the relative fraction of data indicating the presence of flowing water in that location. Afterwards, each flow presence map was compared with the outcome of the hierarchical model, in which the network nodes were switched on from the most to the least persistent, until the total number of nodes observed as active during the corresponding survey was reached (section 4.3). Regardless of the underlying climatic and geologic complexity, the accuracy of the hierarchical model (here defined as the relative number of nodes properly classified as wet or dry throughout a river network during all the surveys) typically exceeded 99% (Figure 7.9b and Table 7.2), with a minimum accuracy around 95% for two European rivers, the Attert and the Valfredda (Figure 7.9b). The average accuracy is very high, and much higher than the accuracy of a random model that assigns the status of each node at random independently on the status of the other nodes but consistently

with the local persistency, which is $0.79 \pm 0.075\%$ for the selection of case studies (see Appendix A). Thus, the observations suggest that the most persistent nodes were generally the first to activate during individual rainfall events and the last to dry-out during the subsequent recessions. The less persistent nodes, instead, were mostly switched on only in response to the most significant rain events and when all the nodes with a higher persistency were already active.

The most common exceptions to the hierarchical behaviour observed in the set of case studies were the following: i) nodes with a relatively low persitency that activate in the early stage of a rain event (Poverty Creek); ii) lack of symmetry in the rate and/or the direction of wetting and drying processes (Valfredda, Turbolo); iii) inter-event shifts in the wetting mechanism (e.g. from the downstream propagation of a saturation front induced by intense events taking place after dry periods to the upstream expansion of saturated areas around the permanent network, as observed in the Valfredda). In spite of this complexity, the hierarchical phenomenon was dominant across the full range of climatic conditions, temporal resolutions and spatial scales explored in the paper. In particular, the hierarchical activation rule applied also to disconnected river networks, where the nodes with the same persistency are not necessarily adjacent because of local discontinuities of landscape and geology (see Figure 7.9b). This means that the hierarchical phenomenon is much more than a simple upstream/downstream propagation of a saturation front along the network (Godsey et al. 2014). In particular, these results indicate that stream sections potentially quite distant in the physical space (up to tens or hundreds of kilometers) might share the same average degree of persistency and exhibit systematically synchronous dynamics. Furthermore, the hierarchical scheme held also within catchments as large as several hundreds of km^2 (the Attert and the Seugne). These basins are characterized by significant internal landscape and climatic gradients that are potentially responsible for the unsystematic, selective activation of limited and specific portions of the river network. The ability of the hierarchical model to describe active stream dynamics in these larger river basins indicates that meso-scale channel network dynamics maximize the spatial correlation of the nodes' states (see section 4.4.1) and reflect an homogeneous signal, such as the total catchment storage, driven by mid-range antecedent precipitation (e.g. weekly to monthly rainfall, see section 7.7). Interestingly, the spatial homogeneity of the hydrological signal underpinning the hierarchical dynamics of temporary streams promotes the synchronization of node status within a channel network, regardless of the observed complex patterns of local persistency produced by spatially heterogeneous physiographic and morphometric features (see Figure 7.9b and Jensen et al. 2017).

The results shown in Figure 7.9 bear important practical and theoretical implications. For instance, the hierarchical behaviour of temporary streams can streamline empirical surveys of river network dynamics, with beneficial consequences on the ability to characterize spatiotemporal patterns of flow persistency (Fritz et al. 2013; Prat et al. 2014). In perfectly hierarchical networks, the adoption of ad-hoc monitoring strategies that exploit information available from previous surveys can reduce the number of nodes to monitor during a long-term field campaign with at least 10 surveys by 40 to 75 %, depending on the exact number of surveys and the mean

network persistency (see Appendix B). Although several initial surveys that include most of the network are needed to establish the hierarchy among the nodes, the saving in terms of number of surveys becomes particularly significant when the number of surveys exceeds 20 - as typically needed to capture event-based variations of the active length, see Table 1 in Senatore et al. 2021. This indicates that the hierarchical nature of stream dynamics could significantly facilitate the observational mapping of flowing streams in a broad range of settings, especially in large river basins. Furthermore, the existence of a fixed hierarchical order in the expansion and retraction of temporary rivers allows the identification of a one-to-one relationship between the total length of flowing streams and the spatial distribution of active nodes in the network, if a spatial map of the local persistency is known e.g. based on multiple field surveys.

7.5 Linking active length statistics to local persistency

The theoretical relationships between the statistics of the dynamic drainage density and the mean network persistency were tested using active length data derived from field surveys in the study catchments (Figure 7.10). As expected, the mean network persistency $\bar{P}$ well approximates the temporal average of the active drainage density normalized by the geomorphic drainage density, as implied by equation (4.27) (Figure 7.10a). The 1:1 relationship between the spatial average of the mean percentage of time during which a node is active and the temporal average of the normalized mean active length is implied by the linearity of the average operation. The scattering of the points is only due to the fact that the geomorphic drainage density was calculated independently from the number of network surveys based on geomorphic signatures of the landscape. Available data also confirm that the magnitude of CV_D is modulated by the mean network persistency across the entire set of study catchments, with higher values of CV_D and an enhanced sensitivity to $\bar{P}$ for low network persistencies (Figure 7.10b). Remarkably, the analytical model given by equation (4.32) captures the observed network length variability across the full set of study catchments ($R^2 = 0.97$), proving that the temporal variation of active streams are in fact linked to the mean persistency of the river network. All the experimental points obey to the inequality $CV_D < CV_D^{max}$, indicating that the observed temporal dynamics of active stream length are properly constrained by the theoretical limit given by equation (4.29). This finite universal limit of the active length standard deviation derives from the contrasting patterns of $CV_D^{max}(\bar{P})$ and $\bar{D}(\bar{P})$ shown in Figure 7.10. The relatively small distance of the experimental points from the theoretical limit given by equation (4.29) suggests that the total active stream length is about as dynamic as it can possibly be (i.e., the CV of network length or drainage density is not far from its maximum possible value). Active stream dynamics and temporarily-dry channels are known to modify the distribution of catchment travel times owing to changes in the length of channel and hillslope flowpaths (Durighetto et al. 2020; Van Meerveld et al. 2019), thereby affecting important biogeochemical and ecological properties of rivers across a broad range of hydroclimatic settings

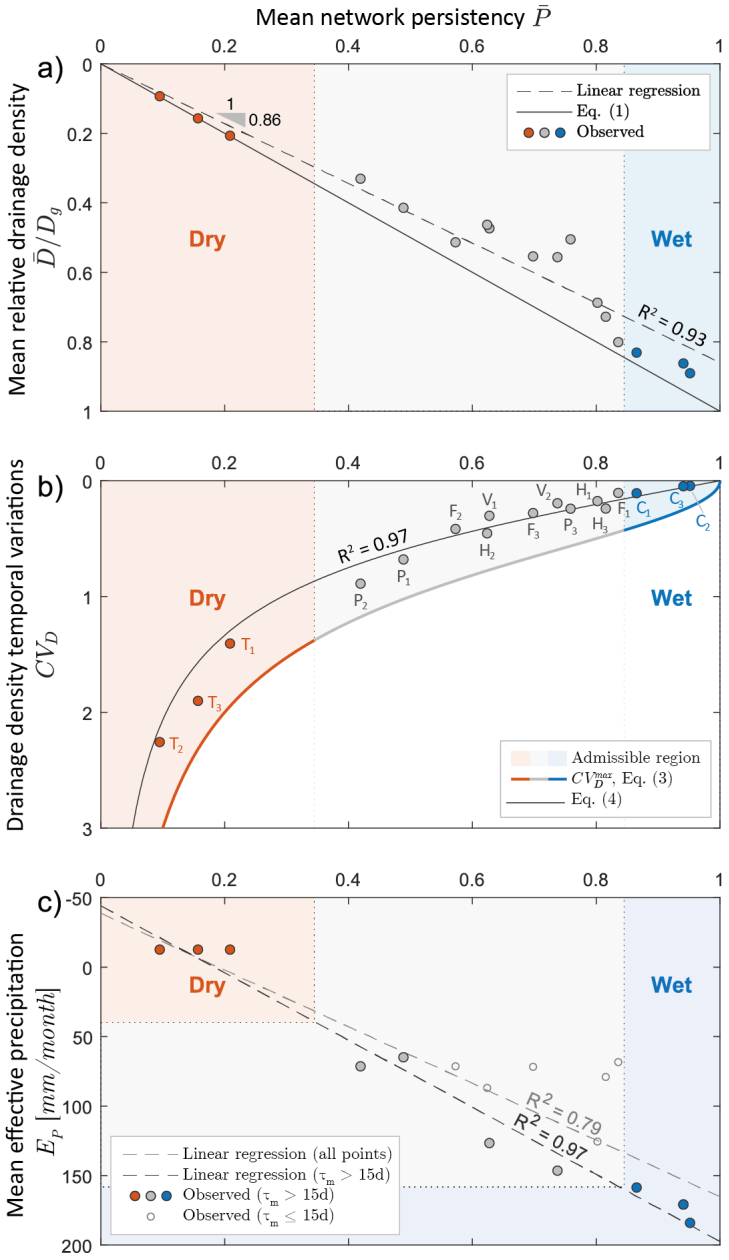

Figure 7.10: Climatic controls on the active drainage density. a) mean drainage density scaled to the geomorphic drainage density as a function of the mean network persistency, $\bar{P}$; b) coefficient of variation of the drainage density as a function of the mean network persistency $\bar{P}$. Also shown here are the maximum theoretical limit for CV_D (equation (4.29)) and the value of CV_D predicted by the hierarchical beta-model (equation (4.32)); c) the correlation between mean network persistency and effective precipitation (total precipitation minus potential evapotranspiration ET) during the period when the active network was surveyed (average monthly value among all the months during which at least one field survey was performed). Points with a lighter gray border represent cases in which the surveys are not evenly distributed within the study period (Hubbard Brook and Fernow) as the median time between all the possible pairs of survey dates, τ_m, was smaller than 15 days. P_3 was not included in this plot because of the lack of reliable precipitation data.

(Fritz et al. 2008; Gallart et al. 2017; Stubbington et al. 2018; Vander Vorste et al. 2020b). Thus, temporal variations of the active channel length should be properly taken into account in regional assessments of biogeochemical function of river networks, such as CO_2 outgassing and nutrient spiraling (Raymond et al. 2013; Gómez-Gener et al. 2016; Bertuzzo et al. 2017; Schiller et al. 2019; Keller et al. 2020).

Other relevant implications of these results stem from the identification of the major physical determinants of the mean network persistency. Surface flow is the byproduct of the excess water drained by the upstream contributing catchment, as proposed by Godsey et al. 2014; Prancevic et al. 2019. Thus, in line with these previous studies, the hypothesis is that mean network persistency represents an important climatic signature of river basins. Accordingly, $\bar{P}$, which was poorly correlated with drainage basin areas ($R^2 < 0.01$), was found to be strongly linked to the underlying climatic water balance, here represented by the effective precipitation, $P_t - ET$ (i.e., total precipitation minus the potential evapotranspiration during the surveyed periods), as shown by Figure 7.10c. Despite the high correlation between effective precipitation and persistency (overall $R^2 = 0.79$), some scattering appears in the observational data. This scatter is attributed to two factors: i) relevant inter-catchment differences of geological or morphometric features, as suggested by Prancevic et al. 2019; Stoll et al. 2010; and ii) an uneven distribution of the survey dates that might bias the relationship between the observed mean network persistency and the average climatic conditions during the study period for some catchments (light grey dots in Figure 7.10c). Nevertheless, a clear climatic signature is present within drainage density statistics: lower mean network persistencies and enhanced relative active length variability were observed in the drier catchments (with $CV_D > 1.5$ for $P_t - ET < 40\,mm/month$, as in the Turbolo site). Conversely, in the wettest site (Coweeta, where $P_t - ET > 160\,mm/month$), the mean network persistency approached unity and network dynamics are smoothed, with $CV_D \to 0$. This result offers novel insight on the impact of climate on the active stream length variability (Jaeger et al. 2014), and nicely complements existing modeling and empirical approaches for the characterization of the spatial patterns of flow persistency across a landscape (Prancevic et al. 2019; Jensen et al. 2019; Senatore et al. 2021). Therefore, the proposed framework may provide useful insights into the impact of climate on the temporal changes of the active drainage density.

Several studies have investigated the impact of rainfall regimes on the geomorphic drainage density, D_g (Melton 1957; Moglen et al. 1998; Collins et al. 2010; Sangireddy et al. 2016). However, the influence of hydroclimatic drivers on the active fraction of the network is not fully understood. Notwithstanding the variability of D_g across the study catchments (attributed to their geological diversity), these results confirm that the extent of active channel length is linked to the amount of excess precipitation in the contributing catchment, as previously proposed in the literature (Godsey et al. 2014; Senatore et al. 2021). This suggests the emergence of distinctive ecohydrological patterns within different climatic regions of the world. The largest temporal variations in the active stream length were found in the sites characterized by intermediate climates (i.e., $40 < P_t - ET < 100\,mm/month$

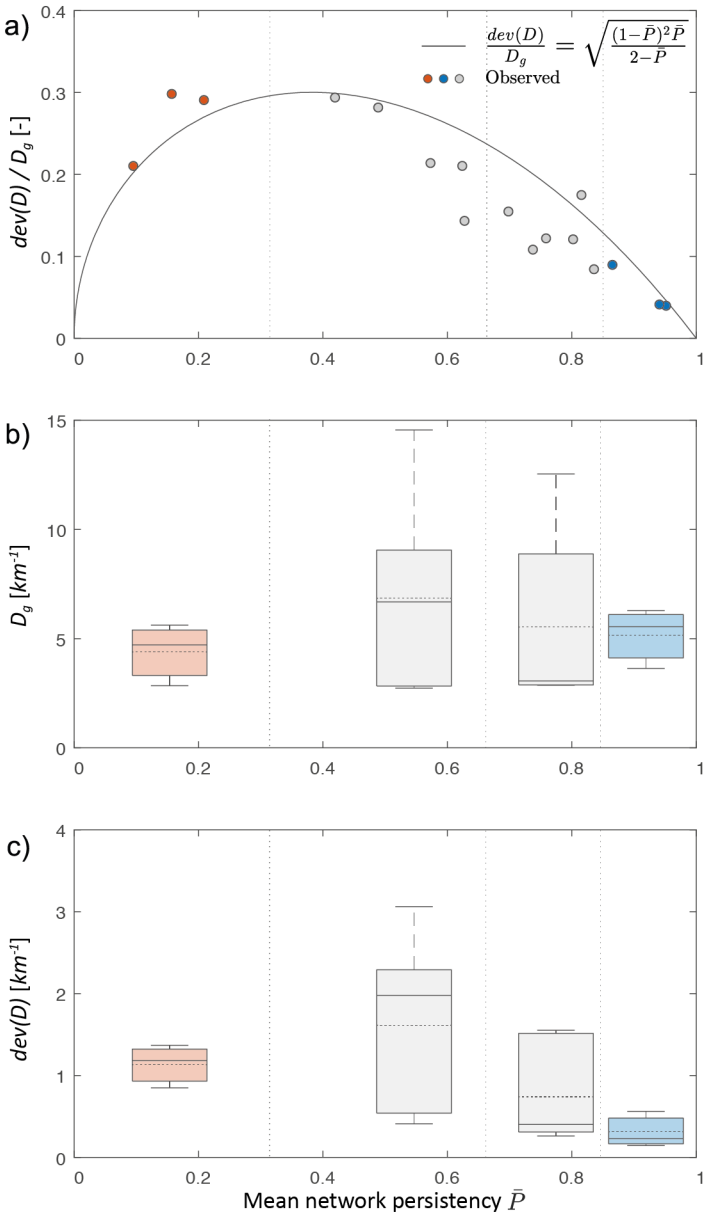

Figure 7.11: Dependence of key drainage density statistics on the mean network persistency, $\bar{P}$; the following statistics are shown in the three panels: (a) the standard deviation of the dynamic drainage density, $dev(D)$, scaled to the geomorphic drainage density, D_g; (b) the geomorphic drainage density; (c) the standard deviation of the active drainage density, that is proportional to the standard deviation of the active length through the contributing area. Panel a) shows a comparison between observed values of $Dev(D)/D_g$ (dots) and the corresponding theoretical prediction of the analytical model as derived from Eqs. (4.27) and (4.32) for all the case studies where active lengths were monitored; in panels b) and c) the box-plots represent the first, second and third quartiles of observed data (solid lines) aggregated for different persistency ranges (as indicated by the dashed lines). The average is shown as a dotted line, while the full range is represented by whiskers.

and $0.4 < \bar{P} < 0.6$), where the standard deviation of the active length and the geomorphic drainage density are concurrently higher (Figure 7.11). Crucially, for intermediate values of $P_t - ET$ both the overall dynamic channel length and its internal heterogeneity are enhanced. In these settings, in fact, the observed local persistencies ranged from 0 to 1 (Supplementary Information) revealing the presence of multiple expansion/contraction cycles that operate with diverse frequencies, from individual storms to seasons. This behaviour generates a gradient of spatially heterogeneous habitats, from predominantly terrestrial to lentic, widening the spectrum of adaptation strategies and increasing biodiversity (Vander Vorste et al. 2020b). In the driest site (Turbolo), the relative variability of D is much higher than in all other settings (Figure 7.10b), as almost the entire network is dynamic. However, the mean active length is typically reduced because of the predominance of dry reaches experiencing episodic activation. The lower persistencies induced by limited water availability entail shorter dynamical lengths of streams, regardless of the pronounced temporal changes of flow conditions experienced by dry rivers (Basso et al. 2016). The ability of the analytical framework to quantitatively describe this wide spectrum of behaviours suggests the general applicability of the proposed approach within large-scale studies and makes it a sound basis for developing more specific numerical tools aimed at interpreting or predicting channel network dynamics.

7.6 The stream length duration curves

The stream network dynamics of a catchment are efficiently summarized by the Stream Length Duration Curve (SLDC, see section 4.5). This section reports the SLDC obtained from the visual field surveys on the Valfredda site, in order to briefly explain how the main characteristics of a temporary streams are reflected by different features of the SLDC. Analogous results are obtained for all the study sites, as reported in Figure 7.13, and in section 7.9 where the SLDC is used to explore the different regimes of the active length.

The comparison between the empirical SLDC of the Valfredda catchment, that was obtained based on the field surveys performed in the summer and fall of 2018, and the prediction of the hierarchical model, i.e. the cumulative exceedance probability of the local persistency along the network (equation (4.20)), is reported in Figure 7.12b. The two curves display a very similar behavior, with a MAE between the quantiles of 0.32 km. This confirms that spatial and temporal variability of streams are tightly linked, thereby allowing the calculation of the SLDC as the cumulative exceedance probability of the mean persistency of the different network nodes.

The SLDC embeds important information about the dynamics of the active stream network induced by climatic variability. The value of the active stream length with a duration of 100% corresponds to the length of the permanent streams of the network, that, according to the empirical observations, for the Valfredda river is about 5 km. The difference between the maximum and minimum length, instead, is the total length of the intermittent streams, approximately 11 km for this study catchment. About 4.5 km of temporary network is active more than 50% of the time.

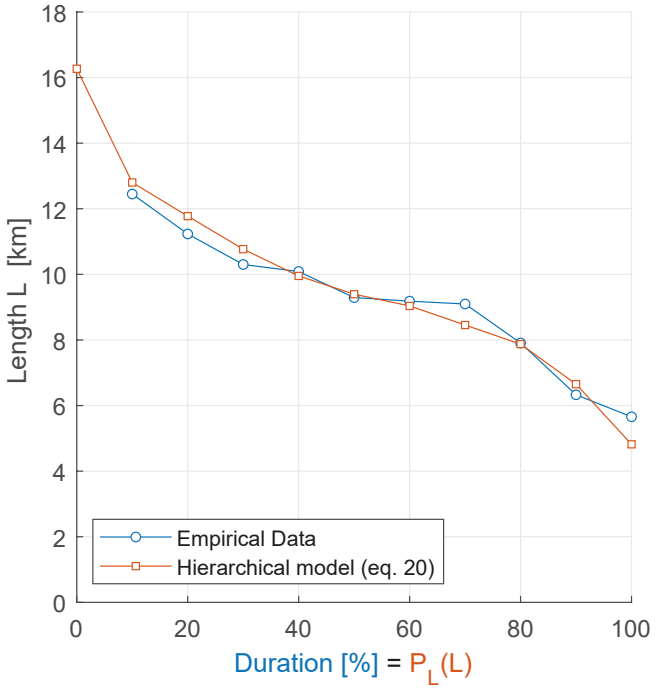

Figure 7.12: Empirical SLDC of the Valfredda catchment obtained with the plotting position method (blue), compared with the cumulative probability of the local persistency along the network (orange).

The median length (9.3 km, corresponding to a duration of 50%) is very similar to the mean length, suggesting that the distribution of active stream lengths is not significantly skewed. In the range of durations between 10 and 90%, the slope of the SLDC is pronounced and uniform, thereby implying that the whole stream network is very dynamical, and there are no preferential values of the active length that are observed with a particularly high probability. The predicted increase in the slope of the SLDC for durations below 10% also suggests that a considerable length of stream network (3.5 km) is activated only during extremely wet climatic conditions.

Figure 7.13 shows the Length Duration Curves obtained for all the other sites studied in this thesis. The Turbolo catchments (T1, T2, T3) prove to be the driest catchments of the study set, with completely dry networks for more than 50 % of the time. The part of LDC associated with the smaller durations are very steep, suggesting that these network only activate briefly in response to rainfall events, and dry out afterwards. At the other extreme, the catchments C2 and C3 are the less dynamic ones, with almost flat LDCs suggesting that at any time their networks are almost completely active. The LDC of catchments F1, F2, F3 and P3 tend to be flat in only the central part, suggesting the presence of a preferential configuration of the active network and a limited variability of the active length, that may be only generated by the most intense precipitation events and droughts. The Poverty (P1, P2) and Hubbard Brook (H2) catchments are the most dynamic ones, as the full range of lengths (from 0 to their respective maximum) is associated with durations spanning from 0 to 100 %.

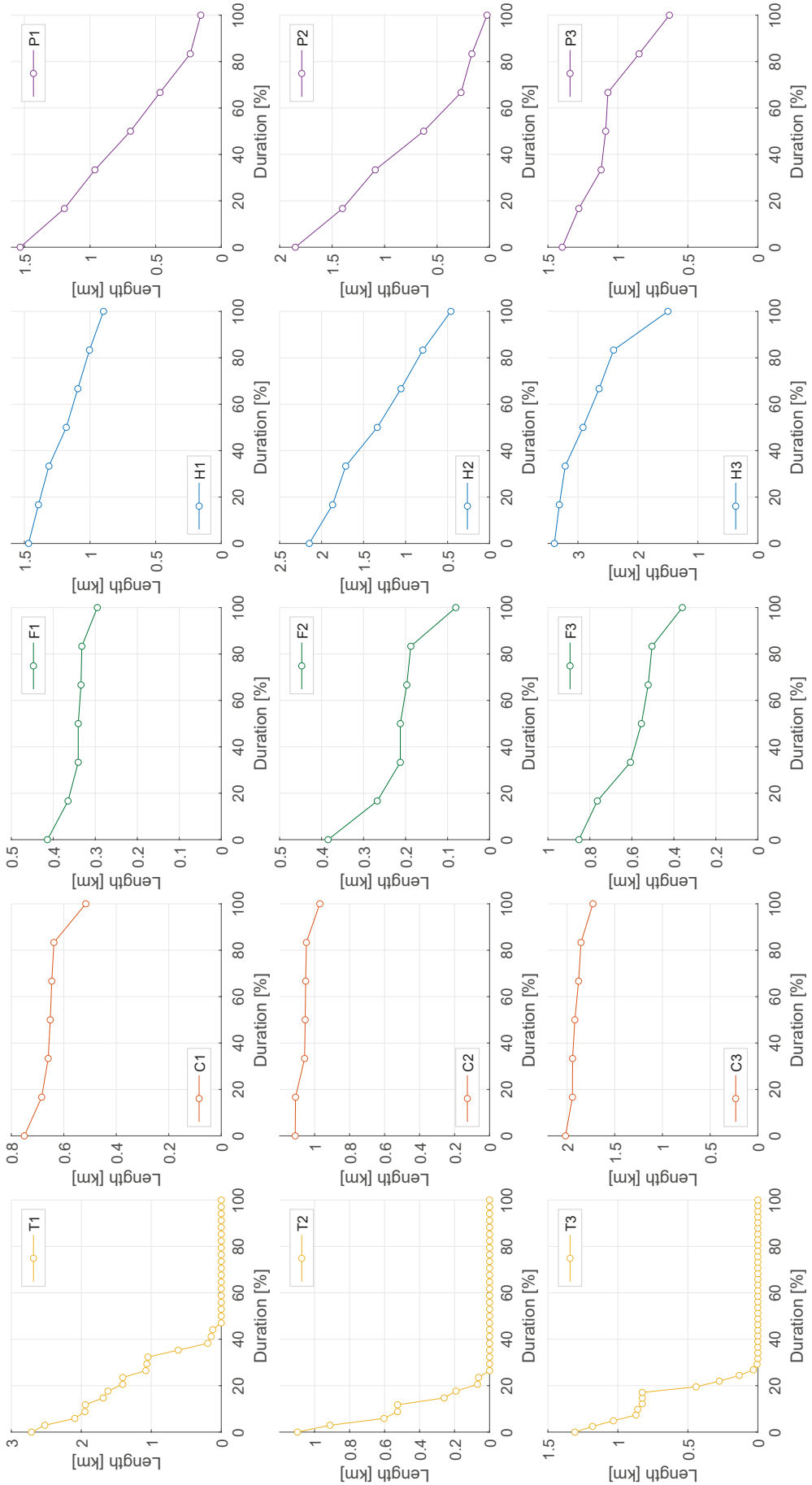

Figure 7.13: Stream Length Duration Curves of the Turbolo, Coweeta, Fernow, Hubbard Brook and Poverty catchments obtained with the plotting position method starting from the available empirical data.

7.7 A STATISTICAL MODEL FOR ACTIVE LENGTH

Three different empirical models for the estimation of the active length starting from climatic data were applied to the study catchments and compared, in order to understand how the unsteady climatic forcing controls stream network dynamics. In particular, the results reported here refer to the Rio Valfredda, and lie at the basis of the reconstruction of the continuous spatio-temporal dynamics of the active network reported in section 7.10. Nonetheless, the same methods could be used to obtain analogous results in all the other catchments.

The performance of the different models described in section 5.1 was assessed through the R^2 and the MAE of the linear regression between the observed and predicted L during the surveys carried out from July to November 2018. Despite its simplicity, model 1 provides a good description of L, with a R^2 of 0.96 (Figure 7.14). The values of the calibrated parameters are reported in Table 7.3, together with the mean and variance of L during the study period, the Akaike Index and the corresponding Akaike Weight. Figure 7.14a shows R^2 and MAE as function of the aggregation time scale for rainfall (T) in model 1. Two different local maxima of R^2 can be recognized: a first, narrow peak for $T = 5$ days ($R^2 \simeq 0.67$) and a second peak, much higher and wider, for $T = 35$ days ($R^2 = 0.96$). The same pattern is found in the MAE, for which two local minima can be identified for the same aggregation timescales mentioned above. This suggests the simultaneous presence of multiple expansion/contraction cycles of the active drainage network operating at different time scales (i.e. 5 and 35 days).

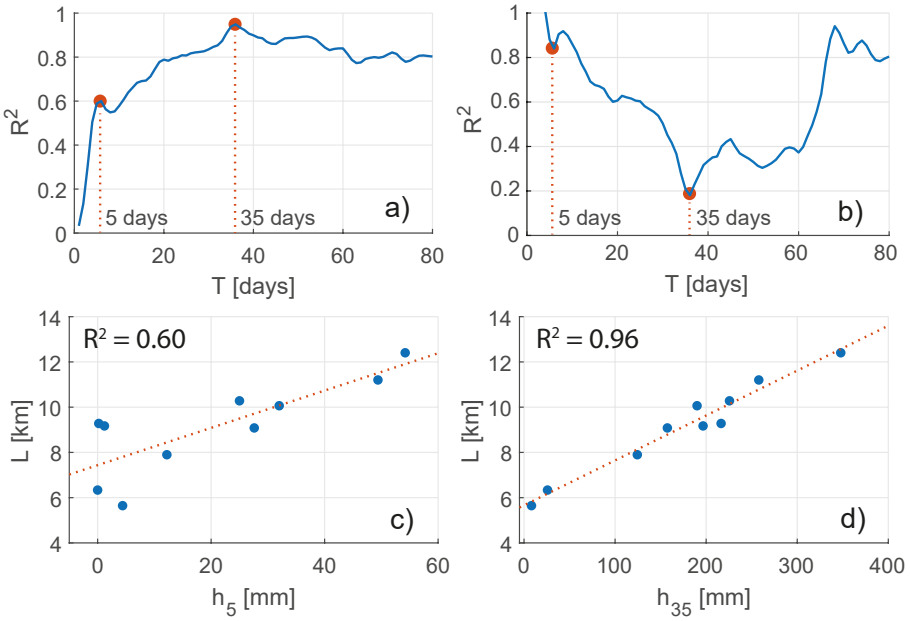

Figure 7.14: Performance of model 1 as a function of time period T in terms of R^2 (a) and MAE (b). Scatter plots of L vs h_T for the two time periods of 5 and 35 days (panels c and d, respectively); the blue points correspond to field surveys, the orange dotted line is the linear regression. The P-value of the linear regression is smaller than 0.015 for $4 \leq T \leq 66$ *days*, and smaller than 0.05 in all other cases.

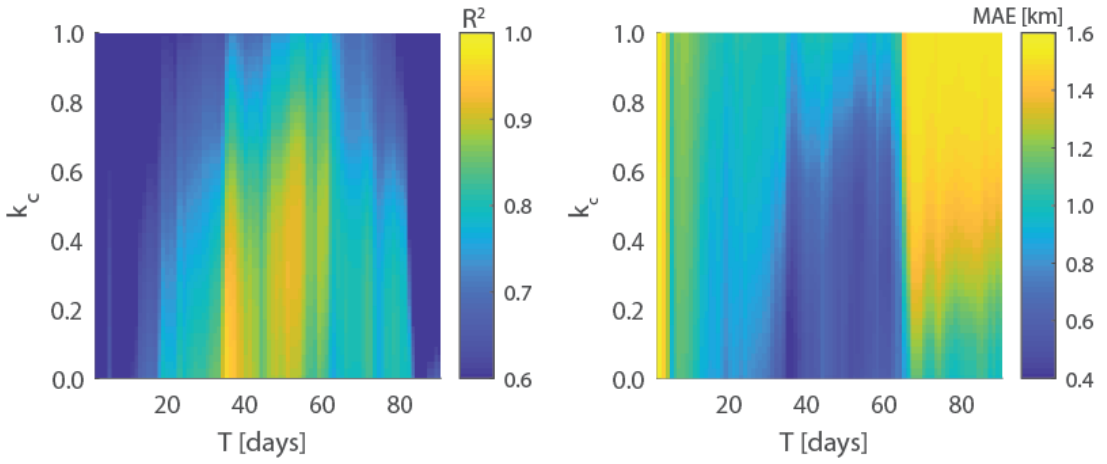

Figure 7.15: R^2 and MAE of model 2 as a function of time period T and crop coefficient k_c.

Figure 7.14c shows the scatter plot of L against h_5, which is the cumulative rainfall observed during the 5 days prior to each survey. Data points appear to be aligned quite well along the regression line for high values of h_5, while they are more scattered for small values, probably because after 5 days of little or no precipitation the hydrological condition of the catchment is dictated by slower hydrological processes that are more affected by long-term precipitation patterns. On the other hand, when a considerable rainfall event occurs, a significant fraction of the network is impacted by faster hydrological dynamics, which are in turn affected by short-term precipitation.

The scatter plot of L against h_{35}, the cumulative precipitation in the 35 days before each survey, is reported in Figure 7.14d. In this case, all the points are well aligned on the regression line and the model performance increased ($R^2 = 0.96$) relative to the case in which h_5 was used as a predictor for L. The increased performance of the model suggests that, at the catchment scale, the river network dynamics are mainly controlled by processes occurring on monthly timescales. Further, note that h_{35} can be seen as the sum of h_5 and the precipitation from 5 to 35 days prior to the surveys. Thus h_{35} includes, to some extent, the cumulative effect of the variability of short-term and long-term precipitation. As a result, the Pearson correlation coefficient between h_5 and h_{35} is 0.73.

Compared to model 1, model 2 introduces the effect of evapotranspiration through the parameter k_c. Figure 7.15 shows R^2 and MAE as function of the two calibration parameters, T and k_c, for model 2. Model performance generally decreases for larger values of k_c, and reaches its maximum for $k_c = 0$, a value for which this model corresponds to model 1. For fixed values of k_c (i.e. along horizontal lines in the plot of Figure 7.15), the patterns of R^2 (and MAE) are the same as in model 1, with a wide peak around $T = 35$ days and high values of R^2 up to $T = 60$ days.

The performance of model 3 as a function of the time periods T_1 and T_2 is shown in Figure 7.16, where $R^2(T_1)$ exhibits a peak for $T_1 = 5$ days and a global maximum at $T_1 = 35$ days and $R^2(T_2)$ follows the same pattern, generating the maximum R^2 for $T_2 = 35$ days. As a consequence, the optimal combination of T_1, T_2 is (5, 35)

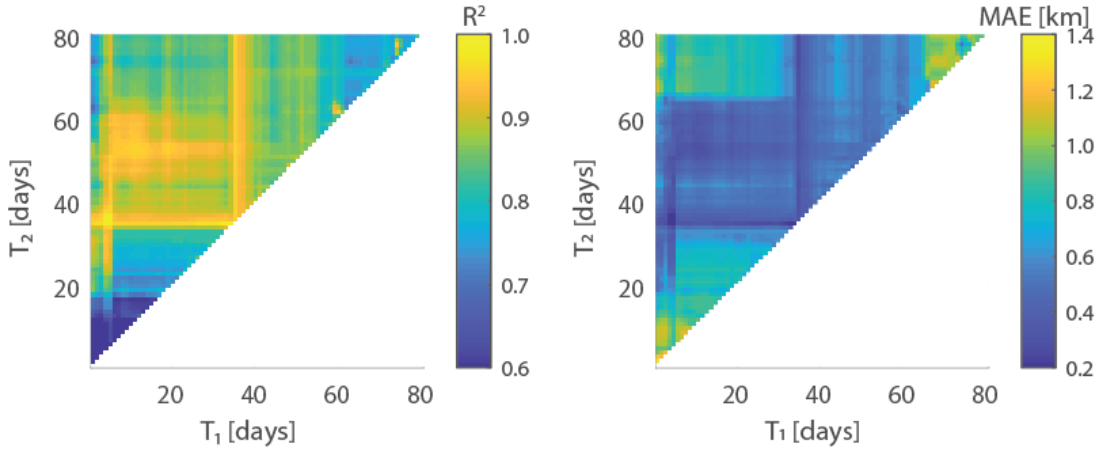

Figure 7.16: R^2 and MAE of model 3 as a function of the two time periods T_1 and T_2.

days. This model reaches $R^2 = 0.99$, further improving the performance of model 1 because it simultaneously accounts for processes happening on two different time scales. The Belsley collinearity test between the cumulative precipitation for the two relevant time periods identified by calibration produces a maximum scaled condition index around 3, indicating that collinearity is not an issue for the given model.

All the models were validated through a leave-one-out cross validation technique. As reported in Table 7.3, the standard deviation of the calibrated parameters is very small, originating coefficient of variations (CV) for each model parameter in the order of 0.01. The small variability of the parameters on different training subsets is an indicator of the robustness of the models. Table 7.3 also shows the MAE and its standard deviation for each calibrated model. The MAE coefficient of variation is very small, indicating the robustness of the approach regardless of the specific calibration subset chosen for calibration. The mean MAE exhibits the same pattern of R^2, being smaller for model 3 and higher for model 1, particularly when using h_5 as predictor variable.

The additional survey performed on January 18$^{\text{th}}$, 2019, was used to get a preliminary indication of the performance of each model during winter conditions, when snow dynamics affect the hydrology of the site. Model 1 shows the smallest absolute error, 0.19 km, when h_{35} is used as independent variable, while the same model produces the highest error (1.9 km) with h_5 used as a predictor of L. This is arguably related to the effect of snow storage that impacts the water balance during relatively short time-scales. Model 3, that combines the two predictors together, has an absolute error of 0.3 km. These errors are comparable to the MAE of the models during the calibration/validation period, suggesting that the same approaches might be valid also during the winter season. However, more data is needed to confirm this hypothesis.

The different models were formally ranked using the Akaike Weights (AW), as reported in Table 7.3. Model 1b is the best model, according to the Akaike Weights, as it is able to provide a good description of the dynamics of L using a limited number of parameters. Model 2 has one parameter more than model 1, with no

Table 7.3: Comparison of the calibrated parameters and performances (in terms of R^2 and Akaike Weights) of the different models. Model 1 is presented twice, considering for the parameter T both the local optimum of 5 days and the global optimum of 35 days.

Model	**# of calibrated parameters**	**Regression parameters**			R^2	MAE	**AW**
1a	3	T	5	days	0.64	1.17 ± 0.81	0.224
		k_0	7.4 ± 0.3	km			
		k_1	0.082 ± 0.008	km/mm			
1b	3	T	35	days	0.96	0.40 ± 0.20	0.688
		k_0	5.7 ± 0.07	km			
		k_1	0.020 ± 0.0004	km/mm			
2	4	T	35	days	0.96	0.40 ± 0.20	0.084
		k_c	0	-			
		k_0	5.7 ± 0.07	km			
		k_h	0.020 ± 0.0004	km/mm			
3	5	T_1	5	days	0.99	0.28 ± 0.20	0.004
		T_2	35	days			
		k_0	5.8 ± 0.09	km			
		k_1	0.022 ± 0.0002	km/mm			
		k_2	0.017 ± 0.0005	km/mm			

performance improvement. In fact, the model 2 calibration results in $k_c = 0$, for which the behavior is the same as model 1. As a result, model 2 has a lower AW than model 1 because the same performance can be obtained with less parameters. Model 3 allows a slight increase in model performance, though it requires two additional parameters. As a consequence, model 1 has a significantly better rating than the other models, since it represents the optimal trade-off between goodness of fit and model complexity.

The simulated L time series for models 1 and 3 are compared in Figure 7.17. The main differences occur during and shortly after the major precipitation events; this is particularly visible for the large rainstorm at the end of October. Such differences are due to model 3 being able to better capture the expansion/contraction cycles of the active drainage network in response to short-term and long-term precipitation. Model 1, on the other hand, only captures long-term L variability induced by monthly rainfall dynamics, and it is likely to underestimate the actual short-term temporal variability of L.

One of the main goals of this study was to quantitatively analyze how the unsteady nature of the climatic forcing controls stream network dynamics. Empirical data and model results indicate that the temporal dynamics of the stream network length are mainly driven by the observed patterns of short and long-term antecedent precipitation (timing and amount). The comparison of the different models also suggests that evapotranspiration does not affect significantly the observed intra-seasonal changes of stream length in the Valfredda catchment, possibly due to the high runoff ratios typical of this Alpine region and the low percentage of forested areas (almost 30% of the total area).

The modeling results indicate the presence of multiple expansion and retraction cycles operating at different time scales behind the observed dynamics of the Rio

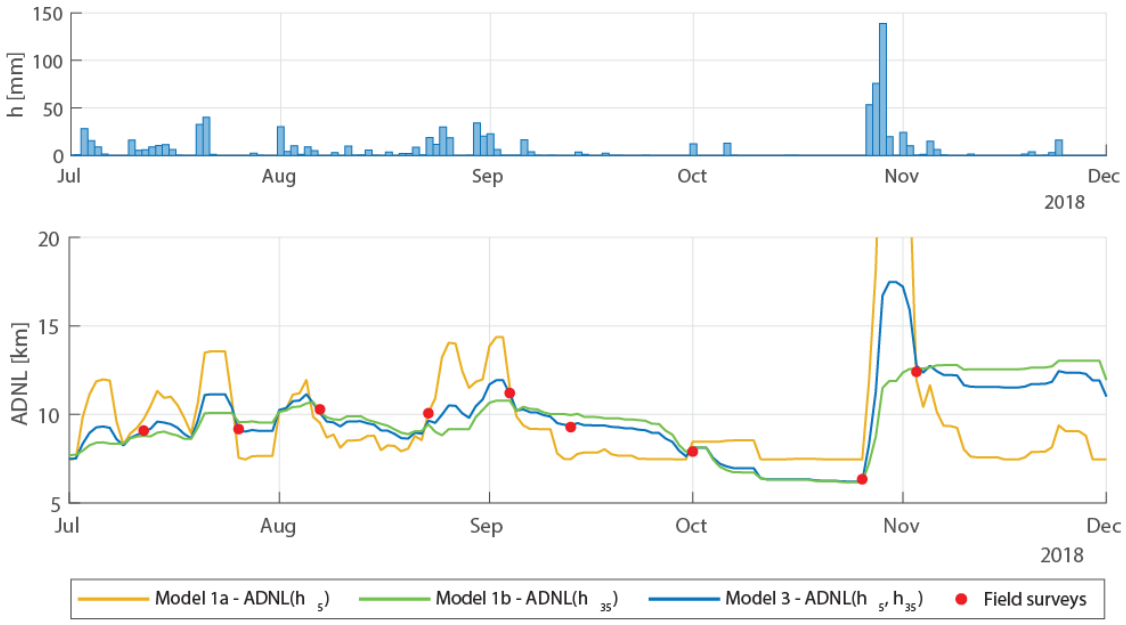

Figure 7.17: Comparison of the calibrated models. The top plot shows precipitation during the period from July, 1^{st} to November, 30^{th} 2018. The bottom plot shows L as calculated by the calibrated models. Model 2 is not reported as it is the same as model 1b. For clarity, L axis has been limited to 20 km even if the maximum length reached by model 1 is about 32 km.

Valfredda stream network. These overlapping dynamics may be in turn controlled by two distinct hydrological processes: i) quick subsurface flow in the root zone feeding temporary streams; and ii) slower groundwater flow generated by the aquifers supplying water to the less dynamical reaches of the river network.

7.8 Active length vs. discharge power-law relation

The available hydrologic data and the data derived from the water presence sensors were also used to study the relationship between discharge and active length in the Valfredda catchment, as reported in this section. The same type of analysis could be performed for all the study catchments, and lies at the basis of the characterization of the flow and active length regimes of section 7.9.

The temporal evolution of rainfall (h), total discharge and total active length during the entire study period is shown in Figure 7.18. During the first precipitation event, the most intense of the period, observed variations of Q and L were both significant. After September 11, instead, the intensity of the events was smaller and discharge variations were barely noticeable less important. However, ER sensors indicate that small rainfall volumes were able to activate several channels for some days, leading to noticeable changes in the total wet length L. Overall, the Figure indicates that the dynamics of L were mainly driven by precipitation, the temporal pattern of which differs from the corresponding streamflow dynamics because of the non linearity of

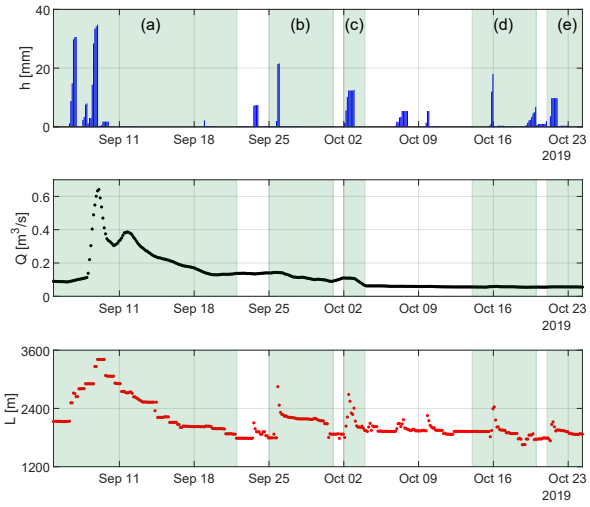

Figure 7.18: Top: temporal evolution of rainfall during the study period. Centre: temporal evolution of catchment discharge, $Q(t)$, during the study period. Bottom: temporal dynamics of active length, $L(t)$, during the study period. Areas in green represent the periods during which active length and discharge are plotted in figure 7.19.

rainfall-runoff mechanisms.

Figure 7.19 shows the joint changes in active length and catchment discharge observed during the five periods shaded in green in Figure 7.18. During the most consistent precipitation event of the period (September 8), the peaks of active length and streamflow were reached at the same time (Figure 7.19a). However, during the early recession of Q, the active length remained stable and close to its peak value. Afterwards, the discharge showed a non-monotonic behaviour with a small second peak, while L decreased consistently.

During the precipitation events that took place between the 25^{th} and the 30^{th} of September (Figure 7.19b), and between the 02^{nd} and the 03^{rd} of October (Figure 7.19c), the maximum active length was reached a few hours after each rain pulse, though in the absence of significant Q variations. Afterwards, the wet length first experienced a rapid decrease (again without significant changes in the discharge) and then it remained almost steady while the discharge kept decreasing. A rainfall event preceded the event shown in Figure 7.19b and it was responsible to increase the catchment moisture conditions prior to the considered event. Therefore, after the end of the rainfall input, the active length remained stable for some time before it started declining. The trend observed during the event occurred between October 02 and 03 (Figure 7.19c) is similar to that shown in Figure 7.19b, but in this case, the soil was drier before the event and the precipitation was less intense, thereby inducing a quicker decrease of the active length as compared to what observed in the recession between 09/25 and 09/30. In both cases, however, consistent variations of the wet length ($\Delta L \simeq 1km$) corresponded to comparatively small variations of the discharge ($\Delta Q \simeq 50l/s$).

The rain events that took place between the 14th and the 18th of October (Figure 7.19d) and between the 20th and the 24th of October (Figure 7.19e), instead, exhibited a different trend: the maximum wet length preceded the maximum discharge that was reached only when the active length was almost back to its initial value. In both these cases, the intensity of the rainfall events was small and the variations of Q were barely noticeable ($\Delta Q \leq 5l/s$).

Figure 7.20 summarizes the joint changes of wet length and discharge during the whole study period, for both the total values of L and Q (Figure 7.20 a) and for their dynamical contributions L_d and Q_d (Figure 7.20 b). As expected, in both cases, the pattern is similar. The variations of Q caused by the first precipitation event

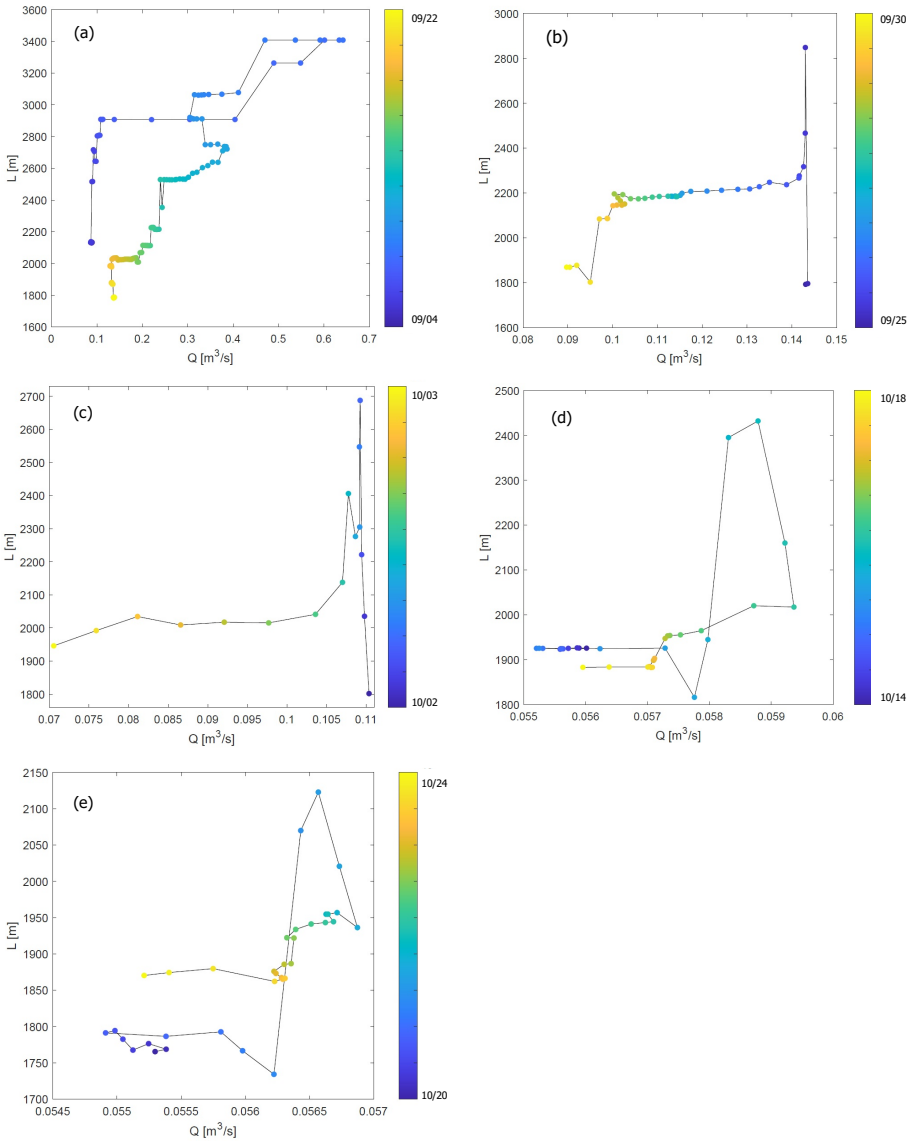

Figure 7.19: Plots of discharge and active length during individual events across the study period, as indicated in Figure 7.18.

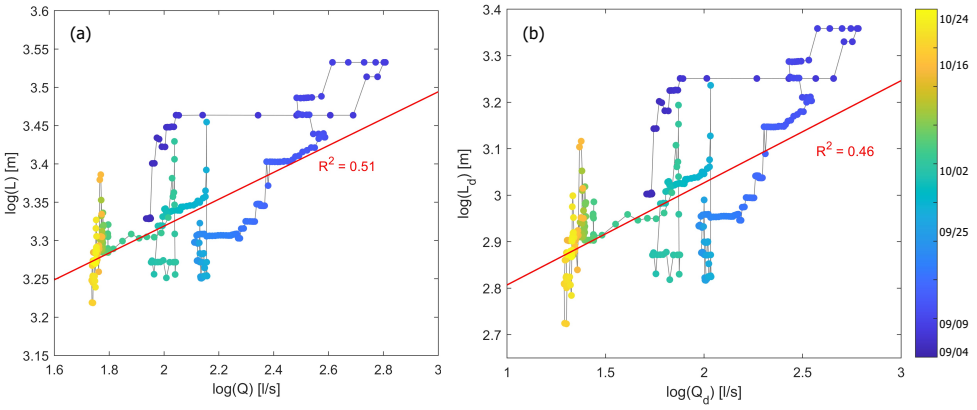

Figure 7.20: (a) Plot of total discharge (Q) and total active length (L). (b) Plot of dynamical discharge (Q_d) and active length (L_d) for the entire period studied.

(blue dots) are larger than those observed in the remainder of the period. Instead, active length dynamics are observed during the entire study period. The available data of Q and L were fitted with a power law relationship, of the type shown in eq. (5.16).

While $log(L)$ and $log(Q)$ are linearly correlated ($p - value < 10^{-5}$ at the 0.01 significance level), a pronounced scatter of the points around the regression line is also observed, mainly due to the effect of small rain events. This scatter underpins the relatively low value of the coefficient of determination ($R^2 = 0.48$) of the power-law model. There is no noticeable difference in the scattering of the points in the two plots of Figure 7.20, as the observed pattern is mainly driven by the dynamical components of L and Q. In both cases, the exponent of the power-law model b is close to 0.2, which is relatively low but still falls in the literature range (Godsey et al. 2014; Prancevic et al. 2019).

7.9 Streamflow and length regimes

This section combines the experimental observations with the analytical derivations of section 5.2, which are grounded on a well-established streamflow probabilistic model, to provide a parsimonious probabilistic description of the coupled dynamics of streamflow and active length of a catchment.

These results are derived from the application of the theoretical setup described in section 5.2.4, which by construction should be general and suitable for a wide range of climates and landscapes. The main limitation on its applicability, however, is related to the number and frequency of available simultaneous observations of streamflow and active length that is necessary to correctly capture the inter-event coupled dynamics of active length and streamflow. For this reason, these regimes were studied only for the Valfredda and Poverty catchments, where water presence sensors were employed to continuously monitor the dynamics of the active network

for a number of expansion/contraction cycles, and for the Turbolo creek, where the visual field surveys were conducted at a weekly interval.

Starting from the available hydroclimatic data, the parameters of the analytical model have been estimated for each case study, as shown in Table 7.4. These parameters enabled the calculation of the analytical distributions of q and L, which were then compared with the corresponding empirical counterparts, as discussed in the following.

Table 7.4: Summary of the fitted streamflow and length parameters for the different case studies. Note that the winter season of the Poverty Creek was divided into two subperiods (winter 1 and winter 2) with contrasting characteristics, as detailed in the SI.

Catchment	**Period**	α $[cm]$	λ $[d^{-1}]$	k $[d^{-1}]$	**Fitting method**	a $[d^b/cm^{b-1}]$	b $[-]$	R^2 $[-]$
Valfredda	Autumn	3.00	0.14	0.05	a-d	0.40	0.17	0.52
Poverty Creek	Spring	9.00	0.32	0.14	a-d			
	Summer	0.72	0.23	0.19	a-c			
	Autumn	0.92	0.25	0.20	a-c	0.30	1.09	0.77
	Winter 1	0.50	0.29	0.12	a-d			
	Winter 2	6.00	0.34	0.14	a-d			
Turbolo	Spring	0.52	0.20	0.07	a-c			
	Summer	0.91	0.04	0.06	a-c	6.17	0.50	0.21
	Autumn	0.80	0.16	0.13	a-c			
	Winter	0.95	0.20	0.10	b-d			

7.9.1 Flow duration curves and stream length duration curves

In the Valfredda catchment the effective rainfall frequency was moderate (one flow pulse every 5 days on average), whereas the observed recession rate was much lower, leading to an average response time of 20 days (Table 7.4). Despite the process complexity, the analytical model was able to capture reasonably well the streamflow statistics observed in the Valfredda. The analytical $P_q(q)$ underestimated low discharges and overestimated high streamflows, though reproducing in a reliable manner the shape of the observed cdf (Figure 7.21a). The MAE, evaluated as the

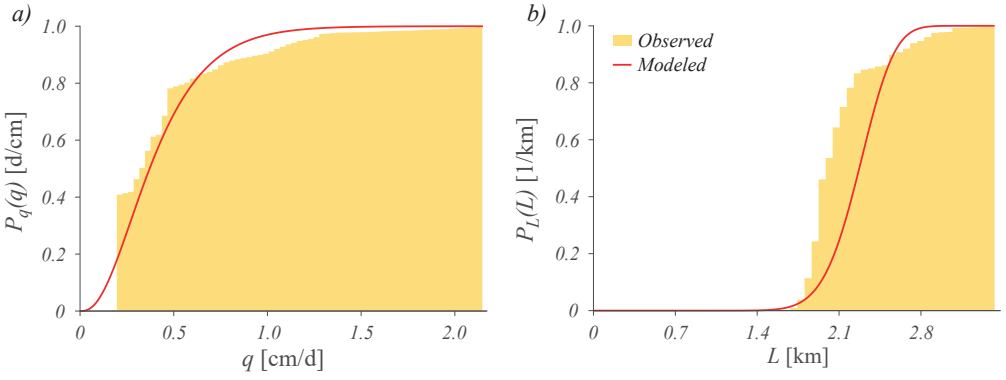

Figure 7.21: Cumulative distribution functions of streamflow ($P_q(q)$, panel a) and active length ($P_L(L)$, panel b) for the Valfredda site: comparison between models and observations.

mean difference between the modeled and the observed discharges associated to the 0.2, 0.4, 0.6, and 0.8 quantiles of the distribution, is 0.054 cm/d. The relatively low value of the $SMAE$ (12.7%) indicates a good performance of the model in this case.

The shape of the discharge cdf mirrored the relatively high frequency of flow-producing events and the importance of groundwater contributions to the discharge, which reduced the observed discharge variability and led to a persistent flow regime. This behaviour complied with the climate of the region. In fact, most of the Alpine rivers in this area are characterized by a constant water supply during the summer and the early fall, which is due to the high frequency of rainfall events (Botter et al. 2010b).

The network extension scaling exponent b, which represents the river dynamicity, is equal to 0.17 indicating a reduced responsiveness of the active length to changes in the underlying climatic conditions. The relatively low value of the R^2 ($R^2 = 0.52$) is related to the scatter of the points around the regression line which is caused by the high variability of observed active lengths for a given discharge, especially during moderate rain events.

The analytical cdf of the active length (eq. (5.19)) mirrors the behaviour of the underlying streamflow distribution (Fig. 7.21b). The plot shows that the modeled $P_L(L)$ underestimates low length probabilities and overestimates high length probabilities, but it is able to fit reasonably well the observed cdf of L. The MAE, evaluated as the difference between the analytical and the observed active length cdfs is relatively low and equal to 0.091 km. The performance of the analytical model was deemed satisfactory ($SMAE = 14\%$), in the light of the simplicity of the approach, the limited number of the required parameters and the geological complexity of the study catchment. The shape of $P_L(L)$ suggested the presence of limited temporal changes in the active length, which are represented by a perennial active length regime. In fact, the presence of significant groundwater contributions to the discharge ensured a continuous supply to the perennial portion of the drainage network (1045 m).

In the Poverty Creek, the mean recession rate varied between 0.2 and $0.12\,d^{-1}$ depending on the time of the year, while the mean frequency of effective rain pulses was in the range ($0.23\,d^{-1} - 0.34\,d^{-1}$). The mean intensity of effective rain events, instead, shows a marked variability across the seasons (Table 7.4). The annual streamflow cdf of the Poverty Creek has been calculated as a weighted average of the seasonal $P_q(q)$. The annual flow regime is influenced by the presence of seasonal droughts generally observed during the summer and the fall. During the summer, in particular, the ratio λ/k was slightly larger than 1, with modal discharge values close to zero and an intermediate-to-persistent flow regime (Figure 7.22a). Summer and autumn were characterized by high temperature and evapotranspiration rates, which induced low discharge rates and pronounced event-based streamflow fluctuations. On the other hand during the spring the mean discharge was much higher, and the frequency of flow pulses was larger than the corresponding recession rate, leading to a persistent flow regime in which P_q was almost zero for $q < 0.6\,cm/d$ (Figure 7.22c). While the seasonal analytical distributions didn't perfectly represent

the observations across all the seasons, the annual $P_q(q)$ (Figure 7.22e) was able to reproduce the overall shape of the observed cdf quite well, with a MAE of 0.1 cm/d in this case (12.8% of the mean discharge). Nevertheless, the model underestimated the probability of low streamflows. At the annual timescale, the streamflow regime of Poverty Creek had an erratic behaviour with $CV_q > 1$ and high slopes of P_q especially for low values of q.

In Poverty Creek, the parameter b that modulates the active length vs. discharge relationship is equal to 1.09, leading to an almost linear relationship between these variables. Relatively high values of b imply a high dynamicity of the river network which is consistent with the observed seasonal variations of the flowing length in this case. In addition, the relatively high value of R^2 (0.77), indicates that the power-law model provides a good representation of the observed L vs q relationship.

Similarly to the annual P_q, the analytical cdf of the active length at the annual timescale was calculated as a weighed average of the seasonal curves. The annual

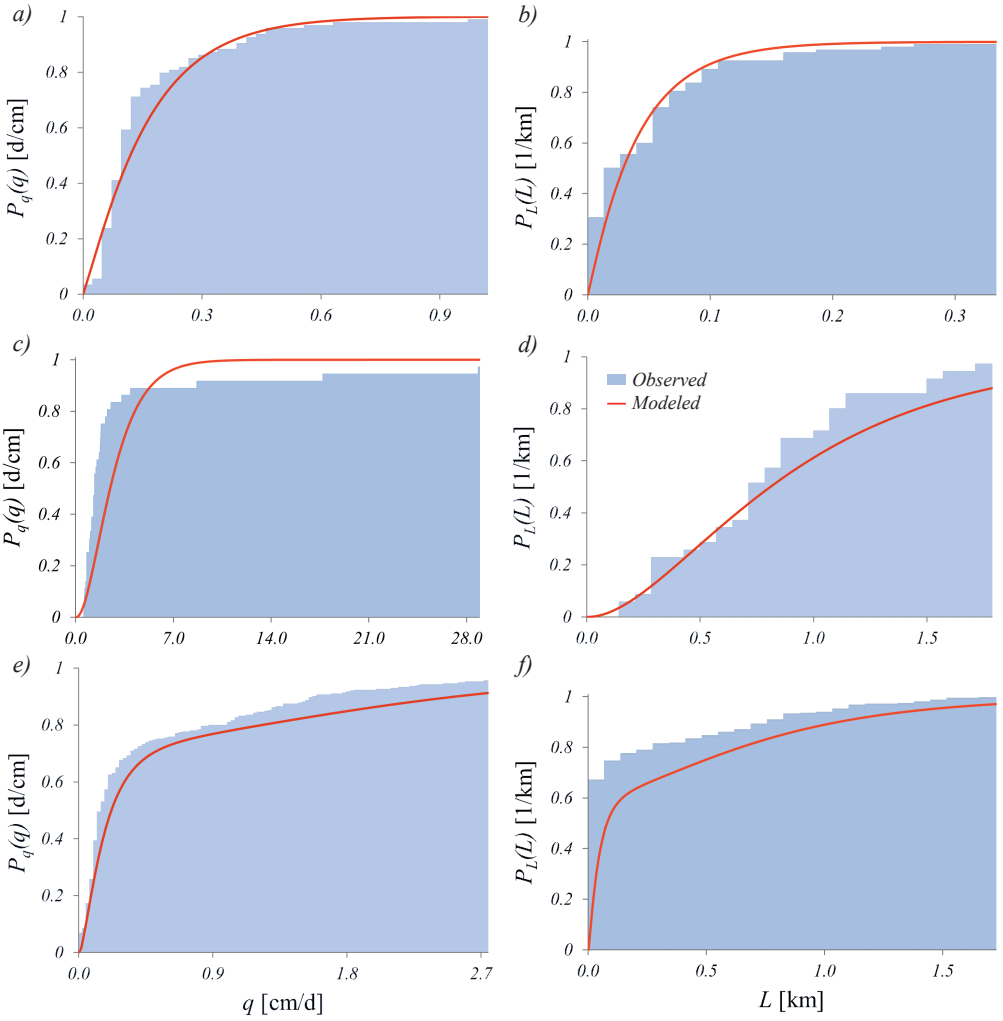

Figure 7.22: Cumulative distribution functions of streamflow ($P_q(q)$, left plots) and active length ($P_L(L)$, right plots) for the Poverty site. Panels a) and b) refer to the summer season, panels c) and d) to the spring season, while panels e) and f) refer to the whole year.

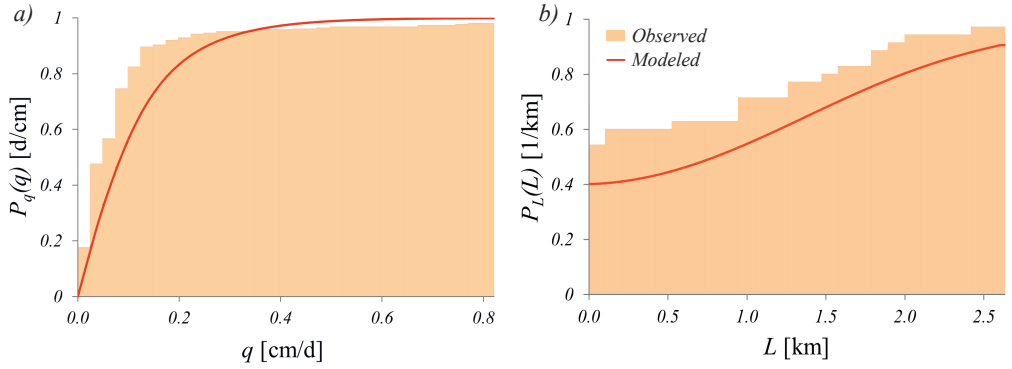

Figure 7.23: Cumulative distribution functions of streamflow ($P_q(q)$, panel a) and active length ($P_L(L)$, panel b) for the Turbolo site.

$P_L(L)$ underestimated the observed cumulative distribution of wet length, particularly for $L < 1\,km$. The shape of the modeled cdf indicates that a high probability is associated to the almost complete network shrinking. Likewise, a wide range of active lengths was associated to the highest non-exceedance probabilities. The MAE, which is equal to 0.138 km (38.5% of the mean), indicates discrepancies between the modeled and the observed active length cdfs. This performance was still deemed acceptable, as the overall shape of the cdf was captured by the model (Fig. 7.22f). The shape of annual active length distribution was influenced by the seasonality of the climate in the study site. During the spring (Figure 7.22d) and the winter (SI), high values of the active stream length were observed, but no particular preferential states were observed in the network configuration. On the other hand, the summer (Figure 7.22b) - similarly to the autumn (SI) - was characterized by dry conditions with active lengths which were often close to zero (with P_L approaching 1 for $L < 0.3\,km$).

In the Turbolo catchment, owing to the strong seasonality in the underlying hydroclimatic conditions, the parameters α, λ and k all varied significantly across the year. The mean effective rainfall depth was slightly lower than $1\,cm/d$ in all seasons but the spring, during which $\alpha = 0.52\,cm/d$. The effective rainfall frequencies, instead, ranged from $0.04\,d^{-1}$ during the summer to $0.20\,d^{-1}$ during the winter and the spring. The mean recession rate followed a similar trend, with values that were in the range ($0.06\,d^{-1} - 0.13\,d^{-1}$). The annual $P_q(q)$, calculated as a weighted average of the seasonal curves, slightly underestimated the probability of low streamflows but it was able to properly reproduce the shape of the observed cdf of q (Fig. 7.23a). The MAE of the streamflow model is equal $0.030\,cm/d$ (17.8% of the mean) in this case.

The annual cdf was a concave function of q. This circumstance is related to the high slope of the summer FDC in correspondence of $q \to 0$. The annual cdf also mirrored the pronounced seasonality of the climate in the whole Crati region. Therein, the summer season was characterized by high temperature and high evapotranspiration rates, which led to a low mean discharge with pronounced streamflow variations. Instead, the other seasons of the year were featured by more frequent rainfall events

which induced a streamflow regime characterized by more abundant water resources and reduced hydrologic fluctuations.

The scaling exponent b is equal to 0.50 in the Turbolo, a value which lies in the literature range. The low value of R^2 ($R^2 = 0.21$) is possibly due to the fact that discharge measurements were only available at the outlet of much larger catchment.

The annual modeled $P_L(L)$ is reported in Fig. 7.23b, where a comparison with the corresponding observed distribution is shown. The modeled $P_L(L)$ generally underestimated the probabilities associated with all the observed active lengths but it properly replicated the shape of the observed cdf. The MAE, calculated as the mean difference between the modeled and the observed active lengths associated to the 0.2, 0.4, 0.6, and 0.8 quantiles of the distribution, is equal to $0.329\,km$ (49.0% of the mean). The MAE for the Turbolo indicates a systematic underestimation of P_L throughout the L domain.

7.9.2 Streamflow and active length regimes

Figure 7.24 compares the shape of the FDC and the SLDC in the three study catchments, using both empirical data (left panels) and the corresponding analytical curves (right panels). The Figure emphasizes that, by and large, the analytical models are able to capture the observed relationship between the discharge and the active length regime across all the case studies.

The Valfredda river (Figure 7.24a and 7.24b) is characterized by a persistent flow regime and a perennial active length regime. In fact, the flow duration curve displays a smooth shape and a relatively flat slope covering the full range of durations from 0 to 1. The stream length duration curve has a smaller slope of the FDC, and displays a clear inflection point which makes the $SLDC$ strictly positive for all the durations between 0 and 1. In this case, the ratio λ/k ($= 2.8$) is larger than 1 while $b < 1$. This implies that the Valfredda catchment, based on the theoretical regime classification proposed in section 5.2.4, has a “class F" behaviour. Accordingly, the theoretical and observed coefficients of variation of streamflows and wet lengths, turned out to be lower than 1, with $CV_L < CV_q < 1$. This behaviour is mainly induced by the presence of few permanent groundwater springs feeding some perennial channels of the stream network.

Regarding Poverty Creek, the FDC and the SLDC both display pronounced seasonality (SI). In the spring (Figure 7.24c), the ratio λ/k is equal to 2.29, thereby suggesting a persistent flow regime, as mirrored by the knee-shaped FDC. As the parameter b is equal to 1.09, the ratio $\lambda/(kb)$ is also larger than 1. Therefore, the active length regime can be classified as a perennial regime, as reflected by the shape of the SLDC, which leads to positive values of $L/\langle L\rangle$ for $D \to 1$. Overall, the behaviour during the spring belongs to the “class E". However, during the summer, $\lambda/k = 1.21$ and $\lambda/(k\,b) = 1.11$. Under these circumstances, ($\lambda/k \simeq 1$, $b \simeq 1$, $\lambda/k > b$ and $\lambda/k < 0.4114\,b^2 + 0.7168\,b$) an ephemeral de facto active length regime and an intermediate flow regime are observed. Thus, during the summer, the behaviour of

Poverty Creek belongs to the “class D".

The normalized annual flow duration curve (Fig. 7.24g and 7.24h) is quite steep and concave within the whole domain (0,1). Similarly, also the annual SLDC has a steep shape and it clearly approaches the x-axis at durations lower than 1, indicating an ephemeral active length regime. On an annual basis CV_q and CV_L are both larger than 1, indicating a pronounced variability of q and L in time, with a behaviour in between “class A" and “class B" ($b \approx 1$). This is mostly related to the high seasonality of discharge and active length regimes. In the Poverty Creek the shape of the seasonal SLDCs resembles that of the corresponding FDCs, as $b \simeq 1$.

In the Turbolo, the streamflow variability is enhanced ($CV_q > 1$) and an erratic flow regime is observed, which is reflected by the convex shape of the FDC (Fig. 7.24i and 7.24j). Similarly, also the temporal variations of the active length are pronounced ($CV_L > 1$). The annual SLDC intersects the x-axis in a point with a duration lower than 1, suggesting an ephemeral active length regime. Overall, the Turbolo shows a “class A" behaviour. The ephemeral nature of the active length regime in the Turbolo catchment is not surprising in the light of the climate of the study site. In several cases the river network has been detected as completely dry, with active length values equal to 0. This is in accordance with the Mediterranean climate, which is characterized by high temperature and prolonged droughts during the whole summer, which leads to a seasonal dry-down of the drainage network.

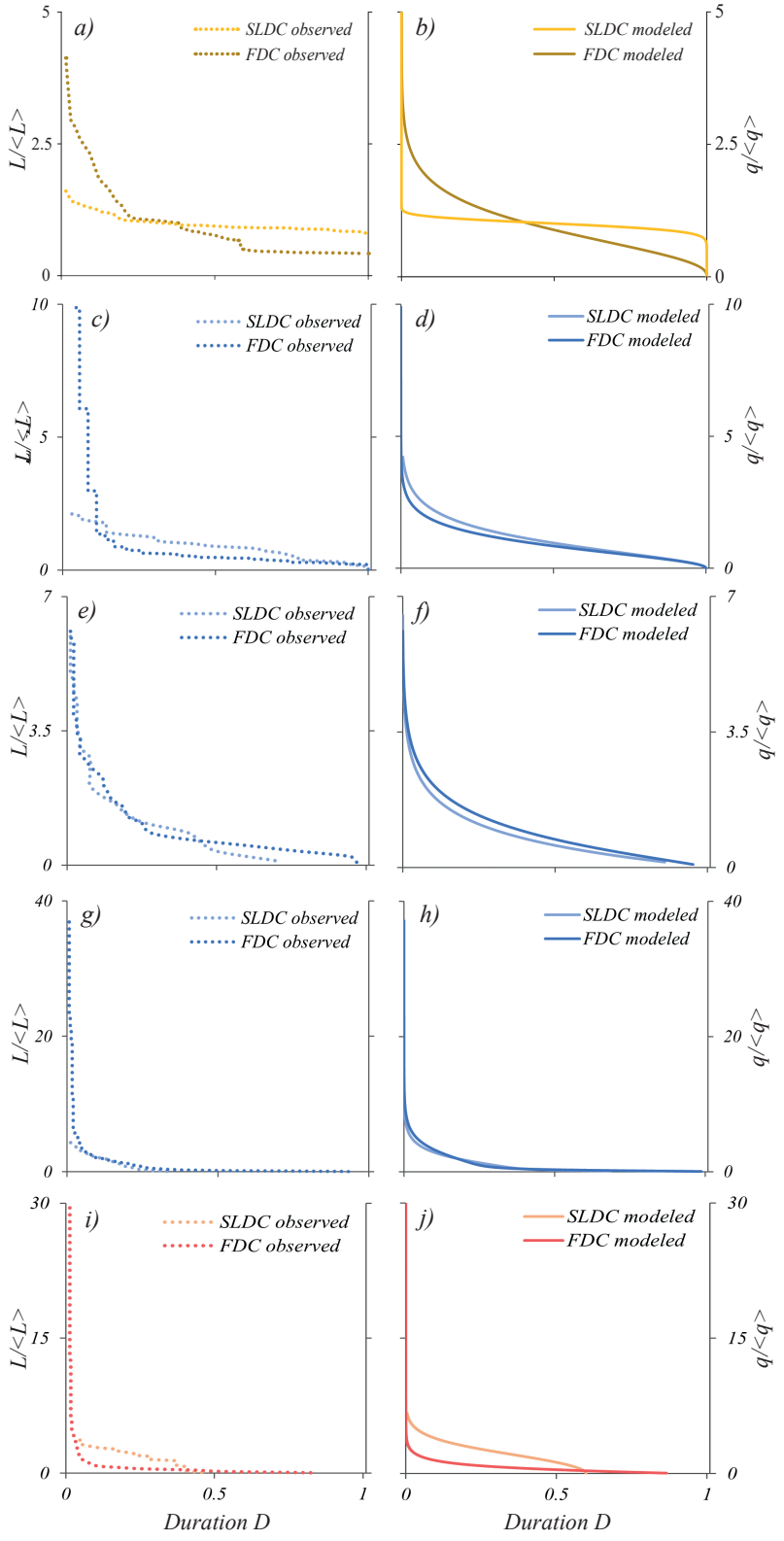

Figure 7.24: FDCs and the SLDCs using empirical data (left panels) and the corresponding analytical curves (right panels) for the three study catchments. Panels a) and b) refer to the whole study period in the Valfredda site. Panels c) to h) refer to different periods in the Poverty creek: spring (c, d), summer (e, f) and the whole year (g, h). Panels i) and j) show the annual curves for the Turbolo creek. All plots refer to dimensionless quantities ($L^* = L/\langle L \rangle$ and $q^* = q/\langle q \rangle$).

7.10 An empirical model for reconstructing the spatio-temporal dynamics of the active channel network

To show the potential of the empirical model described in section 6.1, the model was used to reproduce the change in the active network of the Rio Valfredda during a period of 5 months (from July 1^{st} to December 6^{th}, 2018), on the basis of 9 empirical surveys performed in the same period. A video showing the continuous spatio-temporal dynamics can be found in Durighetto et al. 2021. Instead, Figure 7.25 presents a sequence of snapshots taken from the simulation in correspondence of the most intense rainfall event of the whole study period. Although the results reported here only refer to one study case, analogous results can be obtained for all the experimental sites presented in Chapter 3, as this simulation is mainly based on the hierarchical activation scheme that holds true in all the studied sites (see Section 7.4).

The video highlights that different modes of network expansion and contraction concur to determine the observed changes in the active network of the Valfredda catchment. During stream expansion, some branches lengthen upstream while other expand downstream, either connecting to the outlet or remaining disconnected from the main river. During network contraction, disconnections frequently appear along many tributaries, especially in the lower-east part of the catchment where the limited soil permeability supports a flashy activity of the streams, thus enhancing flow intermittency. Furthermore, network expansion is much faster than the subsequent contraction, mirroring the positive skewness of the hydrograph (e.g. Botter et al. 2003). As an example, during the huge rain event that took place in late October, the network lengthened from approximately 7 to 17 km in only 3 days, while more than one month was necessary to go back to the average length of 8 km. In particular, Figure 7.25a displays the modeled active network during its expansion on the 27^{th} of October, when 50 mm of rainfall occurred after two almost completely dry months. As the network expands, disconnected active stretches appear in the northern and south-eastern part of the catchment, expanding downstream. In the middle part of the network, instead, the already connected active branches lengthen upstream. The active network reached its maximum extension on October 29, after 3 days of continuous, heavy rainfall for a total of about 265 mm (Figure 7.25b). In this configuration, all parts of the network are completely active and connected to the outlet, with the only exception being some smaller branches that are geometrically disconnected from the rest of the streams. As the network starts to contract in the subsequent days (Figure 7.25c), the most flashy branches dry down and disconnections reappear along the network. Overall, the simulation emphasizes the spatial heterogeneity of network dynamics, highlighting once more the importance of capturing high-frequency dynamics of the active network. The continuous nature of the modeling, both in space and time, facilitates the identification of many important features of network dynamics which are much harder to catch from a sequence of static maps.

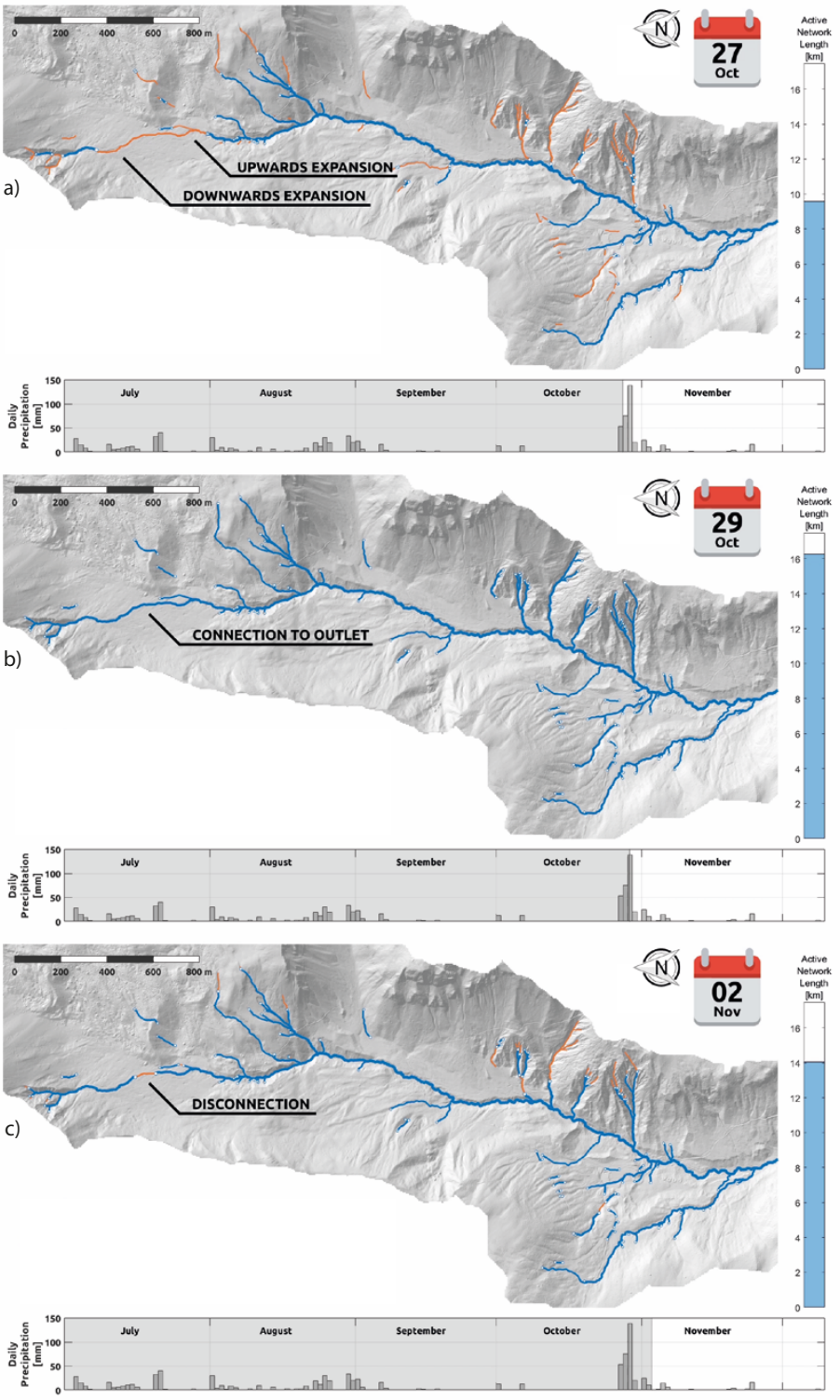

Figure 7.25: Maps of the modeled active stream network of the Valfredda catchment on the 27th of October (a), 29th of October (b) and 02th of November 2018 (c). Active stretches are blue, inactive are orange. White dots correspond to locations where surface flow starts or stops.

7.11 A Bayesian hierarchical model for space-time channel network dynamics

The model presented in section 6.2 allows the coupled simulation of streamflow and stream network dynamics, enabling the stochastic simulation of the spatio-temporal dynamics of the active stream network under a broad range of climatic and morphological conditions while requiring a small number of parameters and a limited computational effort. The model was used to explore spatiotemporal dynamics of the active network in synthetic streams subjected to contrasting flow regimes and various spatial patterns of flow persistency. The generated dynamical active networks were then used as a basis for the D-SPOM metapopulation model (see section 6.3), to provide an assessment of the impact of the hydrological network dynamics on species persistence under different setting.

The model presented in section 6.2 was applied to 9 different climatic and physiographic scenarios to illustrate its capability in reproducing network dynamics under different climatic and geomorphological settings. All the results related to the active length are shown in terms of relative length, defined as $L(t)/L_g$ were L_g is the geomorphic length (i.e. the maximum potential length of the active network), to emphasize the fact that the spatial scale is not relevant for the generation of stream dynamics through the presented model.

The simulation results relative to the *W2* scenario are reported in Figure 7.26. The timeseries of rainfall shows how the high frequency of precipitation in the wet climate ($\lambda = 0.37$) provides a regular water input on the catchment, often resulting in continuous precipitation events that last for multiple days. The stochasticity of the effective rainfall is directly reflected into the timeseries of streamflow, in which the positive increments dictated by precipitation are combined into a continuous signal by the linear recession rate. The timeseries of threshold $P^*(t)$, obtained with eq. (6.4), shows an analogous, albeit reversed, behaviour. In particular, the stochastic rainfall events that increase $Q(t)$ are reflected into reductions of $P^*(t)$, with consequent expansions of the active network. As per equation (6.4), CDF_Q modulates the transformation of $Q(t)$ into $P^*(t)$, introducing a non-linear relation between these two signals. As Figure 7.26 shows, in fact, for the *W2* scenario the variability of the highest flows ($Q(t) > 7.5mm/d$) corresponds to weak variations of $P^*(t)$. Instead, streamflow variations in the range between 2.5 and $5mm/d$ are amplified in $P^*(t)$, suggesting that the active network may be most sensitive for average flow conditions ($\bar{Q} = 4mm/d$ for scenario *W2*). Panels d) to g) of Figure 7.26 show a sequence of snapshots of the simulated active network, while the full dynamics can be observed as a video in the SI. The maximum extension of the network (panel d) is obtained at day 16 of the simulation, after a series of intense rain events that result in a huge increase of Q. During periods with weak rainfalls (e.g. from day 45 to 60) or in the absence of precipitation (e.g. in the period between day 111 and 123), the streamflow gradually decreases, with a consequent progressive contraction of the active network (as shown in panels e and f of Figure 7.26), reaching its most contracted configuration only after the longest dry spells

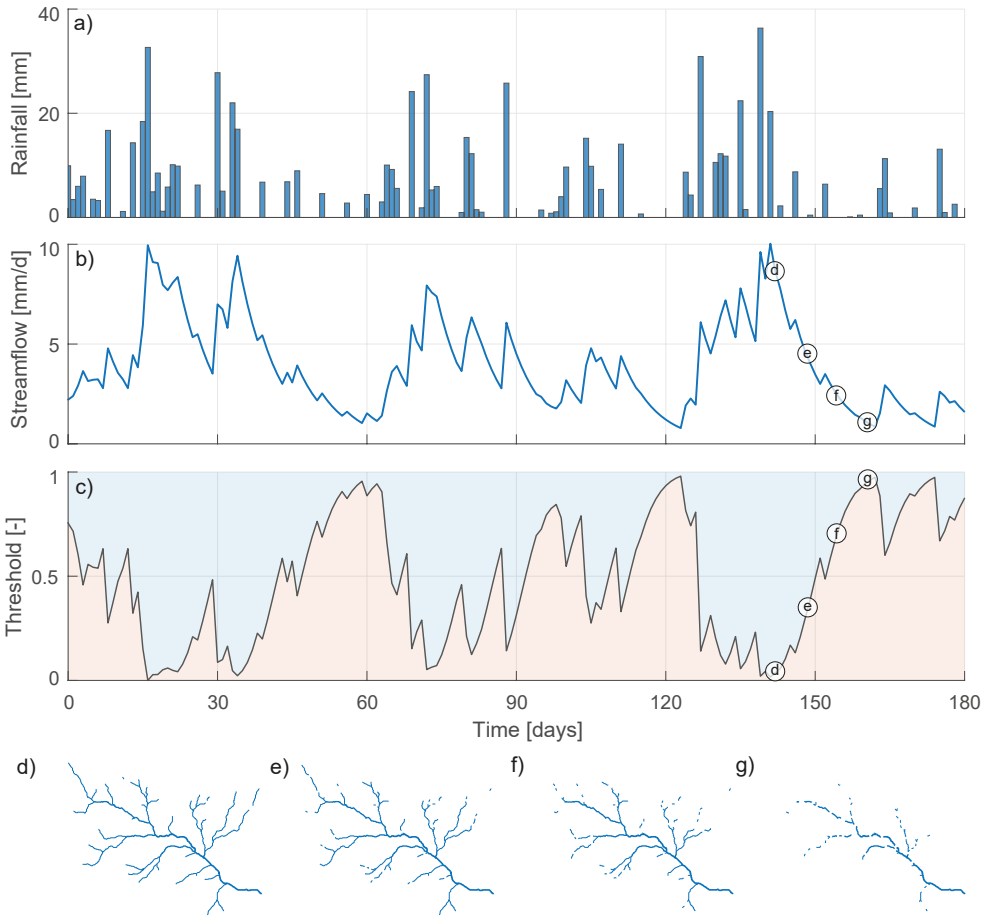

Figure 7.26: Simulation results for the *W2* scenario. Panels a), b) and c) show the timeseries of rainfall, streamflow $Q(t)$ and persistency threshold $P^*(t)$. Panels d) to g) report the simulated maps of the active network on the 4 different time steps indicated in panel c).

(panel g).

The difference dynamics that the network experiences under each scenario are explored by comparing the corresponding maps of local persistency (Figure 7.27), generated timeseries of Q and L (Figures 7.28 and 7.29), and different sequences of possible configurations that each network experiences during expansion (Figures 7.30, 7.31, 7.32).

The generated maps of local persistency for the 6 scenarios related to the wet and dry climates are reported in Figure 7.27. All the dry scenarios (*D1, D2, D3*) share the same mean persistency $\bar{P} = 0.20$, and therefore the same statistical distribution of P_i, with the only difference being the related spatial patterns. The same is true also for the three wet scenarios (*W1, W2, W3*), which all share a mean persistency $\bar{P}$ of 0.74. As one would expect, randomly assigning persistencies (*D1, W1*) generates maps where adjacent nodes might have very different values P_i, while persistencies assigned via the underlying contributing area (*D3, W3*) are monotonically increasing in the downstream direction. Using the TWI as the key criterion for assigning the local persistencies (*D2, W2*), instead, originates maps with P_i that on average

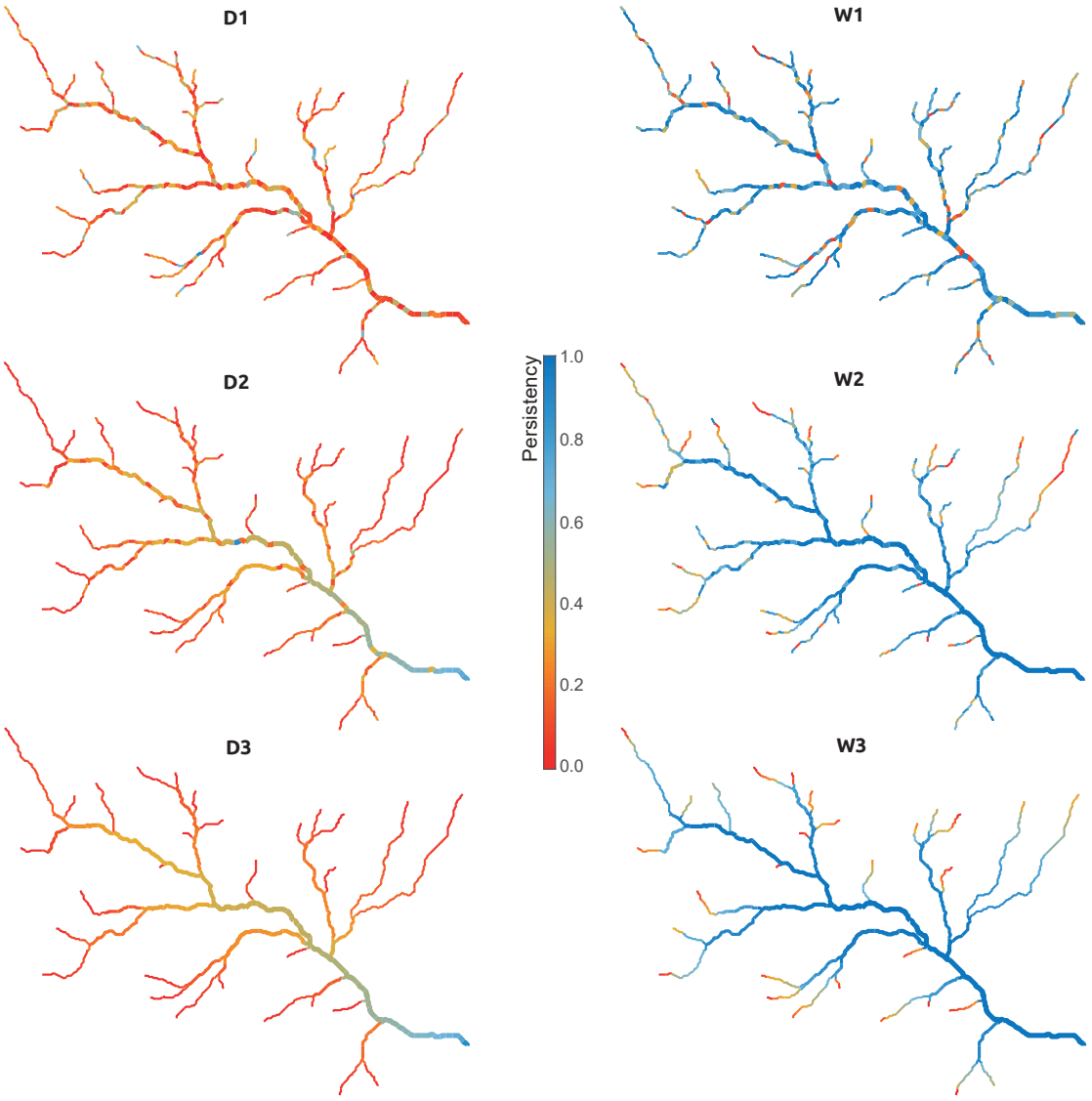

Figure 7.27: Maps of local persistency for the 6 simulated scenarios.

increases in the downstream direction with some exceptions.

An example timeseries of streamflows for the dry climate is depicted in Figure 7.28a. Under this climate, the recession rate is higher than the mean frequency of flow-producing rainfall events ($\lambda/k = 0.65$), resulting in an erratic streamflow regime. Consequently, streamflow dynamics are characterized by spiky flow pulses separated by prolonged intervals with very low flows. The active length timeseries, shown in Figure 7.28b, inherits some of the properties of the $Q(t)$, with some key differences. The faster recessions exhibited by active length dynamics as compared to the corresponding streamflows generate long spells during which the stream network is almost completely dry. Nonetheless, a remarkable fraction of the network is activated by a few moderate to high flow events. This produces a significant variability in the active length ($CV_L = 1.35$). The flow duration curve (FDC) depicted in Figure 7.28c is convex and quite steep, owing to the high probability associated to very low flows. The FDC, being the inverse function of CDF_Q, shows how $Q(t)$ is transformed into $P^*(t)$, modulating the expansion and contraction of the active network. This sug-

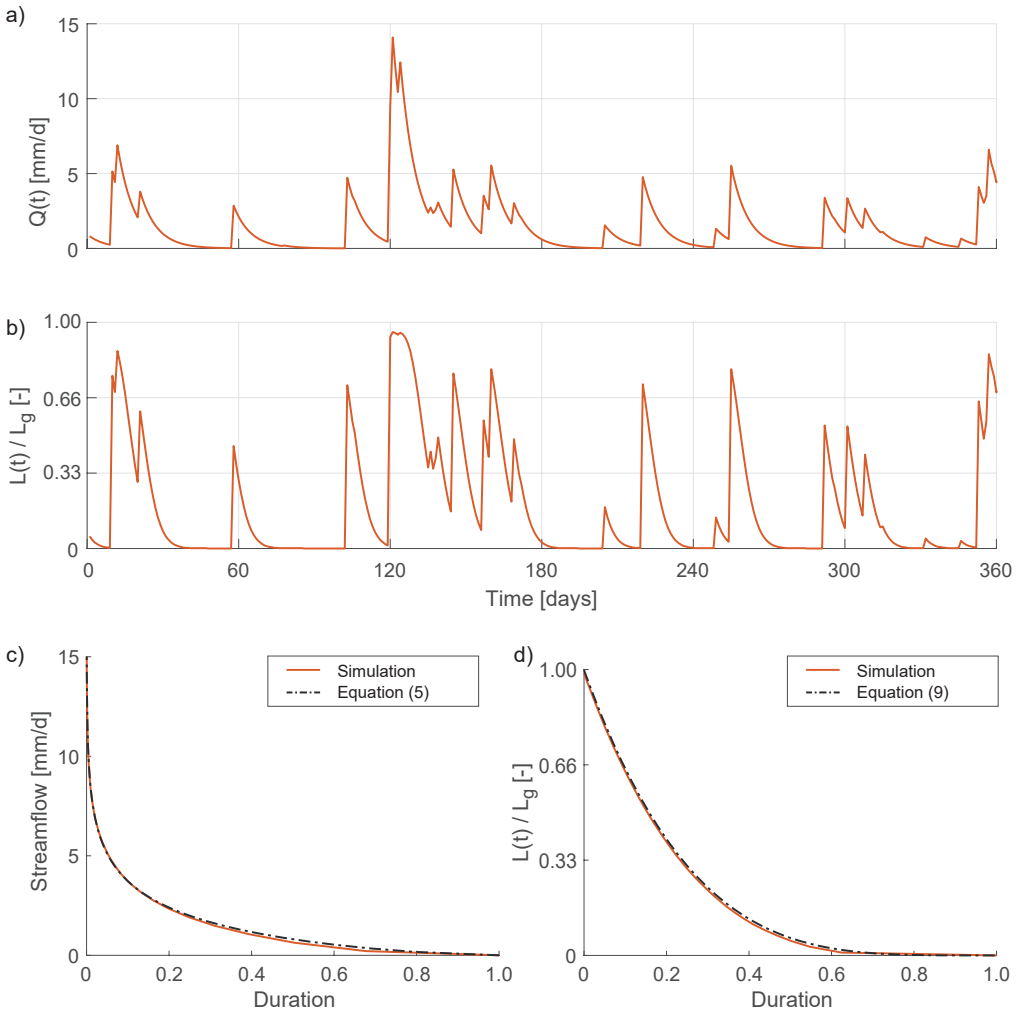

Figure 7.28: Time series of simulated streamflow (a) and active length (b) for the scenarios with dry climate. Panels c) and d) show the corresponding flow and stream length duration curves.

gests that, in the scenarios with dry climate, $P^*(t)$ is more sensitive to low flows, for which the FDC is flatter. The SLDC (Figure 7.28d) displays similar characteristics, and approaches the x-axis for a duration of about 0.65. Thus, the network is almost completely dry for about 1/3 of the simulation.

Figure 7.29 shows the simulated timeseries of streamflow and active length for the wet climate, as well as the corresponding flow and stream length duration curves. In this case the mean interarrival between effective rainfall events is smaller than the recession rate ($\lambda/k = 2.45$), leading to a persistent flow regime with streamflows that are weakly variable around the mean. As a consequence, most of the stream network is active for significant periods of time, with sensible reductions of $L(t)$ only during the longest recession periods. The active length timeseries shows how active length recessions tend to be concave, with the $L(t)$ staying quite constant for a few days before starting the real contraction process. This tends to reduce active length variability (with respect to streamflows), resulting in a coefficient of variation CV_L equal to 0.28. The FDC is knee-shaped, suggesting that the most probable

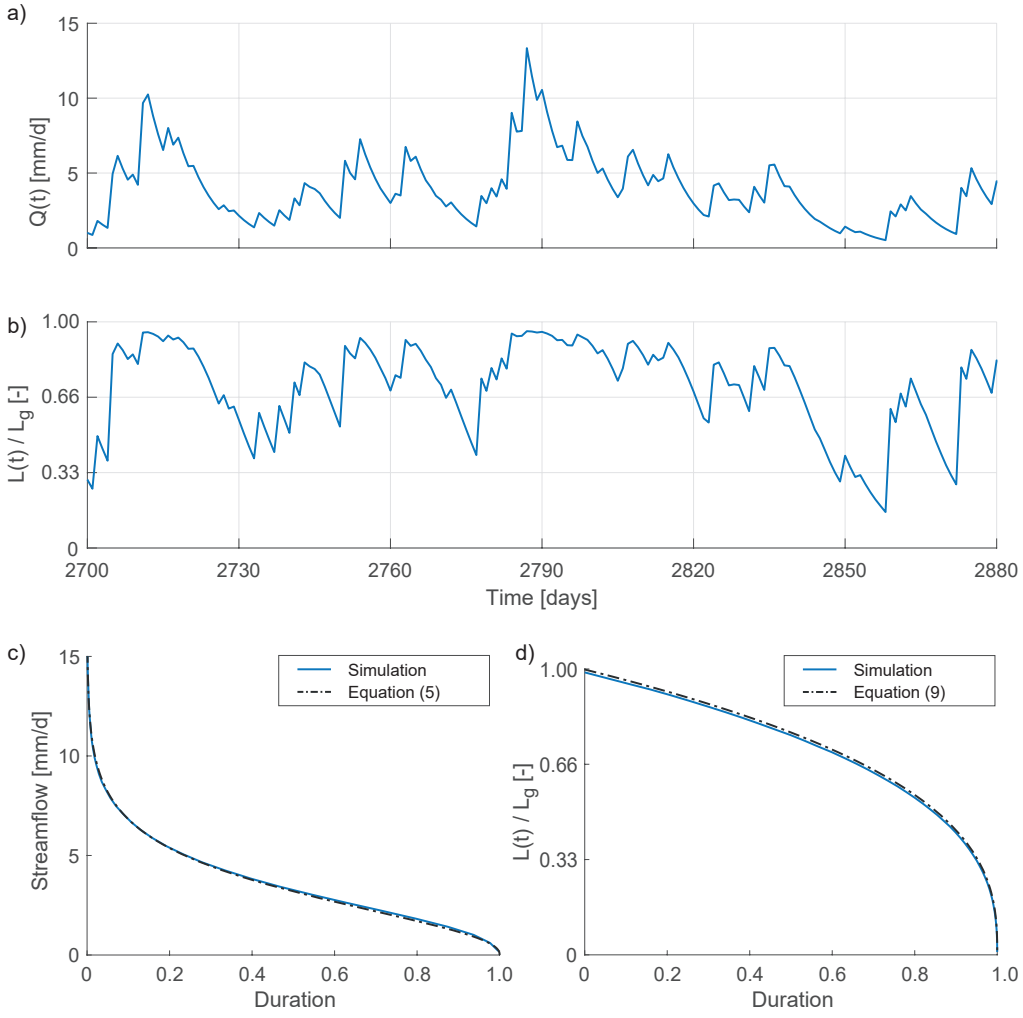

Figure 7.29: Time series of simulated streamflow (a) and active length (b) for the wet climate scenarios. Panels c) and d) show the corresponding flow and stream length duration curves.

streamflow value is greater than zero. The SLDC is concave and much flatter than the one observed under the erratic regime, further confirming the reduced variability of the active length in this case. Furthermore, the SLDC approaches $D = 1$ for a relative length of about 0.2, revealing that in this case a significant portion of the network remains permanently active.

Thanks to the hierarchical scheme, during network expansion (contraction) nodes are activated (deactivated) following a fixed order prescribed by the local persistency. As a result, for a given active length L (or its duration $D(L)$) only one network configuration, intended as the set of nodes that are active, is possible. Figure 7.30 shows two sets of network configurations associated to durations ranging from 0.05 to 0.95, for scenarios *W1* and *D1*. It is worth noting how $D(L)$ can also be interpreted as the persistency threshold P^* determining the status of the nodes. Therefore, as $P^*(t)$ experiences continuous increasing/decreasing cycles as a response to the stochastic climatic input, the corresponding expansion/contraction cycles of the active network consist of a continuous sequence of the configurations reported in the figure. The random assignment of local persistency along the network results in a patchy activation of network segments, generating a multitude of disconnections that are gradually removed as the network approaches its completely expanded configuration. Furthermore, it is evident how under the dry climate (*D1*) owing to the erratic flow regime most parts of the network are activated only sporadically, with the active network associated to a relative length of 50% having a duration $D < 0.2$. The same network configuration, on the contrary, has a duration $D > 0.8$ under the wet scenario (*W1*). In this case, 93% of the network is active with duration $D = 0.2$. Nonetheless, multiple disconnections remain present throughout all the possible network configurations (with the only exception being the completely expanded network). As Figure 7.32 shows, such disconnections are not present in the *D3* and *W3* scenarios, where P_i follows the order of increasing contributing area. In this case, the network always expands from the outlet upstream, ensuring the continuity of its active portion. When TWI is used as criterion for the assignment of P_i (scenarios *D2* and *W2* shown in Figure 7.31), the spatial pattern of flowing network combines the characteristics described above for the other scenarios. In this case, in fact, network expansion can be associated with a double action: the activation of new reaches in the upper part, usually disconnected from the rest of the active nodes, is accompanied by the removal of disconnections in the lowest part of the network. As a consequence, the network configuration at any given time is composed of a main part, comprising most of the active length and usually connected to the outlet, and a number of small disconnected reaches in the uppermost branches.

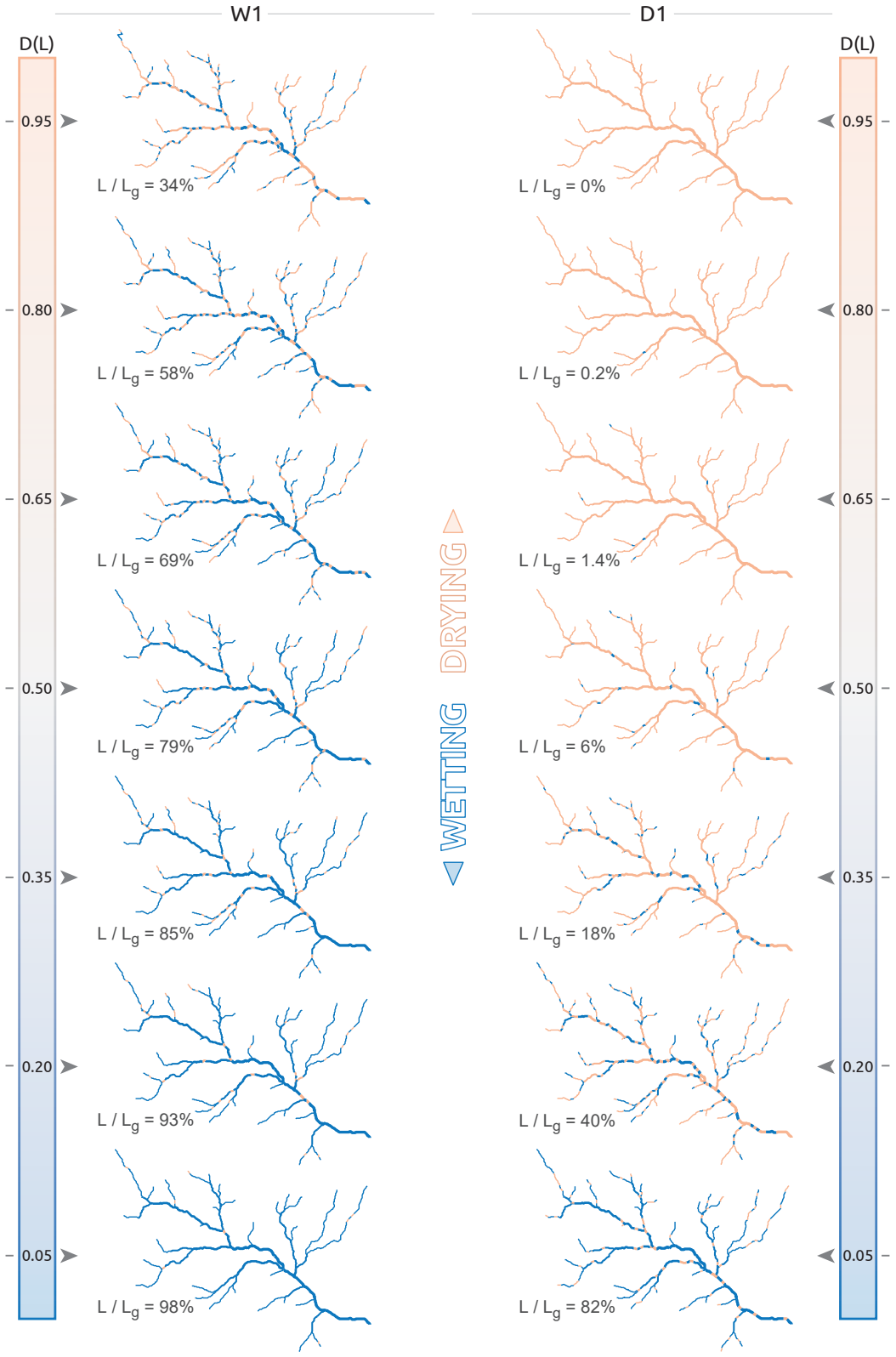

Figure 7.30: Snapshots of the active network (in blue) for scenarios D1 and W1, i.e. dry and wet climates and random assignment of local persistency, with the corresponding active length and its duration.

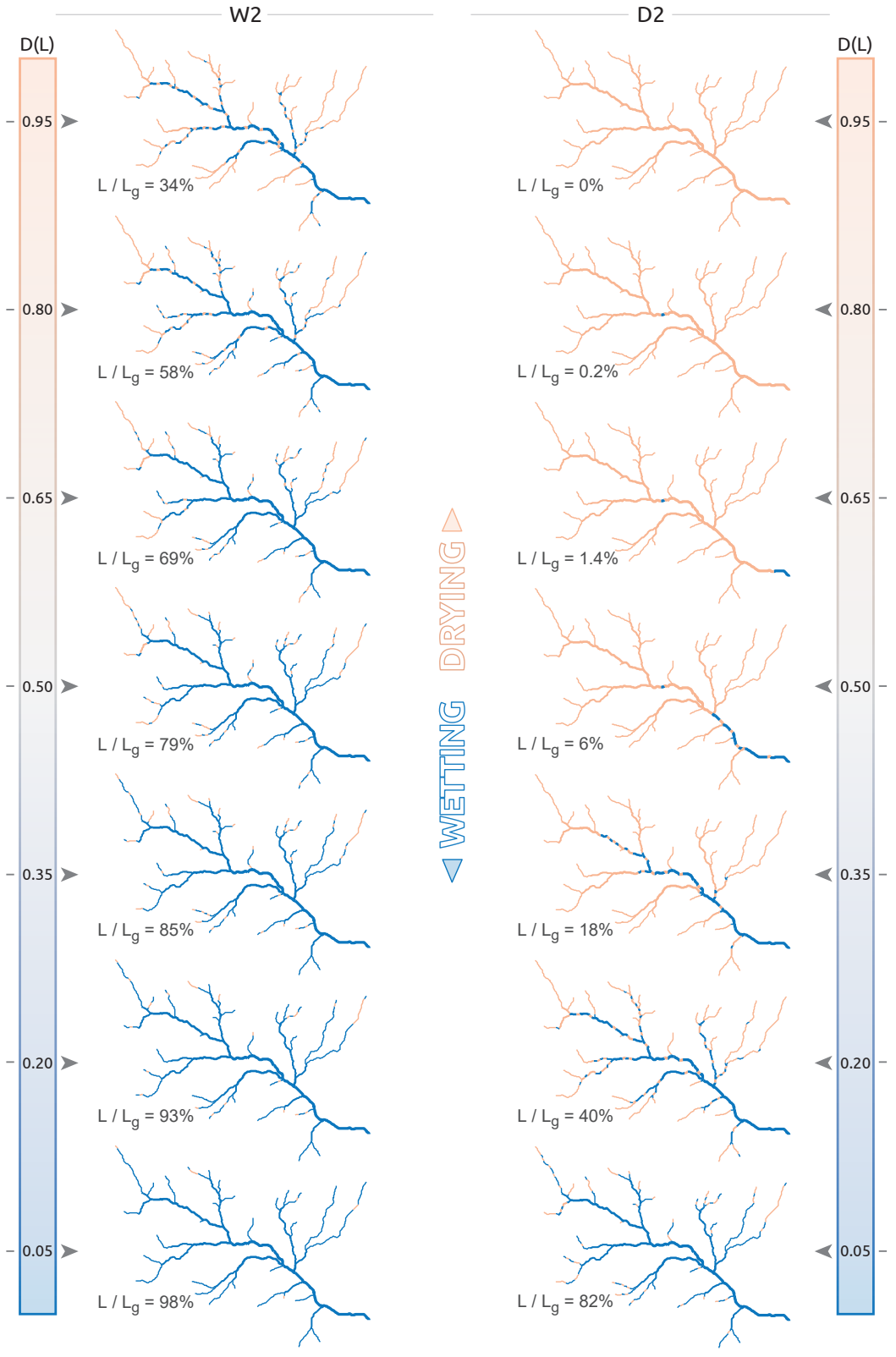

Figure 7.31: Snapshots of the active network (in blue) for scenarios D2 and W2, i.e. with local persistencies assigned by TWI, with the corresponding active length and its duration.

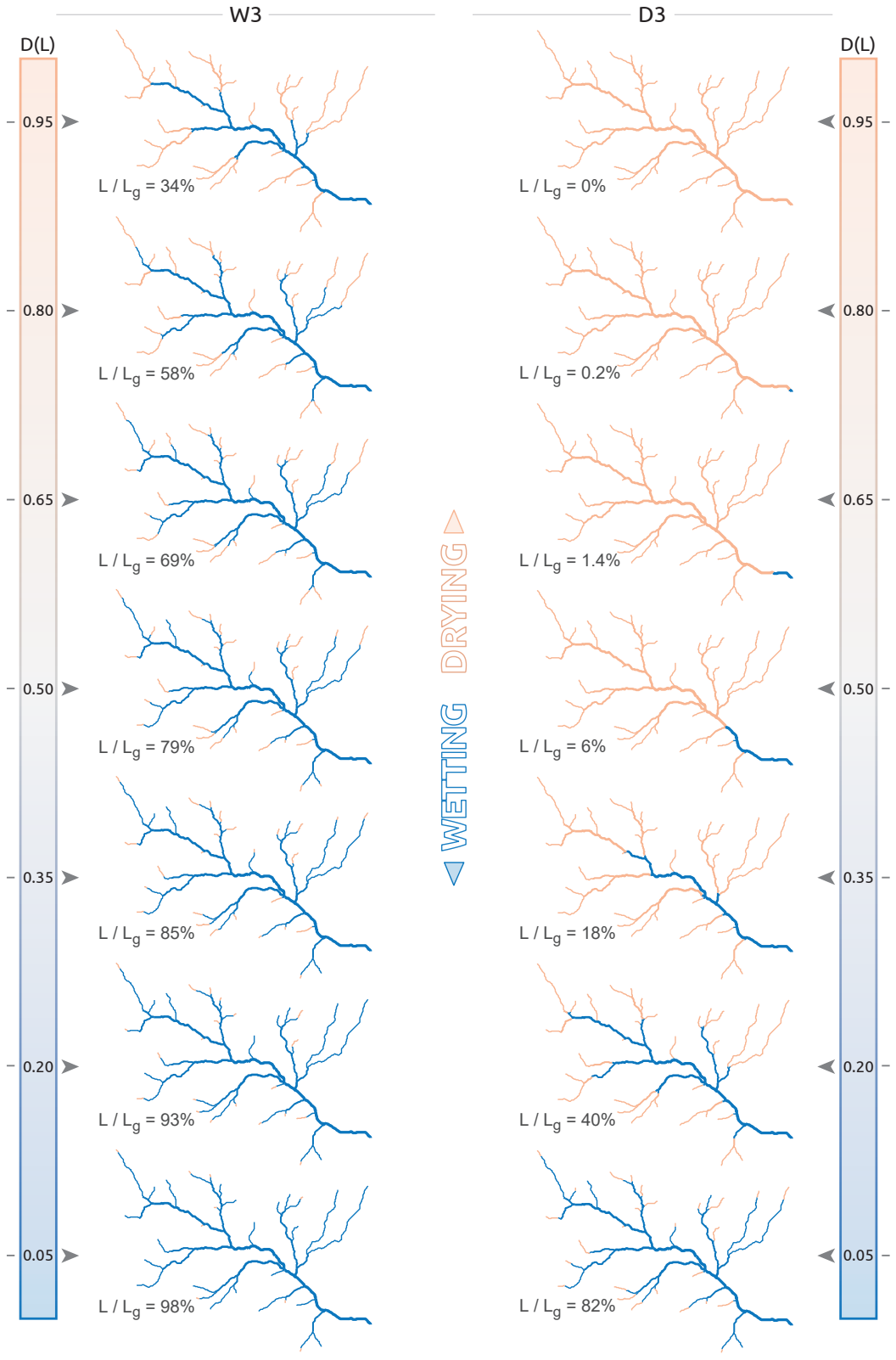

Figure 7.32: Snapshots of the active network (in blue) for scenarios ED3 and W3, i.e. with local persistencies assigned by contributing area, with the corresponding active length and its duration.

The generated time series of active network provide great examples of the main hydrological features of temporary streams in relation to the underlying properties of the climate within the catchment. But the importance of temporary streams goes far beyond hydrology, with important ecological implications related to, as an example, nutrient cycling and species occupancy. This sections provides the results of the application of the metapopulation model described in Section 6.3, which builds upon the simulated networks discussed earlier, with the aim of providing key information on the ecological significance of stream expansion and retraction and unveiling how river network dynamics may affect metapopulation occupancy.

Figure 7.33 displays the time series of network occupancy (i.e. the fraction of network length that is occupied by the target species at any given time) for the 9 different scenarios presented earlier, which combine erratic, intermediate and persistent flow regimes with three different spatial configurations of local persistency (i.e. by contributing area, TWI, or random). Furthermore, the metapopulation dynamics for each scenario are compared with the ones of an equivalent, average static network. The results show that dynamic networks are always associated with a lower mean occupancy than the corresponding static networks. A probable reason for this behaviour is that, in dynamic stream network almost all the nodes aren't always active, regardless of the underlying climate, and a certain amount of time is required

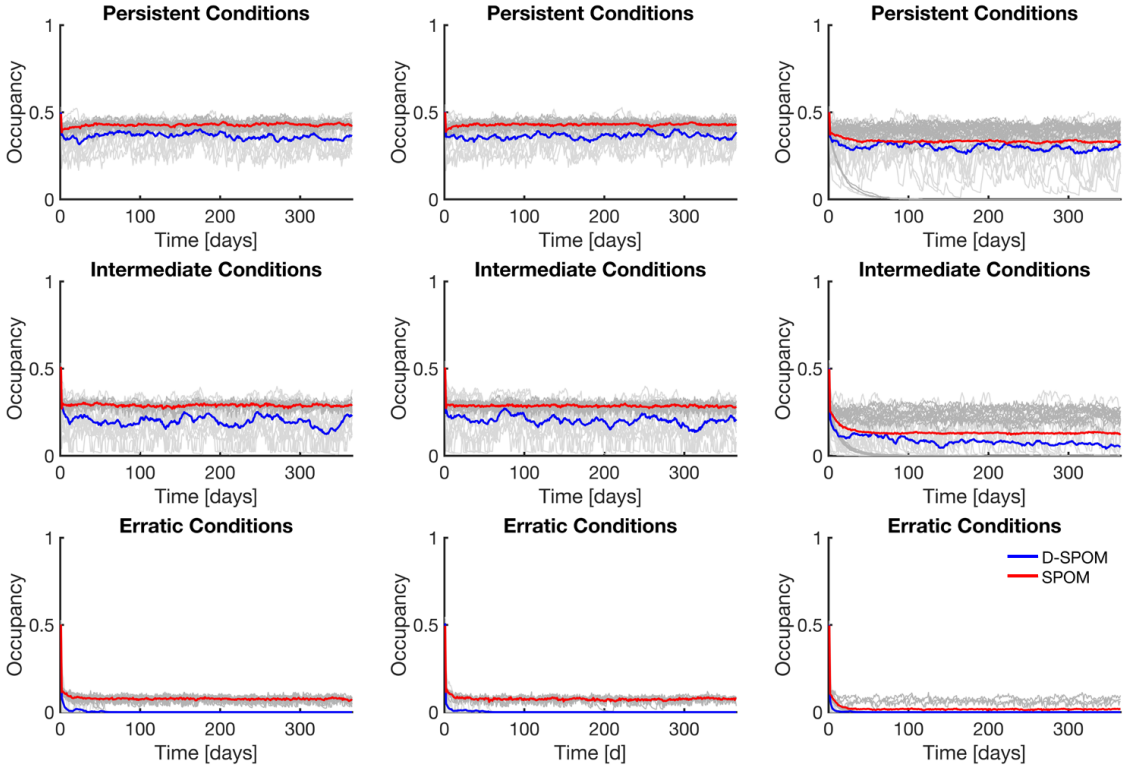

Figure 7.33: Comparison between the time series of river network occupancy computed using the D-SPOM (blue lines) and its static version (red lines). Each of these two type of time series represent the temporal mean over 50 single realizations. The comparison is repeated for persistent, intermediate, and erratic regimes for each of the three persistency scenarios: AD8, TWI and Random.

for the metapopulation to colonize a node once it is activated. The difference in mean occupancy is enhanced by erratic flow regimes, where network expansions are usually sporadic and flashy, and therefore a very limited number of nodes can sustain the metapopulation for prolonged time periods and act as a starting point for species dispersal when the network expands. The time-variability of occupancy on a dynamic stream network (blue lines in Figure 7.33) is, instead, always considerably higher than the cases with static networks (red lines). This could be attributed to the fact that in dynamic networks the active length (i.e. the available habitat for the target species) changes with time, and the activation/deactivation of different nodes is also reflected into different possibilities of dispersal of the metapopulation due to the insertion or removal of disconnections along the network. For this reason, the increase in variability is less pronounced in persistent regimes, where the network is usually more expanded and constituted of bigger intra-connected clusters, than in erratic ones where smaller habitat patches are continuously switched on and off and connected/disconnected from the rest of the network. In fact, the coefficient of variation of the network occupancy is 4 to 6 times higher in dynamic networks than in static ones, growing from 0.05 to 0.19 in persistent regimes and from 0.07 to 0.45 in intermediate ones. This type of comparison could not be done for the erratic regime because all the simulation reached extinction in the dynamic case, thus impeding the calculation of reliable coefficients of variation. The variability in network occupancy is also reflected into a higher probability of extinction in dynamic networks than in the static case. This extinction probability is enhanced in the case of random assignment of local persistency, which generates active networks that are very fragmented, thus reducing the possibilities of species dispersal and colonization of non-occupied nodes. Furthermore, this process is particularly important in erratic regimes, where the occasional activations of the network generate a lower mean occupancy in the static cases, and a high extinction probability in the dynamic ones. The synergistic effects of sporadic, flashy, expansions of the network with the presence of many disconnections that are removed only in the most expanded configurations of the network result into a probability of extinction of 100 % in a very short time period in the case of random local persistencies and erratic flow regimes.

The above results suggest that the ability of a temporary stream to sustain a target species is related to the size of the continuous parts of the network that are active at any given time. These continuous parts of active network, in fact, have two fundamental properties: a) they are active, and therefore the target species can occupy these habitat patches, and b) they are continuous, thus enabling the dispersal of the species between any couple of nodes belonging to the same continuous habitat patch. In graph theory, the size of the biggest continuous part of a network is described by the Minimum Spanning Tree (MST) length. The MST varies with time, as the active network expands and contracts; furthermore, it is influenced by the spatial patterns of local persistency that dictate which nodes are active for any possible length of the active network, and the location of the internal disconnections. Figure 7.34 shows the length of the MST as a function of the persistency threshold P^* for each of the 9 scenarios, showing how the length of the biggest continuous habitat patch varies as the network goes from completely expanded ($P^* = 0$) to contracted

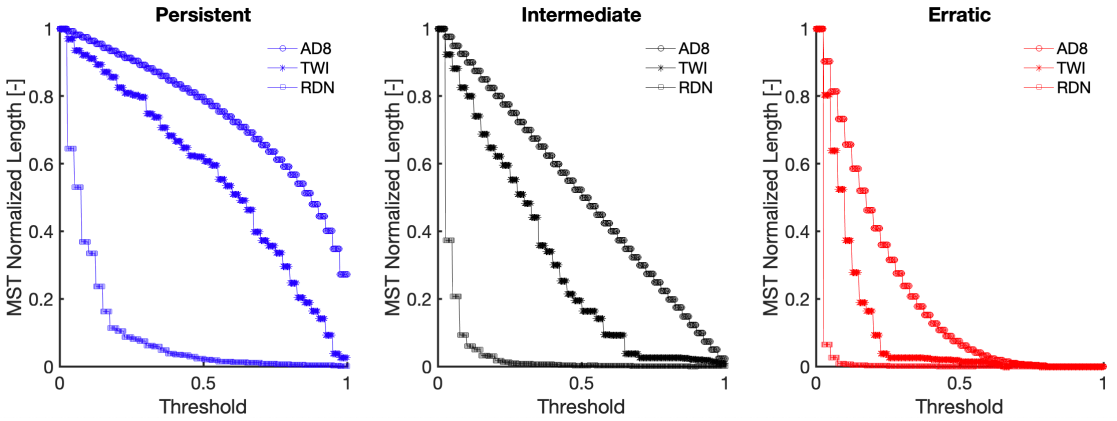

Figure 7.34: Sensitivity of the Normalized Minimum Spanning Tree length to the persistency threshold for persistent, intermediate, and erratic hydrological conditions. The computation is repeated for the three different scenarios of local persistency: AD8, TWI and Random.

($P^* = 1$). Furthermore, P^* can be interpreted as the fraction of time for which the corresponding active length L, or MST length, is equalled or exceeded (see Section 6.2.2). As no disconnections are present in the active network if the local persistencies are assigned by contributing area, the curves in Figure 7.34 relative to scenarios $W1$, $I1$ and $D1$ also correspond to the Length Duration Curves of all the networks that undergo the same flow regime. In the case of local persistency assigned by TWI (scenarios $W2$, $I2$, $D2$), some disconnections are introduced, and some smaller parts of the active network are not connected to the main one, impeding species dispersal and therefore reducing the network occupancy. Interestingly, in the case of non-correlated local persistencies (scenarios $W3$, $I3$, $D3$) the MST has a significant size for a very small duration even in the case of persistent flow regime, suggesting that the fragmentation of the active network significantly hinders the dispersal of the metapopulation, resulting in a lower mean occupancy and a higher extinction probability than in the corresponding scenarios with correlated local persistencies. As the flow regime changes from persistent to erratic, the curves in Figure 7.34 move to the left, showing how smaller and smaller durations are associated to network configurations with habitat patches of significant size.

8 Conclusions

In this study, the pulse of temporary streams was analyzed using a series of different empirical and theoretical tools, including novel monitoring techniques and new statistical indexes for the characterization of active length regimes. The thesis allowed the identification of the physical drivers of the temporal variability of the extent of the flowing network, and the development of new models for the spatio-temporal dynamics of the active network.

The study provides a new framework for a comprehensive analysis of temporary streams in a wide range of climatic and geologic settings. The framework is based on the discretization of the river network into nodes with a status that changes through time, and the characterization of each node through its local persistency. The pivotal finding of the thesis is the hierarchical activation scheme, according to which nodes are always activated a fixed order during network expansion, and deactivated in the opposite order during contraction. As a consequence, all the interactions between the states of different nodes are dictated by their local persistency, because a node can be activated only if all the more persistent nodes are already active, and the possible spatial configurations of the active network are solely defined by the spatial pattern of local persistency. This hierarchical behavior fostered most of the analytical and modeling results of this thesis. In fact, it enabled the derivation of analytical expressions for the main statistics of the active length (e.g. mean, variance and pdf) by disentangling the spatial and temporal dimensions of the dynamics of the active stream, and opened new ways for the spatiotemporal modeling of dynamic river networks.

Experimental activities. This study presents the results of a field campaign for the visual mapping of the stream networks in the Valfredda catchment, complementing the studied empirical dataset with data from a series of catchments located in Europe and USA. The data confirm previous results obtained in other climatic and geographic settings about the highly dynamical nature of river networks (e.g. Buttle et al. 2012; Datry et al. 2014; Godsey et al. 2014; Jensen et al. 2017). In particular, notwithstanding the humid climate typical of the Alps, more than 72 % of the stream network in the Valfredda catchment is dynamic, with an observed drainage density that varied, during about six months, between 1 and 2.5 km^{-1} depending on the underlying hydrological conditions. Under wet conditions, a considerable increase in the disconnected clusters and sources was also observed. This circumstance hints at the importance of mapping not only the streams directly connected to the outlet, but also all the channels that may be temporarily

or permanently disconnected. The portion of the network that was mapped in the Valfredda catchment as systematically inactive is 21%, suggesting that for many streams the time scale of wetting/drying cycles may be smaller than 48 hours (the typical lag between a precipitation event and the subsequent field survey in the field campaign). Moreover, the expansion/contraction cycles of the active drainage network are strongly controlled by event-scale hydrological dynamics, as indicated by the fact that the transition from the shortest to the longest recorded networks was observed in response to a single, albeit extreme, precipitation event.

Observed spatio-temporal patterns of stream network dynamics were efficiently summarized through persistency index maps, which indicate the percentage of time during which every stream of the network is active. These maps provide a useful graphical tool to characterize stream network dynamics and allow fair and objective comparisons across diverse river systems (e.g. Ovenden et al. 1980).

The use of ER sensors for the monitoring of active network dynamics was also tested. To this aim, a personalized version of the HOBO sensors previously proposed in the literature was used and modified to be suited for a deployment under different substrates and is deemed to be more accurate under unstable hydrodynamic conditions and during low-flow conditions. ER sensors provided precious information about high frequency space-time network dynamics in the study catchment during the fall of 2019; in particular, collected ER data were used to produce a video and a sequence of maps representing the dynamics of the active network with a sub-daily temporal resolution. The mean intensity of the ER signal, and the exceedance of a suitably selected intensity threshold were found to be highly correlated with the persistency of the network nodes estimated from visual surveys; this suggests that ER sensors signal provides statistically meaningful information on the hydrologic status of different nodes of the river network. The successful application of ER sensors under the heterogeneous environmental conditions found in the Valfredda catchment suggests the good potential and the flexibility of the tool for river network mapping. Likewise, the study highlighted the major shortcomings of this type of technology and the dependence of these shortcomings on the type of substrate: in steep rocky channels, the main problem is the sensor flushing during floods and the accumulation of sediments; in grassy regions, the major problems relate to water ponding and grazing of animals that might remove the sensors during the deployment. For the above reasons, the use of ER sensors for river network mapping needs to be quite intensively supervised. The high-frequency monitoring of flow rates and active stream lengths performed in this study allowed an in-depth analysis of the relationship between catchment discharge (Q) and active length (L). The data indicated the presence of some hysteresis in the $L - Q$ relation, both within individual events and across different events. The hysteresis observed in the Valfredda was attributed to the larger responsiveness of the active length to small rain events and to non-synchronous increase/decrease of L and Q within individual events.

It is fair to stress that a longer dataset could further enhance the robustness of the results, as new events could be included in the analysis. This, however, would require significant efforts, especially in the light of the challenges imposed by the specifics

of the site (e.g., the heterogeneous substrate, snow dynamics, the high frequency of floods and presence of grazing animals that might interfere with the sensors). Furthermore, more extensive field campaigns would not significantly modify the main conclusions of this study, as the features outlined in the paper emerged systematically from the data collected during a sequence of events, which were few in number but characterized by heterogeneous hydroclimatic features.

Theoretical framework and hierarchical activation. The analysis elucidates the major implications of the observed hierarchical behaviour of temporary streams on the spatial statistics of the node states and the temporal dynamics of the flowing length. In particular, temporal changes of the active drainage density are linked to the catchment water balance through the mean persistency of the whole network, whereas observed spatial patterns of flowing streams maximize the spatial correlation of the node states (wet vs. dry). The internal heterogeneity of the node persistency, though reflecting landscape complexity, is also modulated by climate and proves to be particularly enhanced under intermediate climatic conditions, leading to larger dynamical channel lengths in these settings. Furthermore, because changes in wetness are generally synchronized, stream networks tend to be highly dynamic (i.e., they are nearly as dynamic as they can possibly be). Consequently, temporal variations of the active stream length and their climatic controls should be properly taken into account for accurate regional or global assessment of biogeochemical and ecological function of stream networks, particularly with changing climate.

The Stream Length Duration Curve. The concept of Stream Length Duration Curve was proposed and formalized, as a novel hydrologic index that can be used to efficiently summarize the effect of hydrological variability on the extent of the flowing stream network under a variety of climatic conditions and field settings. A stochastic model has been developed to link the shape of the SLDC to the local persistency of the stream network nodes and its spatial correlation. The mean length of the stream network is solely dictated by the mean persistency of the different nodes of the stream network; the higher the overall average of the node persistencies, the higher the mean length of the active streams and the area of the Stream Length Duration Curve. The shape of the SLDC, instead, is driven by the pdf of the local persistencies. In particular, intermediate persistencies enhance the network length dynamics, thereby implying steeper SLDCs. Conversely, low or high persistencies smooth the changes of the active stream length through time, and originate nearly-horizontal SLDCs. When the activation of the stream network is hierarchical, as described above, the state of the network nodes is highly correlated and the temporal variability of the network length is enhanced; under these circumstances, the SLDC corresponds to the spatial Cumulative Distribution Function of the persistency of the different nodes in the network (i.e. space for time substitution is allowed). The Stream Length Duration Curve of the Valfredda river was estimated based on the conducted field surveys. The SLDC of this humid headwater catchment of the Italian Alpine region is quite steep and regular, with an average slope of $1\,km$ for percentile. This reflects a pronounced sensitivity of the length of active streams to the underlying hydrological conditions. This work provides a basis for

the development of comparative studies of stream network dynamics across different climatic regions and offers a clue for the development of stochastic and mechanistic models for the expansion and contraction of actively flowing streams.

Statistical modeling of the active length. One of the main goals of the study was to quantitatively analyze how the unsteady nature of the climatic forcing controls stream network dynamics. Empirical data and model results indicate that the temporal dynamics of the stream network length are mainly driven by the observed patterns (timing and amount) of short and long-term antecedent precipitation. The comparison of the different models also suggests that evapotranspiration does not affect significantly the observed intra-seasonal changes of stream length in the Valfredda catchment, possibly due to the high runoff ratios typical of this Alpine region and the low percentage of forested areas (almost 30% of the total area).

The modeling results indicate the presence of multiple expansion and retraction cycles operating at different time scales behind the observed dynamics of the Rio Valfredda stream network. These overlapping dynamics may be in turn controlled by two distinct hydrological processes: i) quick subsurface flow in the root zone feeding temporary streams; and ii) slower groundwater flow generated by the aquifers supplying water to the less dynamical reaches of the river network. The superposition of dynamics characterized by different time scales could lie at the basis of the hysteresis frequently observed in the relationship between discharge and L (Shaw et al. 2017; Jensen et al. 2018; Ward et al. 2018; Prancevic et al. 2019). In spite of the empirical nature of the link between L and precipitation provided here, these results could provide a preliminary basis to incorporate the simulation of network expansion and contraction in hydrological models using climatic data.

The value of active length vs streamflow relationships. An analytical model for the characterization of the streamflow regimes has been integrated with the empirical power law model that links active length (L) and specific discharge (q) to provide a probabilistic description of the temporal variations of the flowing length of a dynamic stream network. Novel analytical expressions have been derived for the probability density function of the flowing length and for the Stream Length Duration Curve (SLDC) based on five simple hydroclimatic and morphological parameters. These expressions link the statistics of the active stream length to a set of relevant hydrological processes including rainfall dynamics, recession characteristics and the sensitivity of the active length to changes in the catchment discharge. The model has been tested using data from three different headwater catchments located in Italy and in the USA. The selected case studies provide representative scenarios characterized by different hydrologic conditions (e.g. temperature, rainfall, evapotranspiration, vegetation and soil/geologic properties). Model performances were satisfactory with a mean of the annual $SMAE$s across the case studies of 15% for the FDC and 33.0% for the SLDC. Larger errors were typically associated to drier climates and highly dynamic stream networks.

The proposed theoretical analysis revealed that streamflow and active length regimes are only dependent on two dimensionless parameters: i) the ratio between the frequency of flow pulses and the catchment recession rate λ/k; ii) and the scaling

exponent that regulates the relationship between L and q, b. In particular, analytical arguments and empirical evidence indicate that, depending on the value of the dimensionless parameters λ/k and b, seven different classes of behaviour can be identified (from "class A" to "class G"). These classes correspond to different combinations of streamflow regimes (erratic or persistent) and active length regimes (perennial, ephemeral de facto, ephemeral). In general, when $b < 1$ ($b > 1$), the SLDC is flatter (steeper) than the corresponding flow duration curve. On the other hand, when $b \simeq 1$ the shape of the FDC and that of the SLDC are similar. The variety of hydrological behaviours predicted by the theory is also confirmed by the analysis of the empirical data, and suggest that the proposed model and the implied joint classification from the flow and active length regimes might be useful tools for an objective and simple estimation of the joint dynamics of q and L in catchments characterized by diverse climate, geological and morphological features.

Spatio-temporal dynamics of the active network This thesis also shows how network dynamics can be reconstructed and visualized starting from precipitation data and using a limited number of field surveys (approach 1), or stochastically modeled on the basis of few climatic and hydrologic parameters (approach 2).

The first approach is based on the assumption that the activation of the network nodes is hierarchical, and utilizes an empirical regression between active length and precipitation. This novel visualization technique presented allows an optimized use of the empirical data about active stream dynamics, providing useful information on the influence of precipitation on network expansion and contraction cycles. The approach is also useful to enhance the resolution of empirical data within the proposed mathematically robust framework, in which the temporal and spatial dimensions of the problem are suitably connected through the persistence of the network nodes, allowing an easiest identification of the spatio-temporal patterns of network expansion and contraction in temporary streams.

The second approach allows the coupled simulation of streamflow at the outlet and network dynamics, on the hypothesis that changes in Q and L are synchronized because streamflow increases (decreases) are driven by the same precipitation events (dry spells) that also affect network expansion (contraction). Streamflow is stochastically simulated with the model developed by Botter et al. 2010b, and, thanks to the hierarchical activation scheme, used to define the configuration of the active network on the basis of the local persistencies. This setup allows the modeling of the full spatio-temporal dynamics of a temporary streams on the basis of only four, physically-based, parameters, that are mean daily precipitation intensity α and frequency λ, recession rate k and potential evapotranspiration E_p. The parsimonious nature of this model facilitates the simulation and comparison of multiple scenarios spanning very different climates and hydrological behaviors, and once again highlights the fundamental importance of precipitation in the dynamics of a stream network. Dry climates exhibit erratic flow regimes due to the synergy of irregular water input and fast recessions. The recession of the active length proved to be even faster, thanks to the low local persistency of the nodes, generating long spells during which the stream network is almost completely dry that are interrupted by flashy activations of the network, leading to a significant variability of the active length. Wet

climates, instead, are characterized by a steadier water input and slower recessions, and results in timeseries of Q and L that are less variable around the mean.

The stochastic model was used as a basis for carrying out ecological simulations of the occupancy of a metapopulation in a temporary riverine systems. The simulations suggest the fundamental role that network dynamics play on metapopulation survival: dynamic river networks, in fact, show a significantly lower mean occupancy and a much higher variability of the extent of occupied network with respect to their average static counterparts, particularly in erratic regimes where metapopulation dispersal is consistently prevented by the limited length of the active network. This reduced stability of the metapopulation on dynamic streams is also reflected in higher probabilities of extinction, and is enhanced by the presence of disconnections in the active network, that further limit the ability of the metapopulation to disperse in un-occupied nodes. This confirms that not only network geometry, but also its dynamicity should be considered a fundamental characteristic of a river.

Stream network dynamics are expected to impact a huge number of biogeochemical and ecological processes, including the release of CO_2 from headwater streams to the atmosphere, and the export of carbon and nutrients from uplands to downstream ecosystems (e.g. Battin et al. 2009; Bertuzzo et al. 2017; Dick et al. 2014; Dupas et al. 2019; Ensign et al. 2006; Fasching et al. 2016; Helton et al. 2017; Krause et al. 2017; Von Schiller et al. 2014). As such, the theoretical and modeling efforts presented in this thesis may prove to become useful tools in many stream-related disciplines, and for the development and application of management strategies for the protection of riverine ecosystems.

Appendix A Performance of the hierarchical model

The accuracy of the hierarchical model on each of the study networks is calculated by means of equation (11) of the methods. Figure A.2 shows the maps of the local accuracy of the hierarchical model for each study catchment. The figures indicate that the local accuracy is close to 100% in most cases. The average accuracy within each study catchment is reported in Table 7.2. In the framework presented in this paper, the local persistency is calculated from empirical observations. Given that node persistency dictates the fraction of time for which a node is active, one could expect that a model in which each node is randomly activated/deactivated through time in a way that is consistent with the local persistency could have a positive accuracy. In fact, the accuracy of such a random model for a node with persistency P_i is $P_i^2 + (1 - P_i)^2$, leading to a minimum accuracy of 50%. The accuracy of the hierarchical model was thus compared to the accuracy of the random model for all the study catchments. Figure A.3 shows the maps of local accuracy that would be obtained from the random model. Figure A.1 shows that the mean accuracy of the hierarchical model ($99 \pm 1.7\%$) is substantially higher than the accuracy of the random model ($79 \pm 7.5\%$).

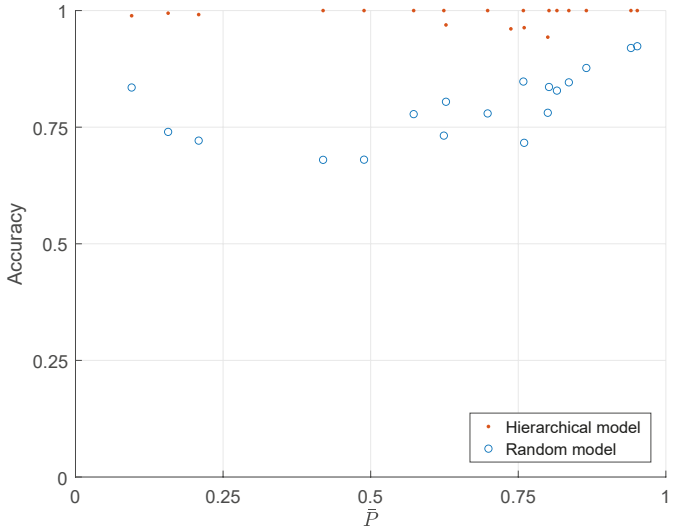

Figure A.1: Accuracy of the hierarchical and random models as a function of the mean network persistency.

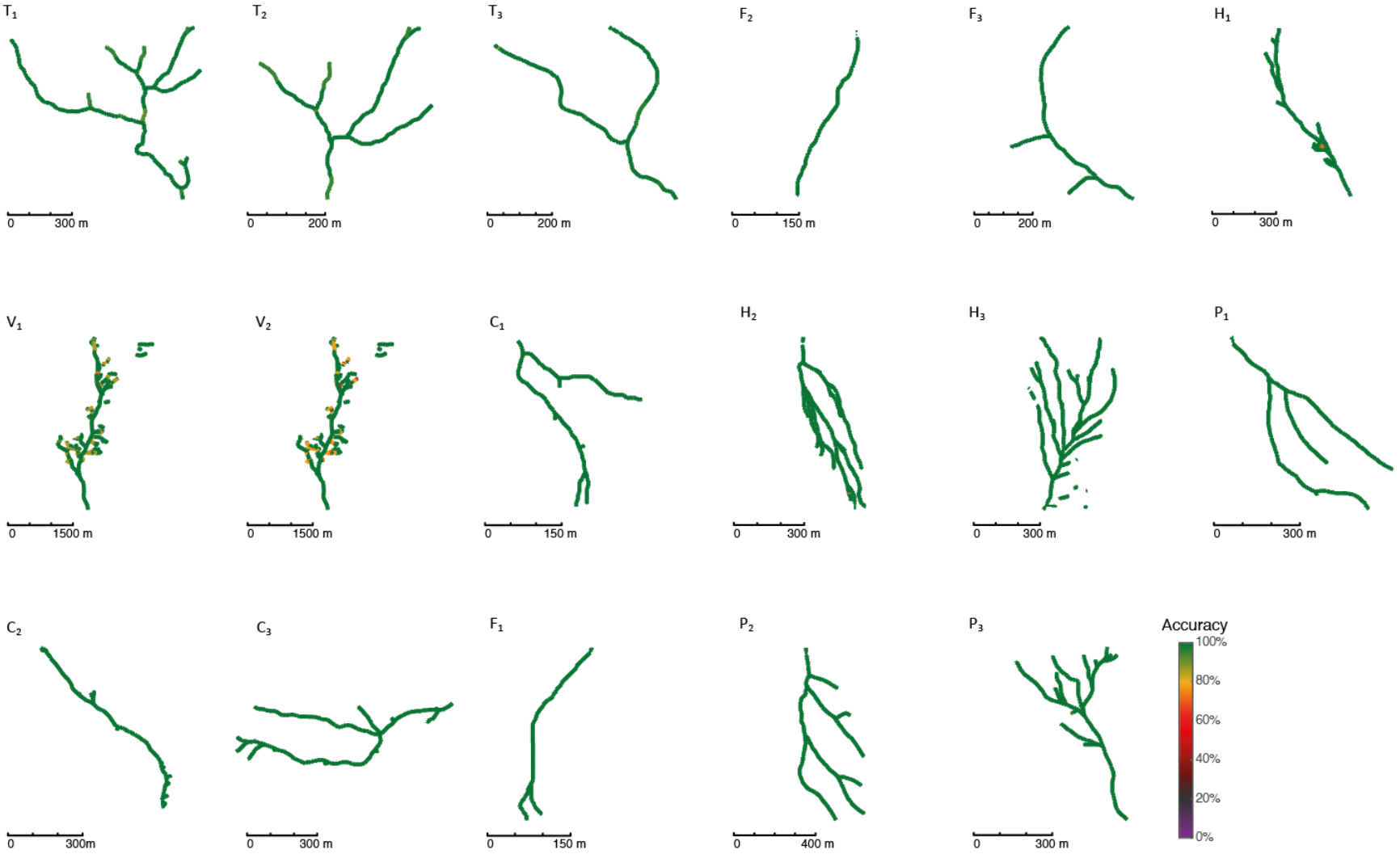

Figure A.2: Maps of local accuracy of the hierarchical model for a set of the study catchments.

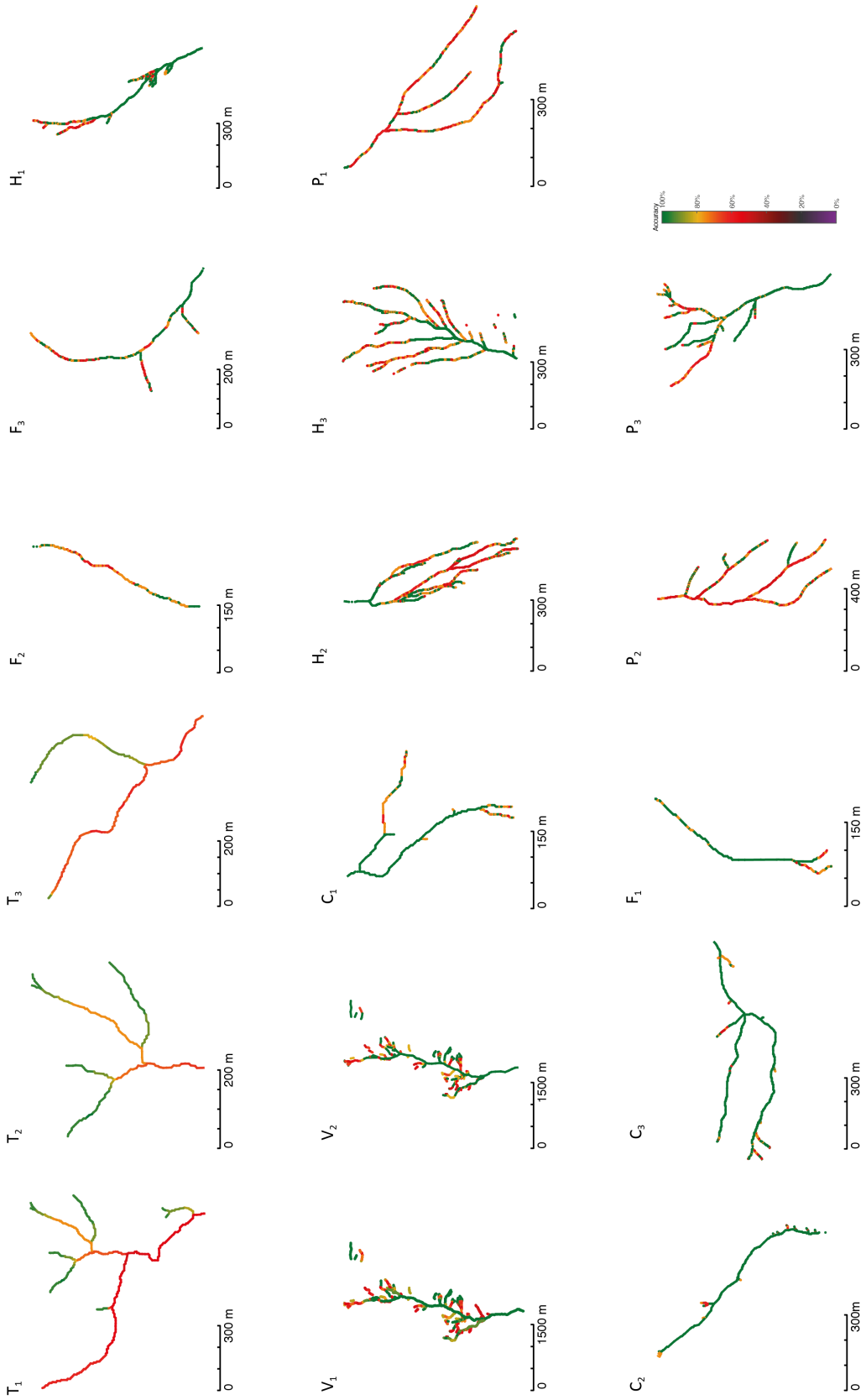

Figure A.3: Maps of local accuracy of the random model.

Appendix B Monitoring hierarchical networks

If the activation and deactivation of the nodes of a dynamic stream network obeys to a purely hierarchical scheme, the monitoring of active stream length dynamics can be significantly facilitated. In fact, the hierarchical assumption can be used to deduce the status of some nodes in the network from the observed status of other nodes. Specifically, if a node is observed as wet then all the nodes in the network with a larger persistency should be wet. Likewise, if a node is dry, then all the nodes with a smaller persistency should be dry as well. One might argue that prior to the field campaign for the monitoring of active stream network dynamics the persistencies of the nodes are not known. However, as long as the surveys take place, this hierarchy is progressively revealed and, crucially, the hierarchies emerging during any survey will remain unchanged for the entire campaign. Thus, as the number of available active stream network maps increases, the ability to extrapolate in space information about the status of the nodes increases as well. To quantify the number of nodes that do not need to be visited during a field campaign (because their status can be deduced from the status of other nodes), a series of numerical simulations was performed in which I simulated the dynamics of the stream network by simulating a hierarchical chain of nodes and the position of the transition between wet and dry nodes in the chain. Likewise, the number of nodes that has to be visited using the information available prior to the survey is computed. These numerical simulations consisted in the following steps: i) a sequence of N nodes with a dichotomic status and a fixed distribution of the local persistencies is considered; ii) the nodes are first re-ordered in a chain following a decreasing order of local persistency (the first node is the most persistent, the last node the least persistent); iii) an auxiliary counting variable, k, is set equal to 1; iii) the position of the unique transition between wet and dry nodes in the chain is identified by selecting randomly one of the existing groups of nodes in the chain; if $k = 1$ the position of the transition is set within the unique group containing all the N nodes of the chain; iv) the selected group is then randomly split into two sub groups (namely, the group of wet nodes and the group of dry nodes) and a new group is thus created; v) a new hierarchy is created between these two node subgroups by assigning an apparent persistency P_a to the existing $k + 1$ groups as follows: $P_a = s/k$, where s is the number of times that a group of nodes was observed as active during the campaign up to the k^{th} survey; vi) the number of nodes to be visited during the k^{th} survey to characterize the whole active network is then computed as the sum of the number of nodes that need to

be surveyed to identify the groups within which the transition takes place (i.e., the number of existing groups k) plus the number of nodes that need to be visited to identify the precise location of that transition within the nodes of the relevant groups (all the nodes that are included in the two groups where the transition takes place); vii) the counting variable k is increased to the subsequent integer number and the procedure starts again from step iii). The procedure stops when a pre-determined number of field surveys (say, K) is performed. The percentage of nodes that has to be surveyed is then calculated as the number of surveyed nodes during the whole campaign scaled to the number of nodes that potentially have to be visited (i.e., $N\,K$). The simulations were performed with different combinations of K, N and $\bar{P}$, and the results are shown in Figure B.1. The plot indicates that, for hierarchical networks, the number of nodes to be visited is between 60 to 30 % of the overall number of nodes that should be surveyed in non-hierarchical networks, with smaller percentages associated to field campaigns made up of a larger number of surveys.

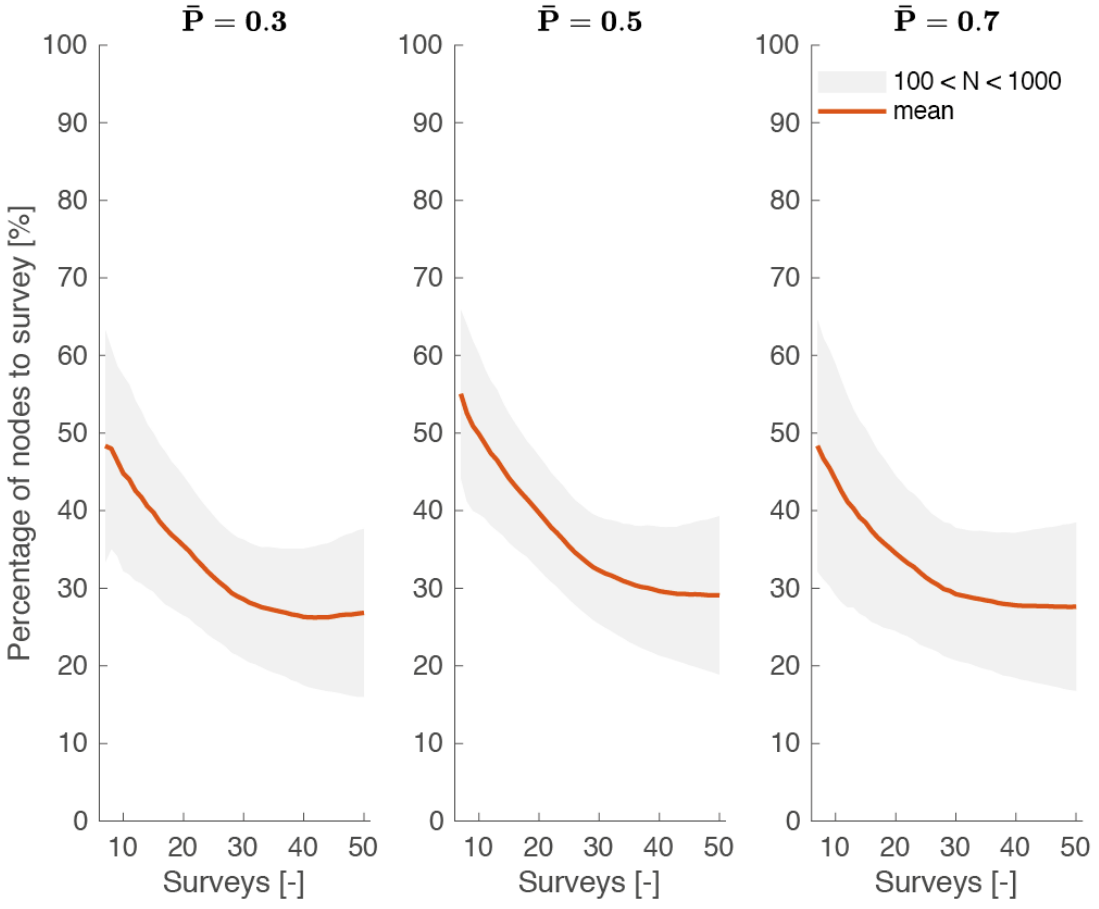

Figure B.1: Percentage of nodes to survey in perfectly hierarchical networks, as a function of the number of performed surveys and the number of nodes, N. The orange line shows the average, while the shadowed area shows the range obtained by varying the number of nodes in the network between 100 and 1000.

Bibliography

Abbott, B.W. et al. (2016). "Using multi-tracer inference to move beyond single-catchment ecohydrology". In: *Earth-Science Reviews* 160, pp. 19–42. ISSN: 00128252. DOI: 10.1016/j.earscirev.2016.06.014. URL: http://dx.doi.org/10.1016/j.earscirev.2016.06.014.

Abbott, K.C. (2011). "A dispersal-induced paradox: Synchrony and stability in stochastic metapopulations". In: *Ecology Letters* 14.11, pp. 1158–1169. ISSN: 1461023X. DOI: 10.1111/j.1461-0248.2011.01670.x.

Abramowitz, M. and S. Irene (1994). *Handbook of Mathematical Functions with formulas, graphs and mathematical tables*. Dove Publications, inc.

Acuña, V. et al. (2014). "Why should we care about temporary waterways?" In: *Science* 343. DOI: 10.1126/science.1246666.

Agren, A.M., W. Lidberg, and E. Ring (2015). "Mapping temporal dynamics in a forest stream network - implications for riparian forest management". In: *Forests* 6(9), pp. 2982–3001. DOI: 10.3390/f6092982.

Akaike, H. (1974). "A new look at the statistical model identification". In: *Trans Autom Control*, pp. 716–723. DOI: 10.1109/TAC.1974.1100705.

Allen, R.G. et al. (1996). "Modification of the FAO crop coefficient approach". In: *Proceedings of the International Conference*, pp. 124–132.

Allen, R.G. et al. (1998). *Guidelines for computing crop water requirements*. Food and Agriculture Organization of the United Nations.

Anderson, M.G. and T.P. Burt (1978). "Analysis of spatial water quality and stream networks in Southern Cotswolds during and after the drought of 1976". In: *Earth Surface Processes* 3, pp. 59–69. DOI: 10.1002/esp.3290030106.

Assendelft, R.S. and H.J.I. Van Meerveld (2019). "A low-cost, multi-sensor system to monitor temporary stream dynamics in montainous headwater catchments". In: *Sensors* 19. DOI: 10.3390/s19214645.

Banavar, J.R., A. Maritan, and A. Rinaldo (1999). "Size and form in efficient transportation networks". In: *Nature* 399, pp. 130–132. DOI: 10.1038/20144.

Basso, S., M. Schirmer, and G. Botter (2015). "On the emergence of heavy-tailed streamflow distributions". In: *Advances in Water Resources* 82, pp. 98–105. ISSN: 03091708. DOI: 10.1016/j.advwatres.2015.04.013. URL: http://dx.doi.org/10.1016/j.advwatres.2015.04.013.

Basso, S., M. Schirmer, and G. Botter (2016). "A physically based analytical model of flood frequency curves". In: *Geophysical Research Letters* 43. DOI: 10.1002/2016GL069915.

Battin, T.J. et al. (2008). "Biophysical controls on organic carbon fluxes in fluvial networks". In: *Nature Geoscience* 1, pp. 95–100. DOI: 10.1038/ngeo101.

Battin, T.J. et al. (2009). "The boundless carbon cycle". In: *Nature Geoscience* 2, pp. 598–600. DOI: 10.1038/ngeo618.

Belsley, D.A. (1991). "A guide to using the collinearity diagnostics". In: *Computer Science in Economics and Management* 4, pp. 33–50. DOI: 10.1007/BF00426854.

Berger, E. et al. (2017). "Water quality variables and pollution sources shaping stream macroinvertebrate communities". In: *Science of the Total Environment* 587-588, pp. 1–10. ISSN: 18791026. DOI: 10.1016/j.scitotenv.2017.02.031. URL: http://dx.doi.org/10.1016/j.scitotenv.2017.02.031.

Bertassello, L.E. et al. (2019). "Wetlandscape hydrologic dynamics driven by shallow groundwater and landscape topography". In: *Hydrological Processes* 34.6, pp. 1460–1474. ISSN: 10991085. DOI: 10.1002/hyp.13661.

Bertassello, L.E. et al. (2020). "Emergent dispersal networks in dynamic wetlandscapes". In: *Scientific Reports* 10.1, pp. 1–10. ISSN: 20452322. DOI: 10.1038/s41598-020-71739-8. URL: https://doi.org/10.1038/s41598-020-71739-8.

Bertassello, L.E. et al. (2021). "Dynamic spatio-temporal patterns of metapopulation occupancy in patchy habitats". In: *Royal Society Open Science* 8.1. ISSN: 20545703. DOI: 10.1098/rsos.201309.

Bertuzzo, E. et al. (2017). "Scaling of dissolved organic carbon removal in river networks". In: *Advances in Water Resources* 110, pp. 136–146. DOI: 10.1016/j.advwatres.2017.10.009.

Betterle, A., M. Schirmer, and G. Botter (2017). "Characterizing the spatial correlation of daily streamflows". In: *Water Resources Research* 53, pp. 1646–1663. DOI: 10.1002/2016WR019195.

Beven, K.J. and M.J. Kirkby (1979). "A physically based, variable contributing area model of basin hydrology". In: *Hydrological Sciences Journal* 24, pp. 43–69. DOI: 10.1080/02626667909491834.

Blyth, K. and J. Rodda (1973). "A stream length study". In: *Water Resources Research* 9(5), pp. 1464–1461.

Boodoo, Kyle S. et al. (2017). "Gravel bars are sites of increased CO2 outgassing in stream corridors". In: *Scientific Reports* 7.1, pp. 1–9. DOI: 10.1038/s41598-017-14439-0.

Borg Galea, A. et al. (2019). "Mediterranean intermittent rivers and ephemeral streams: Challenges in monitoring complexity". In: *Ecohydrology* 12.8, pp. 1–11. ISSN: 19360592. DOI: 10.1002/eco.2149.

Botter, G. and N. Durighetto (2020). "The Stream Length Duration Curve: A Tool for Characterizing the Time Variability of the Flowing Stream Length". In: *Water Resources Research* 56.8. ISSN: 19447973. DOI: 10.1029/2020WR027282.

Botter, G. and A. Rinaldo (2003). "Scale effect on geomorphologic and kinematic dispersion". In: *Water Resources Research* 39 (10). DOI: 10.1029/2003WR002154.

Botter, G. et al. (2007). "Basin-scale soil moisture dynamics and the probabilistic characterization of carrier hydrologic flows: Slow, leaching-prone components of the hydrologic response". In: *Water Resources Research* 43.2, pp. 1–14. ISSN: 00431397. DOI: 10.1029/2006WR005043.

Botter, G. et al. (2010a). "Natural streamflow regime alterations: Damming of the Piave river basin (Italy)". In: *Water Resources Research*.

Botter, G. et al. (2010b). "Natural streamflow regime alterations: Damming of the Piave river basin (Italy)". In: *Water Resources Research* 46.6, pp. 1–14. ISSN: 00431397. DOI: 10.1029/2009WR008523. URL: http://dx.doi.org/10.1029/2009WR008523,%20doi:10.102.

Botter, G. et al. (2010c). "Stochastic modeling of nutrient losses in streams: Interactions of climatic, hydrologic, and biogeochemical controls". In: *Water Resources Research* 46.8, pp. 1–14. ISSN: 00431397. DOI: 10.1029/2009WR008758.

Botter, G. et al. (2013). "Resilience of river flow regimes". In: *Proceedings of the National Academy of Sciences* 110.32, pp. 12925–12930.

Boulton, A.J. et al. (2017). *Hydrological Connectivity in Intermittent Rivers and Ephemeral Streams*. Elsevier Inc., pp. 79–108. ISBN: 9780128039045. DOI: 10.1016/B978-0-12-803835-2.00004-8. URL: http://dx.doi.org/10.1016/B978-0-12-803835-2.00004-8.

Briggs, M.A. et al. (2019). "Efficient hydrogeological characterization of remote stream corridors using drones". In: *Hydrological Processes* 33.2, pp. 316–319. ISSN: 10991085. DOI: 10.1002/hyp.13332.

Brown, J. and K.B. Astrid (1977). "Turnover Rates in Insular Biogeography : Effect of Immigration on Extinction". In: *Ecology* 58.2, pp. 445–449. DOI: 10.2307/1935620.

Budyko, M.I. (19774). *Climate and life*. Vol. 18. Elsevier. ISBN: 9780080954530.

Burrows, R.M. et al. (2017). "High rates of organic carbon processing in the hyporheic zone of intermittent streams". In: *Scientific reports* 7. DOI: 10.1038/s41598-017-12957-5.

Buttle, J.M. et al. (2012). "An overview of temporary stream hydrology in Canada". In: *Canadian Water Resources Journal* 37(4), pp. 279–310. DOI: 10.4296/cwrj2011-903.

Campbell Grant, E.H., W.H. Lowe, and W.F. Fagan (2007). "Living in the branches: Population dynamics and ecological processes in dendritic networks". In: *Ecology Letters* 10.2, pp. 165–175. ISSN: 1461023X. DOI: 10.1111/j.1461-0248.2006.01007.x.

Cardenas, M.B. (2007). "Potential contribution of topography-driven regional groundwater flow to fractal stream chemistry: residence time distribution analysis of Tòth flow". In: *Geophysical research letters* 34. DOI: 10.1029/2006GL029126.

Casas-Mulet, R. et al. (2020). "Unmanned Aerial Vehicle (UAV)-Based Thermal Infra-Red (TIR) and Optical Imagery Reveals Multi-Spatial Scale Controls of Cold-Water Areas Over a Groundwater-Dominated Riverscape". In: *Frontiers in Environmental Science* 8.May, pp. 1–16. ISSN: 2296665X. DOI: 10.3389/fenvs.2020.00064.

Castellarin, A. et al. (2004). "Regional flow-duration curves: Reliability for ungauged basins". In: *Advances in Water Resources* 27.10, pp. 953–965. ISSN: 03091708. DOI: 10.1016/j.advwatres.2004.08.005.

Ceola, S. et al. (2010). "Comparative study of ecohydrological streamflow probability distributions". In: *Water Resources Research* 46.9, pp. 1–12. ISSN: 00431397. DOI: 10.1029/2010WR009102.

Chapin, T.P., A.S. Todd, and M.P. Zeigler (2014). "Robust, low-cost data loggers for stream temperature, flow intermittency, and relative conductivity monitoring". In: *Water Resources Research*, pp. 1–17. DOI: 10.1002/2013WR015158.

Collins, D.B.G. and R.L. Bras (2010). "Climatic and ecological controls of equilibrium drainage density, relief, and channel concavity in dry lands". In: *Water Resources Research* 46. DOI: 10.1029/2009WR008615.

Dai, B., S. Ding, and G. Wahba (2013). "Multivariate Beronulli distribution". In: *Bernoulli* 19(4), pp. 1465–1483. DOI: 10.3150/12-BEJSP10.

Datry, T., S.T. Larned, and K. Tockner (2014). "Intermittent rivers: a challenge for freshwater ecology". In: *Bioscience*, pp. 229–235. DOI: 10.1093/biosci/bit027.

Datry, T. et al. (2016). "A landscape approach to advance intermittency river ecology". In: *Freshwater Biology* 61, pp. 1200–1213. DOI: 10.1111/fwb.12645.

Datry, T. et al. (2017). "Flow intermittence and ecosystem services in rivers of the Antropocene". In: *Journal of Applied Ecology* 55, pp. 353–364. DOI: 10.1111/1365-2664.12941.

Datry, T. et al. (2018). "A global analysis of terrestrial plant litter dynamics in non-perennial waterways". In: *Nature Geoscience* 11.7, pp. 497–503. ISSN: 17520908. DOI: 10.1038/s41561-018-0134-4.

Day, D.G. (1978). "Drainage density changes during rainfall". In: *Earth Surface Processes* 3, pp. 319–326.

Day, D.G. (1980). "Lithologic controls of drainage density. A study of six small rural catchments in New England, N.S.W." In: *Catena* 7.1, pp. 339–351. ISSN: 03418162. DOI: 10.1016/S0341-8162(80)80024-5.

Day, D.G. (1983). "Drainage density variability and drainage basin outputs". In: *Journal of Hydrology (New Zealand)* 22.1, pp. 3–17. URL: http://www.jstor.org/stable/43944508.

DeAngelis, D.L. et al. (2010). "Fish population dynamics in a seasonally varying wetland". In: *Ecological Modelling* 221.8, pp. 1131–1137. ISSN: 03043800. DOI: 10.1016/j.ecolmodel.2009.12.021. URL: http://dx.doi.org/10.1016/j.ecolmodel.2009.12.021.

Debell, L. et al. (2015). "Water resource management at catchment scales using lightweight uavs: Current capabilities and future perspectives". In: *Journal of Unmanned Vehicle Systems* 4.1, pp. 7–30. ISSN: 22913467. DOI: 10.1139/juvs-2015-0026.

Dick, J.J. et al. (2014). "Modelling landscape controls on dissolved organic carbon sources and fluxes to streams". In: *Biogeochemistry* 122(2-3), pp. 361–374.

Doering, M. et al. (2007). "Ecosystem expansion and contraction dynamics along a large Alpine alluvial corridor (Tagliamento River, Northeast Italy)". In: *Earth Surface Processes and Landforms* 32, pp. 1693–1704. DOI: 10.1002/esp.1594.

Doulatyari, B. et al. (2015). "Predicting streamflow distributions and flow duration curves from landscape and climate". In: *Advances in Water Resources* 83, pp. 285–298. ISSN: 03091708. DOI: 10.1016/j.advwatres.2015.06.013. URL: http://dx.doi.org/10.1016/j.advwatres.2015.06.013.

Dupas, R. et al. (2019). "Distribution of Landscale Units Within Catchments Influences Nutrient Export Dynamics". In: *Font. Environ. Sci.* DOI: 10.3389/fenvs.2019.00043.

Durighetto, N. and G. Botter (2021). "Time-lapse visualization of spatial and temporal patterns of stream network dynamics". In: *Hydrological Processes* 35.2, pp. 10–12. ISSN: 10991085. DOI: 10.1002/hyp.14053.

Durighetto, N. et al. (2020). "Intraseasonal drainage network dynamics in a headwater catchment in the Italian Alps". In: *Water Resources Research* 56. DOI: 10.1029/2019WR025563.

Ensign, S.H. and W.D. Martin (2006). "Nutrient spiraling in streams and river networks". In: *Journal of Geophysical Research: Biogeosciences* 111(G4). DOI: 10.1029/2005JG000114.

Fagan, W.F. (2002). "Connectivity , Fragmentation , and Extinction Risk in Dendritic Metapopulations". In: 83.12, pp. 3243–3249. ISSN: 00129658.

Fagan, W.F. et al. (2009). "Interspecific variation in critical patch size and gap-crossing ability as determinants of geographic range size distributions". In: *American Naturalist* 173.3, pp. 363–375. ISSN: 00030147. DOI: 10.1086/596537.

Fahrig, L. (1992). "Relative importance of spatial and temporal scales in a patchy environment". In: *Theoretical Population Biology* 41, pp. 300–314. ISSN: 00405809.

Fasching, C. et al. (2016). "Hydrology controls dissolved organic matter export and composition in an Alpine stream and its hyporheic zone". In: *Limnology and oceanography* 61(2), pp. 558–571. DOI: 10.1002/lno.10232.

Fritz, K.M., B.R. Johnson, and D.M. Walters (2008). "Physical indicators of hydrologic permanence in forested headwater streams". In: *Journal of the North American Benthological Society* 27, pp. 690–704. DOI: 10.1899/07-117.1.

Fritz, K.M., W.R. Wenerick, and M.S. Kostich (2013). "A validation study of a rapid field-based rating system for discriminating among flow permanence classes of headwater steams in South Carolina". In: *Environmental management* 52, pp. 1286–1298. DOI: 10.1007/s00267-013-0158-x.

Gallart, F. et al. (2012). "A novel approach to analysing the regimes of temporary streams in relation to their controls on the composition and structure of aquatic biota". In: *Hydrology and Earth System Sciences* 16, pp. 3165–3182. DOI: 10.5194/hess-16-3165-2012.

Gallart, F. et al. (2017). "TREHS: An open-access software tool for investigating and evaluating temporary river regimes as a first step for their ecological status assessment". In: *Science of the total environment* 607-608, pp. 519–540. DOI: 10.1016/j.scitotenv.2017.06.209.

Gallo, E.L. et al. (2020). "Estimating Surface Water Presence and Infiltration in Ephemeral to Intermittent Streams in the Southwestern US". In: *Frontiers in Water* 2. DOI: 10.3389/frwa.2020.572950.

Garbin, S. et al. (2019). "Hydrological controls on river network connectivity". In: *Royal Society Open Science* 6.2. ISSN: 20545703. DOI: 10.1098/rsos.181428.

Giezendanner, J. et al. (2019). "A minimalist model of extinction and range dynamics of virtual mountain species driven by warming temperatures". In: *PLoS ONE* 14.3, pp. 1–19. ISSN: 19326203. DOI: 10.1371/journal.pone.0213775.

Giezendanner, J. et al. (2021). "A note on the role of seasonal expansions and contractions of the flowing fluvial network on metapopulation persistence". In: *Water Resources Research*, pp. 1–18. ISSN: 0043-1397. DOI: 10.1029/2021wr029813.

Godsey, S.E. and J.W. Kirchner (2014). "Dynamic, discontinuous stream networks: hydrologically driven variations in active drainage density, flowing channels and stream order". In: *Hydrological Processes*. DOI: 10.1002/hyp.10310.

Gómez-Gener, L. et al. (2016). "When Water Vanishes: Magnitude and Regulation of Carbon Dioxide Emissions from Dry Temporary Streams". In: *Ecosystems* 19, pp. 710–723. DOI: 10.1007/s10021-016-9963-4.

González-Ferreras, A.M. and J. Barquín (2017). "Mapping the temporary and perennial character of whole river networks". In: *Water Resources Research* 53.8, pp. 6709–6724. ISSN: 19447973. DOI: 10.1002/2017WR020390.

Gordon, E.S. and M.A. Goñi (2003). "Sources and distribution of terrigenous organic matter delivered by the Atchafalaya River to sediments in the northern Gulf of Mexico". In: *Geochimica et Cosmochimica Acta* 67.13, pp. 2359–2375. DOI: 10.1016/S0016-7037(02)01412-6.

Goulsbra, C., M. Evans, and J. Lindsay (2014). "Temporary streams in a peatland catchment: pattern, timing, and controls on stream network expansion and contraction". In: *Earth Surface Processes and Landforms* 39(6), pp. 790–803. DOI: 10.1002/esp.3533.

Gregory, K. and V. Gardiner (1979). "Comment on drainage density and streamflow: a closer look by S. L. Dingman". In: *Water Resources Research* 15(6), pp. 1662–1664.

Gregory, K.J. and D.E. Walling (1968). "The variation of drainage density within a catchment". In: *International Association of Scientific Hydrology Bulletin* 13, pp. 61–68.

Hansen, W.F. (2001). "Identifying stream types and management implications". In: *Forest Ecology and Management* 143.1–3, pp. 39–46. DOI: 10.1016/S0378-1127(00)00503-X.

Hanski, I. (1994). "Patch-occupancy dynamics in fragmented landscapes". In: *Trends in Ecology and Evolution* 9.4, pp. 131–135. ISSN: 01695347. DOI: 10.1016/0169-5347(94)90177-5.

Hanski, I. and M. Gilpin (1991). "Metapopulation dynamics: empirical and theoretical investigations". In: *Biological Journal of the Linnean Society* 42.2, pp. 3–16. DOI: 10.1111/j.1095-8312.1991.tb00548.x.

Hanski, I. and O. Ovaskainen (2000). "The metapopulation capacity of a fragmented landscape". In: *Nature* 404.April, pp. 755–758.

Helton, A.M., R.O. Hall, and E. Bertuzzo (2017). "How network structure can affect nitrogen removal by streams". In: *Freshwater Biology* 63, pp. 128–140. DOI: 10.1111/fwb.12990.

Horton, R.E. (1945). "Erosional developement of streams and their drainage basins: hydrophysical approach to quantitative morphology". In: *GSA Bulletin* 56.3, pp. 275–370. DOI: 10.1130/0016-7606(1945)56[275:EDOSAT]2.0.CO;2.

Jaeger, K., J. Olden, and N. Pelland (2014). "Climate change poised to threaten hydrologic connectivity and endemic fishes in dryland streams". In: *Proceedings of the National Academy of Sciences of the United States of America* 111, pp. 13894–13899. DOI: 10.1073/pnas.1320890111.

Jaeger, K.L. and J.D. Olden (2012). "Electrical resistance sensor arrays as a means to quantify longitudinal connectivity of rivers". In: *River Research and Applications* 28, pp. 1843–1852. DOI: 10.1002/rra.1554.

Jaeger, K.L. et al. (2019). "Probability of streamflow permanence model (PROSPER): a spatially continuous model of annual streamflow permanence throughout the Pacific Northwest". In: *Journal of Hydrology X* 2. DOI: 10.1016/j.hydroa.2018.100005.

Jensen, A.M. et al. (2012). "Thermal remote sensing with an autonomous unmanned aerial remote sensing platform for surface stream temperatures". In: *International Geoscience and Remote Sensing Symposium (IGARSS)*, pp. 5049–5052. DOI: 10.1109/IGARSS.2012.6352476.

Jensen, C.K., K.J. McGuire, and P.S. Prince (2017). "Headwater stream length dynamics across four physiographic provinces of the Appalachian Highlands". In: *Hydrological Processes* 31, pp. 3350–3363. DOI: 10.1002/hyp.11259.

Jensen, C.K. et al. (2018). "Modeling wet headwater stream networks across multiple flow conditions in the Appalachian Highlands". In: *Earth surface processes and landforms* 43, pp. 2762–2778. DOI: 10.1002/esp.4431.

Jensen, C.K. et al. (Mar. 2019). "Quantifying spatiotemporal variation in headwater stream length using flow intermittency sensors". In: *Environmental Monitoring and Assessment* 191.4, p. 226. ISSN: 1573-2959. DOI: 10.1007/s10661-019-7373-8. URL: https://doi.org/10.1007/s10661-019-7373-8.

Kaplan, L.A. et al. (2019). "Monitoring ephemeral, intermittent and perennial streamflow: a dataset from 182 sites in the Attert catchment, Luxemburg". In: *Earth System Science Data* 11, pp. 1363–1374. DOI: 10.5194/essd-11-1363-2019.

Keller, P.S., N. Catalàn, and R. Marcé (2020). "Global CO_2 emissions from dry inland waters share common drivers across ecosystems". In: *Nature communications* 11. DOI: 10.1038/s41467-020-15929-y.

Kiel, B. A and M.B. Cardenas (2014). "Lateral hyporheic exchange throughout the Mississippi River network". In: 7.June, pp. 413–417. DOI: 10.1038/NGEO2157.

Kirchner, J.W. (1993). "Statistical inevitability of Horton's laws and the apparent randomness of stream channel networks". In: *Geology* 21, pp. 591–594. DOI: 10.1130/0091-7613(1993)021<0591:SIOHSL>2.3.CO;2.

Krause, S. et al. (2017). "Ecohydrological interfaces as hot spots of ecosystem processes". In: *Water Resources Research*. DOI: 10.1002/2016WR019516.

Kuhn, J. et al. (2021). "Assessing stream thermal heterogeneity and cold-water patches from UAV-based imagery: A matter of classification methods and metrics". In: *Remote Sensing* 13.7. ISSN: 20724292. DOI: 10.3390/rs13071379.

Lapides, D.A. et al. (2021). "Variability of stream extents controlled by flow regime and network hydraulic scaling". In: *Hydrological Processes*. ISSN: 0885-6087. DOI: 10.1002/hyp.14079.

Lazzaro, G. et al. (2013). "Water management strategies for run-of-river power plants: profitability and hydrologic impact between the intake and the outflow". In: *Water Resources Research*.

Leigh, C. et al. (2016). "Ecological research and management of intermittent rivers: an historical review and future directions". In: *Freshwater Biology* 61, pp. 1181–1199. DOI: 10.1111/fwb.12646.

Levick, L. et al. (2018). "An ecohydrological stream type classification of intermittent and ephemeral streams in the southwestern United States". In: *Journal of Arid Environment* 155, pp. 16–35. DOI: 10.1016/j.jaridenv.2018.01.006.

Lovill, S.M., W.J. Hahm, and W.E. Dietrich (2018). "Drainage in the critical zone: lithologic controls on the persistence and spatial extent of wetted channels during the summer dry season". In: *Water Resources Research* 54, pp. 5702–5726. DOI: 10.1029/2017WR021903.

Lowe, W.H. et al. (2019). "Hydrologic variability contributes to reduced survival through metamorphosis in a stream salamander". In: *Proceedings of the National Academy of Sciences of the United States of America* 116.39, pp. 19563–19570. ISSN: 10916490. DOI: 10.1073/pnas.1908057116.

Malard, F. et al. (2006). "Flood-pulse and riverscape dynamics in a braided glacial river". In: *Ecology* 87(3), pp. 704–716.

Mari, L. et al. (2014). "Metapopulation persistence and species spread in river networks". In: *Ecology letters* 17, pp. 426–434. DOI: 10.1111/ele.12242.

Martensen, A.C., S. Saura, and M.J. Fortin (2017). "Spatio-temporal connectivity: assessing the amount of reachable habitat in dynamic landscapes". In: *Methods in Ecology and Evolution* 8.10, pp. 1253–1264. ISSN: 2041210X. DOI: 10.1111/2041-210X.12799.

Medici, C. et al. (2008). "Modelling the non-linear hydrological behviour of a small Mediterranean forested catchment". In: *Hydrological Processes* 22, pp. 3814–3828. DOI: 10.1002/hyp.6991.

Melton, M. A. (1957). "An analysis of the relations among elements of climate, surface properties, an geomorphology". In: *Office of Naval Research*.

Mianabadi, A. et al. (2019). "A global Budyko model to partition evaporation into interception and transpiration". In: *Hydrology and Earth System Sciences* 23.12, pp. 4983–5000. DOI: 10.5194/hess-23-4983-2019. URL: https://hess.copernicus.org/articles/23/4983/2019/.

Moglen, G.E., E.A.B. Eltahir, and R. L. Bras (1998). "On the sensitivity of drainage density to climate change". In: *Water Resources Research* 34, pp. 855–862. DOI: 10.1029/97WR02709.

Moilanen, A. (1999). "Patch occupancy models of metapopulation dynamics: Efficient parameter estimation using implicit statistical inference". In: *Ecology* 80.3, pp. 1031–1043. ISSN: 00129658. DOI: 10.1890/0012-9658(1999)080[1031:POMOMD]2.0.CO;2.

Moilanen, A. (2004). "SPOMSIM: Software for stochastic patch occupancy models of metapopulation dynamics". In: *Ecological Modelling* 179.4, pp. 533–550. ISSN: 03043800. DOI: 10.1016/j.ecolmodel.2004.04.019.

Montgomery, D.R. and W. E. Dietrich (1988). "Where do channels begin?" In: *Nature* 336, pp. 232–234. DOI: 10.1038/336232a0.

Montgomery, D.R. and W.E. Dietrich (1989). "Source areas, drainage density, and channel initiation". In: *Water Resources Research* 25, pp. 1907–1918. DOI: 10.1029/WR025i008p01907.

Morgan, R. (1972). "Observations on factors affecting the behaviour of a first-order stream." In: *Transactions of the Institute of British Geographers* 56, pp. 171–185.

Neachell, E. (2014). "Book Review - Environmental flows: Saving rivers in the thrid millennium". In: *River Research and Applications* 30.January, pp. 132–133. DOI: 10.1002/rra.

Nikolaidis, N.P. et al. (2013). "Towards sustainable management of Mediterranean river basins: Policy recommendations on management aspects of temporary streams". In: *Water Policy* 15.5, pp. 830–849. ISSN: 13667017. DOI: 10.2166/wp.2013.158.

Observatoire national des étiages (ONDE) dataset (n.d.). https://onde.eaufrance.fr.

Ocallaghan, J.F. and D.M. Mark (1984). "The extraction of drainage networks from digital elevation data". In: *Computer Vision, Graphics, and Image Processing* 28(3), pp. 323–344. DOI: 10.1016/S0734-189X(84)80011-0.

Osterkamp, W.R. and E.R. Hedman (1982). "Perennial-streamflow characteristics related to channel geometry and sediment in Missouri River basin". In: *USGS Publications Warehouse*. DOI: 10.3133/pp1242.

Ovenden, J.C. and K.J. Gregory (1980). "The permanence of stream networks in Britain". In: *Earth Surface Processes* 5, pp. 47–60.

Pai, H. et al. (2017). "Potential for Small Unmanned Aircraft Systems Applications for Identifying Groundwater-Surface Water Exchange in a Meandering River Reach". In: *Geophysical Research Letters* 44.23, pp. 11, 868–11, 877. ISSN: 19448007. DOI: 10.1002/2017GL075836.

Paillex, A. et al. (2020). "High stream intermittency in an alpine fluvial network: Val Roseg, Switzerland". In: *Limnology and Oceanography* 65.3, pp. 557–568. ISSN: 19395590. DOI: 10.1002/lno.11324.

Peirce, S.E. and J.B. Lindsay (2015). "Characterizing ephemeral streams in a southern Ontario watershed using electrical resistance sensors". In: *Hydrological Processes* 29, pp. 103–111. DOI: 10.1002/hyp.10136.

Perez, A.B.A. et al. (2020). "Connectivity of ephemeral and intermittent streams in a subtropical atlantic forest headwater catchment". In: *Water (Switzerland)* 12.6, pp. 1–15. ISSN: 20734441. DOI: 10.3390/W12061526.

Perry, G.L.W. and F. Lee (2019). "How does temporal variation in habitat connectivity influence metapopulation dynamics?" In: *Oikos* 128.9, pp. 1277–1286. ISSN: 16000706. DOI: 10.1111/oik.06052.

Pfister, L. et al. (2017). "Bedrock geology controls on catchment storage, mixing, and release: a comparative analysis of 16 nested catchments". In: *Hydrological Processes* 31, pp. 1828–1845. DOI: 10.1002/hyp.11134.

Phillips, R.W., C. Spence, and J.W. Pomeroy (2011). "Connectivity and runoff dynamics in heterogeneous basins". In: *Hydrological Processes* 25.19, pp. 3061–3075. ISSN: 08856087. DOI: 10.1002/hyp.8123.

Prancevic, J.P. and J.W. Kirchner (2019). "Topographic controls on the extension and retraction of flowing streams". In: *Geophysical Research Letters* 46, pp. 2084–2092. DOI: 10.1029/2018GL081799.

Prat, N. et al. (2014). "The Mirage toolbox: an integrated assessment tool for temporary streams". In: *River research and applications* 30, pp. 1318–1334. DOI: 10.1002/rra.2757.

Raymond, P.A. et al. (2013). "Global carbon dioxide emissions from inland waters". In: *Nature*, pp. 355–360. DOI: 10.1038/nature12760.

Reyjol, Y. et al. (2014). "Assessing the ecological status in the context of the European Water Framework Directive: Where do we go now?" In: *Science of the Total Environment* 497-498, pp. 332–344. ISSN: 18791026. DOI: 10.1016/j.scitotenv.2014.07.119. URL: http://dx.doi.org/10.1016/j.scitotenv.2014.07.119.

Ridolfi, E., H. Kumar, and A. Bárdossy (2020). "A methodology to estimate flow duration curves at partially ungauged basins". In: *Hydrology and Earth System Sciences* 24. DOI: 10.5194/hess-24-2043-2020.

Rinaldo, A et al. (1993). "Self-organized fractal river networks". In: *Physical Review Letters* 70, pp. 822–825. DOI: 10.1103/PhysRevLett.70.822.

Rinaldo, A., M. Gatto, and I. Rodriguez-Iturbe (2018). "River networks as ecological corridors: a coherent ecohydrological perspective". In: *Advances in water resources* 112, pp. 27–58. DOI: 10.1016/j.advwatres.2017.10.005.

Roberts, M.C. (1978). "Variation of drainage density in a small British Columbia watershed". In: *AWRA Water Resources Bulletin* 14(2), pp. 470–476.

Rodriguez-Iturbe, I. and A. Rinaldo (1997). *Fractal river basins: chance and self-organization*. Cambrige University Press. ISBN: 0521473985.

Rybicki, J. and I. Hanski (2013). "Species-area relationships and extinctions caused by habitat loss and fragmentation". In: *Ecology Letters* 16, pp. 27–38. ISSN: 1461023X. DOI: 10.1111/ele.12065.

Samboko, H.T. et al. (2020). "Evaluation and improvement of remote sensing-based methods for river flow management". In: *Physics and Chemistry of the Earth* 117, p. 102839. ISSN: 14747065. DOI: 10.1016/j.pce.2020.102839. URL: https://doi.org/10.1016/j.pce.2020.102839.

Sangireddy, H. et al. (2016). "Controls of climate, topography, vegetation and lithology on drainage density extracted from high resolution topography data". In: *Journal of Hydrology* 537, pp. 271–282. DOI: 10.1016/j.jhydrol.2016.02.051.

Sassolas-Serrayet, T., R. Cattin, and M. Ferry (2018). "The shape of watersheds". In: *Nature Communications* 9, p. 3791. DOI: 10.1038/s41467-018-06210-4.

Schiller, D. von et al. (2019). "Sediment respiration pulses in intermittent rivers and ephemeral streams". In: *Global Biogeochemical Cycles* 33, pp. 1251–1263. DOI: 10.1029/2019GB006276.

Searcy, J.K. (1959). "Flow-duration curves". In: *USGS Publication Warehouse*. DOI: 10.3133/wsp1542A.

Senatore, A. et al. (2020). "Monitoring and Modeling Drainage Network Contraction and Dry Down in Mediterranean Headwater Catchments". In: *Water Resources Research*. DOI: 10.1002/essoar.10504177.1.

Senatore, A. et al. (2021). "Monitoring and modeling drainage network contraction and dry down in Mediterranean headwater catchments". In: *Water Resources Research* 57. DOI: 10.1029/2020WR028741.

Settin, T. et al. (2007). "Numerical studies on soil moisture distributions in heterogeneous catchments". In: *Water Resources Research*.

Shaw, S.B. (2016). "Investigating the linkage between streamflow recession rates and channel network contraction in a mesoscale catchment in New York state". In: *Hydrological Processes* 30, pp. 479–492. DOI: 10.1002/hyp.10626.

Shaw, S.B., D.B. Bonville, and D.G. Chandler (2017). "Combining observations of channel network contraction and spatial discharge variation to inform spatial controls on baseflow in Birch Creek, Catskill Mountains, USA". In: *Journal of Hydrology: Regional Studies* 12, pp. 1–12. DOI: 10.1016/j.ejrh.2017.03.003.

Skoulikidis, N.T. et al. (2017). "Non-perennial Mediterranean rivers in Europe: Status, pressures, and challenges for research and management". In: *Science of the Total Environment* 577, pp. 1–18. DOI: 10.1016/j.scitotenv.2016.10.147.

Soulsby, C. et al. (2011). "Catchment-scale estimates of flow path partitioning and water storage based on transit time and runoff modelling". In: *Hydrologiacl Processes* 25.25, pp. 3960–3976. DOI: 10.1002/hyp.8324.

Spence, C. and S. Mengistu (2016). "Deployment of an unmanned aerial system to assist in mapping an intermittent stream". In: *Hydrological Processes* 30.3, pp. 493–500. ISSN: 10991085. DOI: 10.1002/hyp.10597.

Stoffels, R.J. et al. (2016). "Dynamics of fish dispersal during river-floodplain connectivity and its implications for community assembly". In: *Aquatic Sciences* 78.2, pp. 355–365. ISSN: 14209055. DOI: 10.1007/s00027-015-0437-0.

Stoll, S. and M. Weiler (2010). "Explicit simulations of stream networks to guide hydrological modelling in ungauged basins". In: *Hydrology and Earth System Science* 14, pp. 1435–1448. DOI: 10.5194/hess-14-1435-2010.

Stromberg, J.C. and D.M. Merritt (2016). "Riparian plant guilds of ephemeral, intermittent and perennial rivers". In: *Freshwater Biology* 61.8, pp. 1259–1275. ISSN: 13652427. DOI: 10.1111/fwb.12686.

Stubbington, R. et al. (2017). "Temporary streams in temperate zones: recognizing, monitoring and restoring transitional aquatic-terrestrial ecosystems". In: *Wiley Interdisciplinary Reviews: Water* 4. DOI: 10.1002/wat2.1223.

Stubbington, R. et al. (2018). "Biomonitoring of intermittent rivers and ephemeral streams in Europe: Current practice and priorities to enhance ecological status assessments". In: *Science of the total environment* 618, pp. 1096–1113. DOI: 10.1016/j.scitotenv.2017.09.137.

Stubbington, R. et al. (2019). "A comparison of biotic groups as dry-phase indicators of ecological quality in intermittent rivers and ephemeral streams". In: *Ecological Indicators* 97, pp. 165–174. DOI: 10.1016/j.ecolind.2018.09.061.

Svec, J.R., R.K. Kolka, and J.W. Stringer (2005). "Defining perennial, intermittent and ephemeral channel in Eastern Kentucky: Application to forestry best management practices". In: *Forest and Ecology Management* 214, pp. 170–182. DOI: 10.1016/j.foreco.2005.04.008.

Tarboton, D.G. (1996). "Fractal river networks, Hortons laws and Tokunga cyclicity". In: *Journal of Hydrology* 187, pp. 105–117. DOI: 10.1016/S0022-1694(96)03089-2.

Terui, A. et al. (2018). "Metapopulation stability in branching river networks". In: pp. 1–7. DOI: 10.1073/pnas.1800060115.

Todd, M. Jason et al. (2010). "Hydrological drivers of wetland vegetation community distribution within Everglades National Park , Florida". In: *Advances in Water Resources* 33.10, pp. 1279–1289. ISSN: 0309-1708. DOI: 10.1016/j.advwatres.2010.04.003. URL: http://dx.doi.org/10.1016/j.advwatres.2010.04.003.

Tonkin, J.D. et al. (2017). "The role of dispersal in river network metacommunities: Patterns, processes, and pathways". In: *Freshwater Biology*. DOI: 10.1111/fwb.13037.

Unmack, P.J. (2001). "Fish persistence and fluvial geomorphology in central Australia". In: *Journal of Arid Environments* 49.4, pp. 653–669. ISSN: 01401963. DOI: 10.1006/jare.2001.0813.

Uys, M.C. and J.H. O'Keeffe (1997). "Simple words and fuzzy zones: early directions for temporary river research in South Africa". In: *Environmental Management* 21.4, pp. 517–531.

Van Meerveld, H.J.I. et al. (2019). "Expansion and contraction of the flowing network changes hillslope flowpath lengths and the shape of the travel time distribution". In: *Hydrological and earth system sciences*. DOI: 10.5194/hess-2019-218.

Vander Vorste, R., R. Sarremejane, and T. Datry (2020a). *Intermittent rivers and ephemeral streams: a unique biome with important contributions to biodiversity and ecosystem services*. Vol. 4. Elsevier Inc., pp. 419–429. ISBN: 9780124095489. DOI: 10.1016/b978-0-12-409548-9.12054-8.

Vander Vorste, R., R. Sarremejane, and T. Datry (2020b). "Intermittent rivers and ephemeral streams: a unique biome with important contributions to biodiversity and ecosystem services". In: *Encyclopedia of the World's Biomes* 4, pp. 419–429. DOI: 10.1016/B978-0-12-409548-9.12054-8.

Vogel, R.M. and N.M. Fennessey (1994). "Flow-duration curves. I: New Interpreteation and confidence intervals". In: *Journal of Water Resources Planning and Management* 120.4, pp. 485–504. DOI: 10.1061/(ASCE)0733-9496(1994)120:4(485).

Von Schiller, D. et al. (2014). "Carbon dioxide emissions from dry watercourses". In: *Inland Waters* 4, pp. 377–382. DOI: 10.5268/IW-4.4.746.

Ward, A., N.M. Schmadel, and S.M. Wondzell (2018). "Simulation of dynamic expansion, contraction, and connectivity in a mountain stream network". In: *Advances in Water Resources* 114, pp. 64–82. DOI: 10.1016/j.advwatres.2018.01.018.

Whiting, J.A. and S.E. Godsey (2016). "Discontinuous headwater stream networks with stable flowheads, Salmon River basin, Idaho". In: *Hydrological Processes*. DOI: 10.1002/hyp.10790.

Wiginton, P.J., Moser T.J., and Linderman D.R. (2005). "Stream network expansion: a riparian water quality factor". In: *Hydrological Processes* 19(8), pp. 1715–1721. DOI: 10.1002/hyp.5866.

Williamson, T.N. et al. (2015). "Classification of ephemeral, intermittent, and perennial stream reaches using a topmodel-based approach". In: *Journal of the American Water Resources Association* 51. DOI: 10.1111/1752-1688.12352.

Wohl, E. (2017). "The significance of small streams". In: *Frontiers of Earth Sciences* 11, pp. 447–456. DOI: 10.1007/s11707-017-0647-y.

Woodget, A.S. et al. (2015). "Quantifying submerged fluvial topography using hyperspatial resolution UAS imagery and structure from motion photogrammetry". In: *Earth Surface Processes and Landforms* 40.1, pp. 47–64. ISSN: 10969837. DOI: 10.1002/esp.3613.

Woodget, A.S. et al. (2017). "Drones and digital photogrammetry: from classifications to continuums for monitoring river habitat and hydromorphology". In: *WIREs Water* 4.4, pp. 1–20. ISSN: 2049-1948. DOI: 10.1002/wat2.1222.

Yi, R.S. et al. (2018). "Shapes of river networks". In: *Proceedings of the Royal Society A* 474. DOI: 10.1098/rspa.2018.0081.

Zanetti, F. et al. (2021). "Analysing river network dynamics and active length - discharge relationship using water presence sensors". In: *Hydrology and Earth System Sciences Discussions* March, pp. 1–27. ISSN: 1812-2108. DOI: 10.5194/hess-2021-103.

Zeigler, S.L. and W.F. Fagan (2014). "Transient windows for connectivity in a changing world". In: *Movement Ecology* 2.1, pp. 1–10. ISSN: 20513933. DOI: 10.1186/2051-3933-2-1.

Zhou, Y. and W.F. Fagan (2017). "A discrete-time model for population persistence in habitats with time-varying sizes". In: *Journal of Mathematical Biology* 75.3, pp. 649–704. ISSN: 14321416. DOI: 10.1007/s00285-017-1095-8.

Zimmer, M.A. and B.L. McGlynn (2017). "Ephemeral and intermittent runoff generation processes in a low relief, highly weathered catchment". In: *Water Resources Research* 53, pp. 7055–7077. DOI: 10.1002/2016WR019742.

Zimmer, M.A. et al. (2020). "Zero or not? Causes and consequences of zero-flow stream gage readings". In: *WIREs Water* 7. DOI: 10.1002/wat2.1436.